

Computational methods in hydrogeophysics

by

Klara Steklova

B. Applied Ecology, Czech University of Life Science, Prague, 2006

M. Ecohydrology and Groundwater management, Wageningen University, 2009

A THESIS SUBMITTED IN PARTIAL FULFILLMENT
OF THE REQUIREMENTS FOR THE DEGREE OF

Doctor of Philosophy

in

THE FACULTY OF GRADUATE AND POSTDOCTORAL STUDIES
(Geophysics)

The University of British Columbia
(Vancouver)

March 2017

© Klara Steklova, 2017

Abstract

Parameter and state estimation for groundwater models within a coupled hydrogeophysical framework has become common in the last few years as it has been shown that such estimates are usually better than those from a single data inversion. Different approaches have been suggested in literature to combine the essentially two different modalities in order to obtain better estimates for groundwater models, and improve monitoring of processes such as solute transport. However, the coupled approaches usually come at a price of higher computational cost and difficulties in coupling the geophysical and groundwater inverse problems.

Unlike in other studies, we developed both the groundwater and geophysical models in the same computational environment in order to test different minimization strategies. When solving the coupled inverse problem, the objective function consists of data misfit and regularization terms as well as a coupling term that relates groundwater and geophysical states. We present a novel approach to solve the inverse problem using an Alternating Direction Method of Multipliers (ADMM) to minimize the coupled objective function. ADMM enables us to treat the groundwater and geophysical part separately and thus use existing software with minor changes.

However, ADMM as well as many other coupled approaches relies on implementing some petrophysical relationship to couple the groundwater and geophysical variable. Such relationships are usually uncertain and hard to parametrize for a large region and can potentially produce solute mass errors in the final model estimates. Therefore, in this thesis we examine coupled approaches that replace the fixed petrophysical relationship by a more loose structure similarity constraint. Besides, we propose efficient computational methods to minimize the objective function when there is no explicit petrophysical constraint.

All approaches were tested on 3D synthetic examples. In the solute tracer test we estimated hydraulic conductivity or solute distribution using a structure coupled inversion,

and were able to reduce the errors compared to a single data inversion alone. For a more complex example of seawater intrusion we implemented the ADMM method, and obtained better estimates for the solute distribution compared to just considering each data separately, or solving the problem with a simple coupled approach.

Preface

This dissertation is my original work made under supervision of Dr. Haber during the study program at the University of British Columbia.

The first three chapters review the current modeling practices and state of the art in hydrogeophysics. Chapter 4 presents new ideas for the joint inversion minimization and structure coupled inversion which came from conversations with Dr. Haber.

The code implementation and numerical experiments were carried out by myself with Dr. Haber's support and advice, and form the Chapter 5. The results in the first section of chapter 5 were published in [91], and the results in the second section are part of the manuscript, which is currently under review [90].

Table of Contents

| | |
|--|-------------|
| Abstract | ii |
| Preface | iv |
| Table of Contents | v |
| List of Tables | viii |
| List of Figures | x |
| Acknowledgements | xv |
| 1 Introduction | 1 |
| 1.1 Geophysical data in hydrology | 3 |
| 1.2 Hydrogeophysics: different approaches to couple the modalities | 5 |
| 1.3 Coupled hydrogeophysical inversion: The state of art | 7 |
| 1.3.1 Structure - coupled inversion | 9 |
| 1.4 Thesis objectives and research contributions | 11 |
| 2 Forward modeling | 14 |
| 2.1 Groundwater model | 14 |
| 2.1.1 Modeling of solute tracer movement | 15 |
| 2.1.2 Variable density flow (VDF) model | 21 |
| 2.1.3 Testing the GW models | 24 |
| 2.2 Geophysical modeling | 27 |
| 2.2.1 Direct current resistivity survey | 27 |
| 2.2.2 Time domain electromagnetic survey (TDEM) | 28 |

| | | |
|----------|--|-----------|
| 3 | Inverse problem for a single model | 32 |
| 3.1 | Ill-posedness and regularization | 32 |
| 3.2 | Gauss-Newton method | 34 |
| 3.3 | Sensitivities | 36 |
| 4 | Coupled inverse problem | 41 |
| 4.1 | Coupling the GW and geophysical variables | 42 |
| 4.1.1 | Petrophysical relationships | 42 |
| 4.1.2 | Structure-based coupling | 44 |
| 4.1.3 | Discretization of the coupling terms | 46 |
| 4.2 | Formulation of the coupled problem | 48 |
| 4.3 | Minimization with an explicit petrophysical constraint | 49 |
| 4.3.1 | ADMM | 50 |
| 4.4 | Minimization without an explicit petrophysical constraint | 53 |
| 4.4.1 | BCDM | 53 |
| 4.4.2 | Joint Gauss-Newton method (JGN) | 55 |
| 5 | Applications - synthetic examples | 57 |
| 5.1 | Seawater intrusion - state estimation with ADMM | 57 |
| 5.1.1 | Parametrization for the synthetic scenarios | 59 |
| 5.1.2 | Joint inversion with ADMM | 62 |
| 5.1.3 | Joint inversion by ADMM with inexact GW parameters | 66 |
| 5.1.4 | Summary | 71 |
| 5.2 | Solute tracer test - Parameter and state estimation without an explicit petrophysical relationship | 73 |
| 5.2.1 | Parametrization | 74 |
| 5.2.2 | Example 1 and 2: Estimation for initial state c_0 | 77 |
| 5.2.3 | Example 3: Estimation for hydraulic conductivity K | 80 |
| 5.2.4 | Summary | 88 |
| 5.3 | Joint inversion with electromagnetic loop survey | 90 |
| 5.3.1 | Joint inversion with ADMM | 91 |
| 5.3.2 | Summary | 93 |
| 6 | Conclusions | 95 |

Bibliography 99

List of Tables

| | | |
|-----------|---|----|
| Table 5.1 | Parametrization for the seawater intrusion Cases 1 and 2. | 60 |
| Table 5.2 | Errors, $\epsilon(\omega_k) = \ \omega_k - \omega_{true}\ $, for the solute content at time t_0 and t_1 for the two different cases. | 65 |
| Table 5.3 | Errors, $\epsilon(\omega_k) = \ \omega_k - \omega_{true}\ $, for the solute content at time t_0 and t_1 for Gauss-Newton method with the substitution of σ ; 1. The weights were fixed throughout the minimization based on the initial data misfits; 2. δ_f was adjusted as $\delta_f = \frac{\phi_{D,e}}{\phi_{D,f}}$ at each iteration; 3. δ_e was adjusted as $\delta_e = \frac{\phi_{D,f}}{\phi_{D,e}}$ at each iteration. GN inversion run up to 10 iterations. | 66 |
| Table 5.4 | Errors, $\epsilon(\omega_k) = \ \omega_k - \omega_{true}\ $, for the solute content at time t_0 and t_1 when different from true GW parameters are used in the ADMM inversion or coupled approach. Test 1 - change in permeability field. Test 2 - 70% reduction in permeability and dispersion values. | 70 |
| Table 5.5 | Computational cost overview for the forward model (f.m.) runs and actual run time of the inversion; all results displayed were executed on a desktop with Intel(R) Core(TM)i7-2860 QM processor and 16GB RAM. Parameters for line search procedure were the same for all methods, amount of iteration counts is displayed in the brackets next to each method. | 72 |
| Table 5.6 | Parametrization for the solute tracer Examples 1, 2 and 3. | 75 |
| Table 5.7 | Minimization parameters for the inverse problem | 76 |
| Table 5.8 | Example 1: Summary of the errors for the solute distribution and electrical conductivity estimates, the data misfits and the cross-gradient coupling terms (between the estimate and the true field) by either separate inversion or joint inversion with cross-gradient product. | 78 |

| | | |
|------------|--|----|
| Table 5.9 | Example 1 and 2: Summary of the relative errors (joint inversion vs GW (or DC) data only) for the solute distribution and electrical conductivity estimates based on the results from 10 different GW survey designs. | 78 |
| Table 5.10 | Example 2: Summary of the errors for the solute distribution and electrical conductivity estimates, the data misfits and the cross-gradient coupling terms (between the estimate and the true field) by either separate inversion or joint inversion with cross-gradient product. | 80 |
| Table 5.11 | Example 3: Estimation of hydraulic conductivity with KL expansion parametrization: Summary of the errors for the solute distribution, electrical conductivity and hydraulic conductivity estimates (and also the estimate for $\mu = \text{mean}(K)$, the true value was $mu = -1.8$) by either separate inversion or joint inversion with cross-gradient product. A final cross-gradient product between c^n and σ is displayed too. | 84 |
| Table 5.12 | Example 3: Summary of the relative errors (joint inversion vs GW data only) for the solute distribution at c_n , hydraulic head h and logarithm of errors for conductivity K based the results from 10 different GW survey designs. | 84 |
| Table 5.13 | Errors for the initial and final solute content at time t_0 and t_1 for the two different Cases 1 and 2. | 91 |

List of Figures

| | | |
|------------|--|----|
| Figure 1.1 | A simple dipole - dipole survey with one receiver pair and one source pair, from [73]. | 4 |
| Figure 1.2 | Coupled hydrogeophysical problem: each problem can be treated separately (blue and orange loop) or the petrophysical relationship can be added and both models updated in some coupled fashion (yellow loop). | 6 |
| Figure 2.1 | A single cell in the staggered grid of the discretized groundwater model, hydraulic head h and solute concentration c live in the cell centers, fluxes are computed at the cell faces. | 18 |
| Figure 2.2 | Visualization of the Semi-Lagrangian scheme in 2D: Interpolation of solute mass $\mathbf{x}_{t+\Delta t}$ which was advected from the cell center at \mathbf{x}_t to surrounding cells. We track the particles (cell centers) forward along the flowlines. | 19 |
| Figure 2.3 | Test against analytical solution for advective transport: Semi-Lagrangian method (left) vs Lax-Friedrich implicit scheme (right). Simulations were run for three different time steps, from top to bottom, $t = 15, 40$ and 80 days, corresponding to Courant number $0.33, 1$ and 1.33 . The solid line is the modeled break through curve and the dashed one is the analytic solution. | 25 |
| Figure 2.4 | The boundary conditions setup for a Henry's benchmark problem, seawater boundary is on right, freshwater inflow on the left. | 26 |
| Figure 2.5 | Contour plots for two cases of testing the Henry's benchmark problem representing the steady state solutions for solute mass fraction. Left: the dimensionless parameters $a = 0.33, b = 0.01$; right: $a = 0.33, b = 0.1$, which correspond to the solutions in [1] | 26 |
| Figure 2.6 | DC survey scheme for a single source and receiver. | 28 |

| | | |
|------------|---|----|
| Figure 2.7 | Staggered discretization for the TDEM model, properties such as permeability μ and electrical conductivity σ are at the cell centers, magnetic field b is computed at the cell face and electric field e on edges. | 30 |
| Figure 3.1 | The reference model for SWI inverse problem. The resulting conductivity σ_{ref} has high solute mass fraction along the seaward boundary on the left, as expected in real conditions. | 35 |
| Figure 4.1 | Comparison of the JGN and BCDM scheme. Left: The scheme for a single iteration of the Joint Gauss - Newton minimization, the two data misfit terms Φ_D , regularization terms Φ_R and a similarity term Φ_S are computed for the initial estimates of m and σ , both models are then updated via a Gauss-Newton iteration (Eq.(4.34)). Right: BCDM minimization starts with the Gauss-Newton descent for the groundwater model m only (Eq.(4.32)) involving also the similarity term, the new GW model m_{k+1} serves as an input for the geophysical Gauss-Newton descent (Eq.(4.31)), leading to an update for the geophysical model, σ_{k+1} , the next BCDM iteration starts with m_{k+1} and σ_{k+1} | 56 |
| Figure 5.1 | Effect of increased pumping on the propagation of the SWI front. Source: A.D. Wenner, P.E. Jacobsen, L.K. Morgan - Understanding seawater intrusions [poster]. 2013 | 58 |
| Figure 5.2 | The geological layers for the heterogeneous case based on Kidd2 site in Fraser River delta [71], schema for k_z field. | 60 |
| Figure 5.3 | Seawater intrusion scenario: Upper left and right: True models for initial and final solute distribution for Case 1; Bottom left and right: True models for initial and final solute distribution for Case 2. Isosurfaces at $\omega = 0.25, 0.5$ and 0.75 are displayed. | 61 |
| Figure 5.4 | Data collection. Left: Experimental design for the DC survey: Dark blue points represent the electrodes on the surface placed on a regular grid, saltwater is coming in from the west boundary. Right: GW wells locations, 8 wells in total are placed along two transects at $x = 16 m$ and $x = 24 m$ distance, later labeled as b and c , other experimental designs for GW data are plotted in Figure 5.10. | 62 |

| | | |
|-------------|---|----|
| Figure 5.5 | The error and residual decrease during the ADMM descents: Green triangles represent the scaled error for the final solute fraction ω_f , orange stars correspond to updated r_k values, where $r_k = \sigma_f(k) - p(\omega_f(k))$. The GW wells in this case were placed along $x = 16\text{ m}$ and $x = 24\text{ m}$ | 63 |
| Figure 5.6 | ADMM estimates for Case 1: Contour profiles at $x = 10$ and $x = 20$. The dashed lines are estimates from the joint inversion (ADMM), and the full contour lines are the actual locations corresponding to $\omega = 0.25$ (blue), $\omega = 0.5$ (green) and $\omega = 0.75$ (red). | 64 |
| Figure 5.7 | ADMM estimates for Case 2: Contour profiles at $x = 10$ and $x = 20$. The dashed lines are the estimates from the joint inversion (ADMM), and the full contour lines are for true locations corresponding to $\omega = 0.25$ (blue), $\omega = 0.5$ (green) and $\omega = 0.75$ (red). | 64 |
| Figure 5.8 | ADMM estimates. Upper left and right: Estimates for initial and final solute distribution for Case 1. Bottom left and right: Estimates for initial and final solute distribution for Case 2. Isosurfaces at $\omega = 0.25, 0.5$ and 0.75 are displayed. The true models are plotted in Figure 5.3 | 65 |
| Figure 5.9 | The relative error decrease for five different GW sampling designs; the dotted line is for the ω_0 relative error, the full line for the ω_f relative error decrease. In all cases the error decrease slows down with further iterations. The plotted results are based on different transects of wells plotted in Figure 5.10. | 67 |
| Figure 5.10 | The transects along x and y axis in plan view. For the homogeneous Case1 the sampling depths were $z = [3, 7, 11]$, and for the heterogeneous Case 2 $z = [5, 9]$. each design had two vertical or horizontal transects. | 67 |
| Figure 5.11 | Altering the GW parameters: Errors decrease for ω_f estimate and residual r_k when correct and altered GW parameters (D, k) are used in ADMM. The errors for ω_f for the coupled approach are plotted as well with a dashed line, it is just a single value. | 68 |
| Figure 5.12 | Altering the GW parameters: The true permeability field in x direction k_x in the second test. For solving the inverse problem a fixed value $k_x = 4.4^{-11}$ was used instead, while the true field is shown in this figure. The true k_y and k_z were altered similarly when simulating GW data. | 69 |
| Figure 5.13 | Altering the GW parameters: Errors decrease for ω_f estimate and residual r_k when correct and altered GW permeability is used in ADMM. The errors for ω_f for the coupled approach are plotted with a dashed line. | 69 |

| | | |
|-------------|--|----|
| Figure 5.14 | Solute tracer test. Left: A scheme for the GW survey design with two transect of wells, applied in Example 1 and 2. Right: A scheme for DC survey with receivers on surface only, in the background is the electrical conductivity model applied in Example 2 which spatially correlated more conductive field than background. | 75 |
| Figure 5.15 | Different GW surveys for solute tracer test. Ex 1,2 - des1: Two transects of wells at $x = 14$ and 18 m applied in Example 1 and 2. Ex 1,2 - grid: 4×5 grid of wells from which 8 locations was chosen randomly for each run. Ex3-des1: 3×3 grid of wells locations for results presented in Table 5.11. Ex3-grid: Regular grid of well from which 10 wells were randomly chosen, corresponding results summarized in Table 5.12 | 76 |
| Figure 5.16 | Solute tracer test. The true models for the initial solute concentration in Example 1 (left) and Example 2 (right), isosurfaces displayed at $c_0 = 0.2, 0.4, 0.6$ and 0.8 | 77 |
| Figure 5.17 | Example 1 and Example 2: Bar plots for the error estimates by different methods, the actual values are in Table 5.8, Table 5.10 respectively. | 78 |
| Figure 5.18 | Example 1: The true models vs the estimates by GW data inversion and structure-coupled inversion, contours at $z = 8$ and $y = 18$ for final and initial solute c^n, c^0 are plotted. | 79 |
| Figure 5.19 | Example 2: The true models vs the estimates by GW data inversion and structure-coupled inversion, contours at $z = 8$ and $y = 18$ for final and initial solute c^n, c^0 are plotted. | 81 |
| Figure 5.20 | Example 2: The estimates for 10 different experimental designs, altering location of 8 wells from Ex 1,2 - grid design. | 82 |
| Figure 5.21 | Example 3 : Bar plot for the errors by different methods, the actual values are in Table 5.11 | 84 |
| Figure 5.22 | Example 3: The true models vs GW data and structure-coupled inversion estimates for the final solute concentration, contours at $z = 8$ and $y = 16$ are plotted and hydraulic head at $y = 24$ | 85 |
| Figure 5.23 | Example 3: The estimates for 10 experimental designs by different methods, altering the location of 10 wells in Ex3-grid design. | 86 |
| Figure 5.24 | Example 3: The true field and estimates of hydraulic conductivity K by GW data only and JGN and BCDM. | 87 |

| | | |
|-------------|---|----|
| Figure 5.25 | The experimental design for EM survey: Loop (transmitter) is placed in the center on surface, the receiver coils are placed on surface in an uniform grid. | 90 |
| Figure 5.26 | The error and residual decrease during the ADMM descents: Green triangles represent the scaled error for the final solute fraction ω_f , orange stars correspond to updated r_k values, where $r_k = \sigma_f(k) - p(\omega_f(k))$. The GW wells in this case were placed along $x = 16\text{ m}$ and $x = 24\text{ m}$ | 91 |
| Figure 5.27 | ADMM estimates for Case 1: Contour profiles at $x = 10$ and $x = 20$. The dashed lines are estimates from the joint inversion (ADMM), and the full contour lines are the actual locations corresponding to $\omega = 0.25$ (blue), $\omega = 0.5$ (green) and $\omega = 0.75$ (red). | 92 |
| Figure 5.28 | ADMM estimates for Case 2: Contour profiles at $x = 10$ and $x = 20$. The dashed lines are estimates from the joint inversion (ADMM), and the full contour lines are the actual locations corresponding to $\omega = 0.25$ (blue), $\omega = 0.5$ (green) and $\omega = 0.75$ (red). | 92 |
| Figure 5.29 | ADMM estimates. Upper left and right: Estimates for initial and final solute distribution for Case 1. Bottom left and right: Estimates for initial and final solute distribution for Case 2. Isosurfaces at $\omega = 0.25, 0.5$ and 0.75 are displayed. The true models are plotted in Figure 5.3 | 93 |
| Figure 5.30 | The relative error decrease for different GW sampling designs; the dotted line is for the ω_0 relative error, the full line for the ω_f relative error decrease. The plotted results are based on different transects of wells plotted in Figure 5.10. | 94 |

Acknowledgements

I would like to start off by thanking my advisor, Eldad Haber, for giving me the opportunity to join the PhD program at UBC, helping me with funding, allowing me to research the topics I enjoyed most, and guiding me in a research field which was new to both of us. The fact that I could pursue my PhD studies in Vancouver had a huge impact not only on my professional, but also, personal development.

I also want to acknowledge Roger Beckie who always found time for me and gave me advice when I asked. I enjoyed being a teaching assistant in his Groundwater hydrology and Contaminant transport classes because it gave me an opportunity to explore a role in the academic world other than research.

I want to thank all GIF members for all our valuable discussions and, just as importantly, for creating a pleasant environment to work in. And a special thanks to Mike Mitchell for reviewing this thesis.

Last but not the least, I would like to thank to my family for their encouragement during this long term commitment, but also to all of my “Vancouver families” in capoeira, dance and sailing for the great times outside of work.

Special thanks to my mum for her limitless psychical support, to Matei for encouraging me to apply to UBC and always having a good advice when I was frustrated, and to my friends - Sonja, Romain, Sarka, Daja, Radka, Olda, Ludek, Jonas, Gata, Luz, Dean, Nick and many others for their cheering and support.

Chapter 1

Introduction

Many different processes in groundwater hydrology can be labeled as solute transport, comprising different scales and both natural and human affected processes. At a small scale we can think of fertilizers moving through the root zone, a contaminant plume observed in a few wells can already affect an area of watershed size, or seawater intrusions that can affect large regions along the coastal zones. While all these examples evolve from different applications, they have a few important commonalities. In all these cases we need a groundwater flow model to determine the flow field in the subsurface and a solute transport model, to describe, and ideally also to predict the fate of the solute.

Theoretically, we do have a groundwater flow and solute transport model specifically tailored for each different process; however, conceptualizing from the real environment to a mathematical model brings a lots of uncertainty. The soil and porous media are rarely homogeneous, and processes such as dispersion and diffusion are hard to upscale from the real scale heterogeneity to the actual model resolution. Furthermore, we need to make decisions regarding the boundary and initial conditions, which are sometimes fairly straightforward, but in more complex situations the particular choice can substantially impact the model outcomes.

From the numerical point of view, the modeling challenges arise in solving the governing equations, which are a system of two partial differential equations for flow and solute mass

balance:

$$\frac{\partial(\phi\rho)}{\partial t} + \nabla \cdot (\rho q) = \rho Q_{gw} \quad (1.1)$$

$$\frac{\partial(\phi\rho\omega)}{\partial t} + \nabla \cdot (\phi\rho D\nabla\omega) - \nabla \cdot (\rho\omega q) = Q_{s\omega}, \quad (1.2)$$

where ρ is the fluid density, ω is the solute mass fraction, ϕ porosity, D represents the hydrodynamic dispersion, t time and $Q_{s\omega}$ and Q_{gw} the external fluxes of solute and groundwater. These two equations are coupled via groundwater flux q ;

$$q = -\frac{k}{\mu}(\nabla p + \rho g \nabla z), \quad (1.3)$$

where k is permeability of the porous media, p fluid pressure, μ fluid viscosity, z is downward depth coordinate and g gravity acceleration. Hence, if the fluid density does not change, we can basically decouple the system and the groundwater flow is essentially governed by the pressure gradient, ∇p , only. For flow of variable density though, the governing equations are strongly coupled and weakly nonlinear. Any 3D simulation is therefore computationally costly especially when considering the inverse problem.

To overcome the challenge of conceptualization, i.e. simplifying the real world into a representative physical model, we need to have enough data to properly calibrate the groundwater model, and hence reduce the uncertainty regarding parameters and initial or boundary conditions. However, data availability is usually somewhat limited for a few reasons.

Obtaining measurements via groundwater sampling can be costly and difficult. Direct groundwater data are usually obtained from boreholes or wells, which even with multiple screening intervals provide only a few data points information for groundwater states, such as solute concentration or hydraulic head. Moreover, for variable density flow models additional density data has to be obtained next to standard head measurements. The density information can come from concentration data (respectively electrical conductivity of water samples), but this is prone to error due to the difference between resident and flow concentration (i.e. the collected samples might not represent well the surrounding environment [15]). Besides, parameters like dispersivities or permeability can not be measured directly at the field scale and we thus have to rely on indirect data and laboratory samples.

In many cases, where the complexity of the solute transport process is high, the avail-

able groundwater data is too scarce for a successful calibration and good predictability of the underlying models. In these cases, some of the properties such as fluid conductivity, saturation or porosity, can be well captured by geophysical methods sensitive to these properties. Indeed, as we show in this work, geophysical methods provide an attractive option to add more information for groundwater model calibration, and improve the solute transport monitoring and predictions.

1.1 Geophysical data in hydrology

Recent advances in geophysical instrumentation as well as computational software have made many geophysical techniques more accessible for environmentally oriented surveys [53]. In groundwater hydrology geophysical methods have already become standard techniques to map the bedrock topography, the geology, estimate hydraulic conductivities by salt tracer tests, and for monitoring seawater intrusions. A new discipline, hydrogeophysics, developed focusing on the use of geophysical measurements for mapping subsurface features, estimating properties and monitoring processes that are important to hydrological studies [84].

For example, Direct Current (DC) resistivity methods found a broad application across different areas of hydrology. In DC experiments a current is injected into the ground creating an electrical potential, which is then measured using pairs of electrodes - receivers placed on the surface or in boreholes (Figure 1.1). The DC method was successfully applied in many hydrogeophysical studies for solute transport, such as tracer tests and seawater intrusions ([47], [32],[45],[44],[20],[51] or [49]) but also to investigate unsaturated zone transport, such as soil salinization [52], or hyporheic flow transport [98]. The conductivity of saltwater is a few orders higher than that of freshwater in the pore spaces. Hence, saltwater intrusion increases the soil bulk electrical conductivity, which makes it an excellent target for electromagnetic and electrical resistivity methods. DC surveys were also successfully used to identify clay lenses, which have higher conductivity compared to other geological materials, and to determine variable moisture content [12, 73].

Electromagnetic methods (EM) are based on the electromagnetic induction effect, and are also sensitive to changes in subsurface conductivity; however, the different physical process of charging conductive bodies in the subsurface can make these methods better for recovering the soil bulk conductivity. Depending on the type of survey one can collect 1D data, so called EM soundings, with possible large depth investigation or target shallow

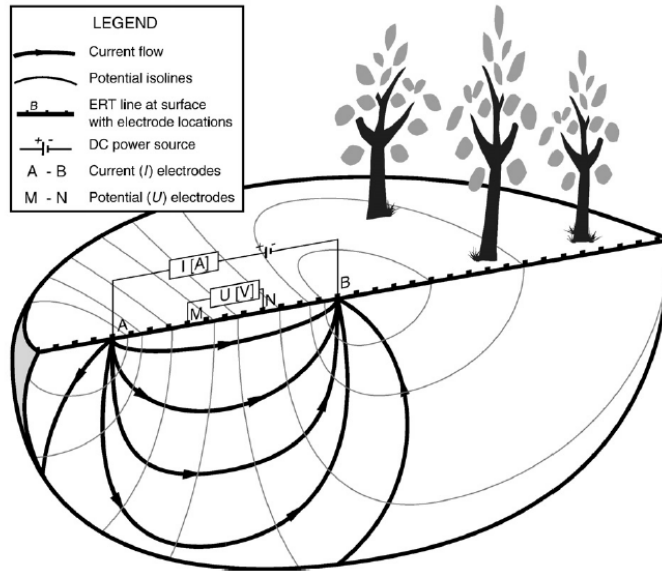


Figure 1.1: A simple dipole - dipole survey with one receiver pair and one source pair, from [73].

depths with shorter offsets and obtain two and 3D data. In airborne surveys, a helicopter carrying transmitter and receiver coils can easily map large areas. EM applications in groundwater hydrology are similar to those of DC methods, but for large scale studies EM surveys are usually preferred due to easier, though more expensive, data acquisition. For example in [77] they collected airborne electromagnetic data in the Red River basin of Texas to estimate the volume of water intruded by saline water, capturing an area of 34 km². Other examples of seawater intrusion monitoring via EM methods can be found in [72],[93] or [14].

Ground penetrating radar is another non-invasive geophysical technique used by hydrologists, which is sensitive to changes in dielectric permittivity. The reflection depth can give information about location of lower density plumes [22] or geological structures such as fluvial deposits [24], which can then help in estimating the hydraulic conductivity of the aquifer. Seismic or nuclear magnetic resonance methods have also been used to study hydrological problems [21, 40, 96].

The main advantage of geophysical methods lies in their non-invasive character and ability to map a large subsurface area. As opposed to groundwater sampling methods that give only point wise observations, geophysical methods can provide extensive 3D data sets

in a relatively short time for a large and heterogeneous area. Many geophysical methods are available, which together with different experimental designs offer large to small scale investigation of the subsurface. However, the main caveat of geophysical methods is that the collected data, regardless the chosen method, are indirect. Therefore, an inverse problem has to be solved to recover the subsurface geophysical property field. This inverse problem is usually ill-posed leading to non-unique solutions dependent on some “a priori” information. Furthermore, the groundwater property of interest is linked to the geophysical property via some petrophysical relationship, which is based on empirical laws and has to be calibrated for specific field conditions. The parametrization for this relationship then brings another source of uncertainty when “incorporating” the geophysical information into groundwater estimates. Geophysical data thus come with a price of solving an inverse problem and determining the link between the geophysical and groundwater variables.

1.2 Hydrogeophysics: different approaches to couple the modalities

Combining the geophysical and hydrological data increases the amount of data about the flow in subsurface and hopefully can help to overcome some of the caveats of each specific, individual type of data. Ideally, we want to keep the advantages of both types of data and improve the estimates of groundwater states and parameters. We should keep in mind though that both the geophysical and groundwater inverse problems are ill-posed; with limited data we want to recover the 3D subsurface properties. Hence, both inverse problems need some form of regularization (a-priori information), that would steer the estimates towards physically realistic ones.

As Figure 1.2 shows, each inverse problem can be treated separately, we can add some regularization and solve it for one type of data only. The geophysical estimate can then be converted to a groundwater variable via some petrophysical relationship allowing geophysical and hydrogeological computations to stay independent. The advantage of such an uncoupled framework is that the hydrogeological and geophysical models run independently. However, this also means that the a-priori information from hydrology is not integrated into the geophysical inversion. Since geophysical inverse problems are ill-posed and require a regularization term, or a prior (if Bayesian methods are used), ignoring hydrogeology data can severely deteriorate the quality of the geophysical inversion estimates.

Another option is to include the coupling term which represents the link between the

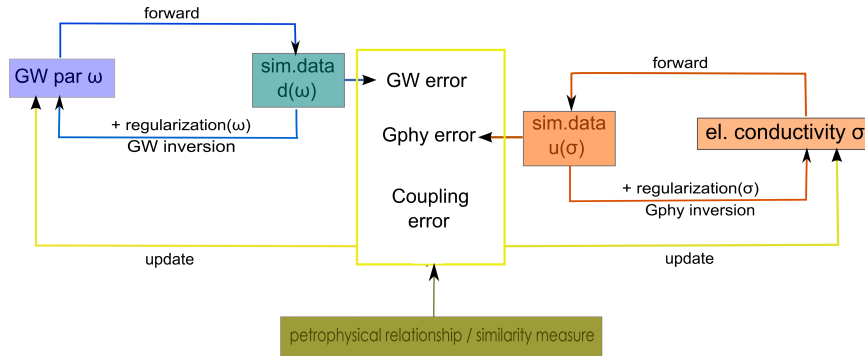


Figure 1.2: Coupled hydrogeophysical problem: each problem can be treated separately (blue and orange loop) or the petrophysical relationship can be added and both models updated in some coupled fashion (yellow loop).

groundwater and geophysical variables in the inversion. This is usually referred to as a coupled approach. The coupling term can be the previously mentioned petrophysical relationship, which is usually empirical (e.g. Archie’s law which relates soil bulk conductivity and fluid conductivity) or it can be set more loosely by only imposing a structure similarity, between the groundwater and geophysical models.

For the actual coupling, if we have an explicit relationship, the geophysical variable (estimate) can be transformed into a groundwater variable or the other way around. Thus, beside evaluating the similarity between the two models, one can also use one of the estimates as a reference model, and possibly also as an initial guess for solving the other inverse problem. Another option is “data extraction” [8], where we use the petrophysical relationship to convert the geophysical estimates into groundwater states and create some additional data for groundwater model inversion. For the actual inversion, some approaches invert only one type of data, however, both data misfits are evaluated with respect to the updated estimate ([45],[5]).

The different ways that the two types of data are combined and solved leads to various approaches in hydrogeophysical studies and therefore terminology vary among authors. However, in all coupled approaches, the geophysical and groundwater models are linked together during the inversion. The hydrological state estimates are then guaranteed to be physically realistic and fewer a-priori assumptions need to be entered into the geophysical inversion implicitly. Due to this fact, coupled approaches were repeatedly found to give better results ([44], [49] or [47]). However, coupled approaches are computationally

more intensive and possible errors introduced by the coupling term, may map from the groundwater to geophysical estimate and vice versa and need to be considered.

The joint approach can be considered as a specific type of a coupled approach, where both data misfits are minimized together. Since both models behave differently in terms of convergence, weighting the two different data misfits next to regularization and coupling term in one objective function can be a challenging task. Each of the problems can be difficult to solve by itself due to governing equations, which are partial differential equations, and solving them in a coupled manner can create even more computational complexity. Moreover, the forward and inverse simulations for the geophysical and groundwater models are commonly solved by separate codes, possibly “black-box”, which further complicates the joint inversion. Therefore, in most literature we find applications of coupled approaches rather than an actual joint minimization.

1.3 Coupled hydrogeophysical inversion: The state of art

Before reviewing some of the work on coupled hydrogeophysical inversions, we should recall that the groundwater (GW) forward problem alone may require solving a system of two strongly coupled and nonlinear partial differential equations, and thus any 3D simulation is costly when solving the inverse problem, where multiple forward simulations are necessary. To decrease the amount of estimated parameters and make the inverse problem solvable, usually some a-priori information based on geology is considered to reduce the size of the problem. One option is to apply some geostatistical constraints when estimating the GW parameters [46, 51, 80]. The actual minimization is then often directed by some general inverse software such as PEST [25] or UCODE [78] where the sensitivities are derived by a perturbation approach.

In the last decade, numerous studies have investigated the potential of coupled inversion and the resulting improvement in parameter estimation when compared to the inversion of a single data type. For example in [47] the authors tested the coupled versus uncoupled approaches for an infiltration event on synthetic data by joining HYDRUS1D model and ERT data simulations to estimate the soil properties. The authors confirmed the benefits of the coupled approach, although the results show that model estimates are highly dependent on how well the hydrologic model represents the real system.

The study of [44] also examined different approaches for coupling groundwater and geophysical data. In their synthetic study a simple cross-sectional groundwater model was

coupled with TDEM (1D soundings) and a real field dataset coupled a Modflow groundwater model with 1D ERT data. Both sequential and joint approaches were tested. In the sequential approach the geophysical inversion was independent, but the subsequent groundwater model inversion used the geophysical estimates, while in the joint approach the geophysical and groundwater models were updated simultaneously. Geometric and petrophysical constraints were used in this study to couple the GW model and geophysical data by relating a particular layer resistivity to its hydraulic conductivity. For the joint approach, the authors employed a petrophysical constraint as an additional regularization term. They observed that the joint approach increases the computational time compared to the sequential approach, with no significant improvement of the groundwater parameter estimates in the case of a real dataset.

The first joint hydrogeophysical inversion to estimate the hydraulic conductivity appears in [79] for a synthetic 2D experiment; the authors combined the temporal moments of electric potential perturbations with hydraulic head data. Later, the same approach was tested using a real data set from a sandbox laboratory experiment [80]. The fully coupled approach managed to successfully recover the solute transport and preferential pathways, the hydraulic conductivity fields were smoothed out but contained the main heterogeneous features.

In the study of Irving and Singha [49] the authors also jointly inverted geophysical ERT and groundwater concentration data for a saline tracer test; however they introduced a stochastic approach for this type of application. The pilot points technique was used to generate possible hydraulic conductivity fields in 2D and a Markov chain Monte Carlo sampling algorithm was implemented within the joint inversion. In [51] they expanded on this work by adding self potential data. The synthetic case results for their 2D profile showed improved estimates when combined data were used compared to an inversion of each type of data independently. The authors noted the necessity to parallelize the code to reduce computation time, if applied to 3D problems.

For seawater intrusions (SWI), with variable density flow modeling, the situation is usually more complex in terms of time scale and heterogeneity compared to solute tracer experiments. However, similar ideas were implemented in the calibration of underlying solute transport models, leading to a high diversity of approaches when solving the hydrogeophysical inverse problem. In most cases groundwater and geophysical data are inverted separately and the coupling happens via a petrophysical relationship.

In the study by [8] the authors investigated a sequential approach to estimate hydraulic

conductivity and dispersivity parameters, which they tested on two synthetic benchmark problems representing pumping experiments in a coastal aquifer in 2D. The ERT derived conductivities were transformed via Archie’s law to salt mass fraction. These estimates were then filtered using a cumulative sensitivity based on the squared Jacobian and served as data in the hydrogeological parameter estimation next to the “collected” salt mass fraction data. The inversion was performed with PEST using a gradient based method. The geophysical ERT data did improve the SWI model calibration.

The calibration of a seawater intrusion model using geophysical data can be also found in [45]. In this work the GW model is used to interpret the data and guide the geophysical inversion. Saltwater concentrations based on the 2D SEAWAT model were converted with Archie’s law to electrical resistivity and the forward modeled response of a TDEM sounding were calculated and compared with observed data. The TDEM data sets (1D soundings) were collected in Santa Cruz County, California. In total, six parameters were estimated for both the groundwater and TDEM model using the PEST optimization system. The authors concluded that the coupled approach provided a significant improvement in spatial resolution which would be hard to obtain with standard geophysical inversions.

Large scale hydrogeophysical problems are the focus of the recent work by [18]. The authors improved the inversion framework of iTOUGH2 to enable parallel computing and merge it with a parallel geophysical simulator for electromagnetic data, creating a general framework they can apply to a wide range of processes in multiphase flow and solute transport. The sensitivities with respect to parameters were evaluated by a perturbation approach, and the high computational burden of this approach was balanced by the fact that the perturbed model simulations could be run independently.

Compared to other synthetic studies and applications, we set up both models in the same computational environment in order to test different minimization schemes using a joint approach, which is one of the goals of this thesis. For the joint approach we propose a couple of methods that can split the minimization into two subproblems and thus ease the computational burden of the coupled problem.

1.3.1 Structure - coupled inversion

Most of coupled inversions and even inversion of geophysical data alone, involve some kind of petrophysical relationships that relate the two different physical properties. The petrophysical relationship represents an explicit way to impose a similar structure on two different

models. In environments with well mapped geology and well calibrated parameters it is feasible to generate a petrophysical map that links groundwater and geophysical parameters or states, yet such information is generally not available. Some authors question the validity of the petrophysical relationships (i.e. knowledge of the porosity distribution). In some cases researchers are able to calibrate it in the field, but often this petrophysical relation is accepted just by applying some fixed empirical parameters for either synthetic or field datasets. If incorrectly assigned this direct link may cause significant errors in the solute content estimates or enforce the coincidence of the two models, when there is none. This naturally leads to the idea of replacing the fixed petrophysical relationship by a more loose structural constraint.

In the structure-coupled inversion the two or more different models are not linked by an explicit petrophysical relationship but instead, some similarity is assumed, such that the two different models exhibit changes in the same regions. This similarity is imposed by a structural constraint in the minimization procedure leading to model estimates of different properties that share the same “structure”.

The idea of a structure-coupled inversion to image the subsurface using geophysical methods has been studied over two decades [34, 39, 64]. Typically, indirect data are collected by multiple methods, but due to the different physical phenomena of each method, the model estimates often vary [35]. Moreover, each set of data might have a very different resolution and be contaminated by different measurement errors. Still, inverting these datasets in some coupled fashion is desired if all data are related to the same geological feature. Examples of structure-coupled inversions with geophysical data can be found in [34, 48, 63, 69]. Joint total variation is particularly popular method for this type of joint geophysical inversion.

Similarly, when coupling the hydrological and geophysical inversions, different approaches exist that alleviate the need of the fixed petrophysical relationship. For example in the work of [13] the authors assumed that the parameter of interest was mainly affected by geological facies and used a level set method to minimize the coupled objective function. The same method could be expanded for joint inversion with groundwater and geophysical data using the same level set parametrization (geological facies distribution). In [54], the authors replaced the petrophysical relationship by an assumption of a strong correlation between the fluid and soil bulk electrical conductivity. In particular, for their synthetic study with a solute tracer test, they used ERT time lapse data together with groundwater head and fluid conductivity data to determine hydraulic conductivity.

To our knowledge, the first work applying a structural constraint in hydrogeophysical inverse problem is the study of Lochbuhler et al.[65]. The authors combine ground-penetrating radar data with hydraulic tomography or tracer mean arrival times to estimate hydraulic conductivity. As a structural constraint they applied a cross-gradient field product. In this thesis we further expand on the ideas of [65], but implement a full 3D inversion and jointly invert geophysical and hydrological data that are not directly dependent on the property of interest.

1.4 Thesis objectives and research contributions

The motivation for this thesis was to improve estimates for modeling of solute transport processes by combining hydrogeological and geophysical data. This objective was conquered in few different steps, which can be summarized as follows:

- **Developing the groundwater and geophysical models in conjunction with analytically derived data sensitivities**

Joint approaches were reported to improve the groundwater estimates. However, the forward and inverse simulations for the geophysical and groundwater models are commonly solved separately to take advantage of each inversion code and forward model. In the joint approach both data misfits are minimized together, which of course brings computational complexity by implementing the coupled framework, solving a larger problem and weighting the two different data misfits next to regularization and coupling term in the objective function.

In order to overcome some of these issues, we developed both models in the same computational environment, so that we can test different minimization schemes for a joint inversion of hydrological and geophysical data. The common framework also simplifies the coupling implementation between the physically different models. We derived the sensitivities of data with respect to parameters or states analytically, using a closed form formula. Unlike the perturbation approach, the analytical derivation of sensitivities significantly reduces the computation burden, and thus enables us to solve problems in 3D. We tested both models against benchmark problems or by tests using artificial sources.

- **Propose computationally efficient inversion scheme**

For the sake of simplicity and testing the approaches themselves, the hydrogeophysical inversions are often either of a small size or applying 2D data only. However, in

the field we can rather expect large domain and dataset, especially in case of geophysical data. In this thesis we therefore proposed a computationally efficient scheme, which can handle large datasets (e.g. discretization with more than 200 cells in each direction)

Specifically, we introduced a version of the alternating direction method of multipliers (ADMM), which allows us to efficiently split the objective function of the coupled inverse problem. ADMM was introduced in early 70's and has recently gained popularity for many inverse problems. It is a natural choice for multiphysics problems [11], due to its strong convergence properties [36]. ADMM is suitable for cases where the constraint (here the petrophysical relationship) can be considered as exact, in practice having low uncertainties usually suffices. A successful hydrological application can be found in Wohlberg et al. [99], where ADMM was applied to solve the inverse problem to estimate the piece-wise smooth hydraulic conductivity fields. Many more applications can be found in machine learning or statistical modeling.

In addition to ADMM we also examined other minimization techniques such as the Block Coordinate descent method (BCDM), which also splits the minimization onto two subproblems and a standard Gauss-Newton method, that updates both models at each iteration. Both Block coordinate descent and ADMM have a major advantage over the Gauss-Newton method. First, by splitting up the objective function into geophysical and groundwater part, we do not need to weight two different data misfits with respect to regularization and coupling term at each iteration. There are almost no criteria for setting two parameters during the iterative minimization process when each data misfit has a different speed of convergence. Second, the multiplication of Jacobians and data misfit can have a very different computational cost for each model and hence make each iteration very unbalanced and difficult to parallelize.

The ADMM method was tested on a seawater intrusion scenario, we jointly inverted the solute mass fraction data together with either DC resistivity or TDEM data to estimate the groundwater states.

- **Structure-coupled inversion**

Another limitation of the joint hydrogeophysical inversion is the knowledge of the petrophysical relationship. Despite its abundant use, this empirical relationship is hard to properly parametrize in field conditions and adds uncertainty to the coupled

inversion estimates. In this thesis we further explored the potential of joint hydrogeophysical inversion when the parameters for petrophysical relationships are unknown and implemented structural constraints such as the cross-gradient field product and joint total variation instead, so that the hydrological and geophysical data can be still inverted in a joint approach.

The coupling via structural constraints usually evaluates the gradient fields of each property rather than the actual values and thus encourage the two models to change in the same location. Therefore, it is a good alternative to a petrophysical link, as it does not enforce an exact linear mapping between soil bulk conductivity and solute content when there is none.

We tested the structure coupled inversion on a synthetic test of solute tracer to estimate the initial conditions for solute content and hydraulic conductivity field. Groundwater solute concentration and hydraulic head data were jointly inverted with DC resistivity data.

In the following chapter we elaborate on both groundwater and geophysical models used in this work, their governing equations, our chosen discretization and our approach for the solution of the forward problem. In chapter 3 we show a general scheme for the minimization of a single type of data, which has crucial importance when building up more advanced joint inversion schemes. The actual coupled inversion is detailed in chapter 4, where we also expand on coupling options such as petrophysical relationships and structure similarity constraints, and introduce the ADMM method together with other methods for joint inversion. Applications of all proposed methods are documented in chapter 5; section 5.1 is devoted to the seawater intrusion scenario (results of this experiment were published in [91]) and section 5.2 shows a structure-coupled inversion for a solute tracer test (the manuscript is under review). In the last chapter we summarize our findings.

Chapter 2

Forward modeling

In this chapter we present the models that we developed to test different minimization schemes in the hydrogeophysical inversion. For solute transport we have two models that can simulate solute tracer tests and seawater intrusions scenarios. Both of them are based on solute and fluid mass balance equations. For the geophysical modeling, direct current resistivity and time domain electromagnetic data were simulated. For each model we discuss the governing equations, applied assumptions, discretization and solution of the equations and present the results of some model verification tests.

2.1 Groundwater model

Models of solute transport can range from simplistic to fairly complex representations of the real world. The choice often depends on the application, required accuracy and available data for model parametrization. In solute tracer tests or plume monitoring, the time scale is often short, and density variation effects do not need to be considered. However, in applications such as seawater intrusions a full variable density flow model is desirable to improve the accuracy of forecasts.

In our study, we developed two groundwater models, both consist of the fluid and solute mass balance equation, where each one is represented by a partial differential equation in

time and space:

$$\frac{\partial(\phi\rho)}{\partial t} + \nabla \cdot (\rho q) = \rho Q_{gw} \quad (2.1)$$

$$\frac{\partial(\phi\rho\omega)}{\partial t} + \nabla \cdot (\rho\omega q) - \nabla \cdot (\phi\rho D\nabla\omega) = Q_{s\omega} \quad (2.2)$$

The system above is a pressure - solute mass fraction formulation [57], where ρ is the fluid density, ω is the solute mass fraction, ϕ is porosity, D represents the hydrodynamic dispersion, t is time and $Q_{s\omega}$ and Q_{gw} are the external fluxes of solute and groundwater respectively. The two governing equations are coupled via groundwater flux q (sometimes referred to as specific discharge), which, taking the general formulation for Darcy's law [7], can be written as

$$q = -\frac{k}{\mu}(\nabla p + \rho g \nabla z), \quad (2.3)$$

where p is the hydraulic pressure, k is the permeability of the porous media, μ is the fluid viscosity, g is the gravitational acceleration and z is an upward coordinate direction.

Depending on the problem we want to model, we need to add further assumptions or simplify the system above. If the fluid density changes across the model domain due to the solute content dynamic, the system becomes nonlinear and one needs to complete it with state equations which define the dependence of density ρ and other porous media parameters on the solute mass fraction. However, if the solute dynamic does not effect the density we can simplify the system by taking the density ρ out of the brackets. Furthermore, for steady state conditions, the velocity term q does not change and the two PDEs can be solved separately.

In the next two sections we describe the specifics of a simple solute tracer model and a variable density flow model, and elaborate on the methods applied to solve the discretized systems of equations.

2.1.1 Modeling of solute tracer movement

For the solute tracer model we assume fluid of a uniform density, therefore, we can rearrange equation (2.3) (Darcy's law), and use the formulation with hydraulic head and conductivity instead. Hydraulic head is essentially the sum of pressure and elevation head (potential)

and in unconfined aquifers it corresponds to the water level in the well:

$$h = \frac{p}{\rho g} + z. \quad (2.4)$$

After taking the density term ρg out of the brackets in Eq.(2.3) we obtain:

$$q = -\frac{k\rho g}{\mu}(\nabla \frac{p}{\rho g} + \nabla z) = -K \nabla h, \quad (2.5)$$

where K is hydraulic conductivity, which is equal to $\frac{k\rho g}{\mu}$ and has length per time units, $[L/t]$, unlike the permeability k which has $[L^2]$ units and is related to the architecture of the porous media only.

In this application we assumed steady state conditions. This assumption can not be generally applied, however, if we look closer at the time dependent term and consider the fluid to be compressible, we can apply chain rule and rewrite the time dependent term as:

$$\frac{\partial(\phi\rho)}{\partial t} = \phi \frac{\partial\rho(p)}{\partial t} + \rho \frac{\partial\phi(p)}{\partial t} = \phi \frac{\partial\rho}{\partial p} \frac{\partial p}{\partial t} + \rho \frac{\partial\phi}{\partial p} \frac{\partial p}{\partial t} = \left(\phi \frac{\partial\rho}{\partial p} + \rho \frac{\partial\phi}{\partial p} \right) \frac{\partial p}{\partial t}. \quad (2.6)$$

Letting α be the coefficient of (rock) matrix compressibility, $\alpha = \frac{\partial\phi}{\partial p}$, and β , the coefficient of fluid compressibility, $\beta = \frac{1}{\rho} \frac{\partial\rho}{\partial p}$; the specific storativity is then $S_s = \rho g(\phi\beta + \alpha)$ [6] and we can write the time dependent term for hydraulic head as

$$\left(\phi \frac{\partial\rho}{\partial p} + \rho \frac{\partial\phi}{\partial p} \right) \frac{\partial p}{\partial t} = \rho S \frac{\partial h}{\partial t} = \frac{1}{g} S_s \frac{\partial p}{\partial t} = \rho S_s \frac{\partial h}{\partial t}. \quad (2.7)$$

S_s , specific storativity, is the volume released (or added) from or to a unit volume of storage due to a unit decline (increase) in hydraulic head. The units are $[L^{-1}]$.

Since the solute tracer model is for flow of uniform density, after dropping out the density term and substituting (2.5) in (2.1) we obtain:

$$S_s \frac{\partial h}{\partial t} - \nabla \cdot (K \nabla h) = Q_{gw} \quad (2.8)$$

In confined aquifers specific storativity has fairly low values of order 10^{-3} or lower [92]. We can therefore neglect the time dependent term $S_s \frac{\partial h}{\partial t}$, when $|S_s \frac{\partial h}{\partial t}| \ll |Q_{gw}|$, i.e. the external sources representing pumping rates or boundary effects are much larger than changes due to hydraulic head decline (rise). This will be mostly the case for a short time scale and

confined aquifers with pumping tests.

The steady state fluid mass balance equation (2.8) thus becomes

$$-\nabla \cdot K \nabla h = Q_{gw} \quad (2.9)$$

Appropriate boundary conditions need to be defined, here we use Neumann and Dirichlet boundary conditions

$$h = h_{BC} \text{ at } \Gamma_D, \quad \vec{n} \cdot K \nabla h = 0 \text{ at } \Gamma_N. \quad (2.10)$$

h_{BC} is the fixed head along the boundary Γ_D , and a no-flux boundary is set for Γ_N . The groundwater linear velocity v , which is the velocity of solute moving in the subsurface, is defined as

$$v = \frac{1}{\phi} q = -\frac{1}{\phi} K \nabla h. \quad (2.11)$$

Now we can rearrange the solute mass balance equation (2.2), and take the density term out of brackets, which leads to a standard advection-diffusion equation for solute concentration c (replacing the $\rho\omega$ term). Assuming, that porosity ϕ does not change in time or vanish we obtain the following time dependent partial differential equation for c with groundwater velocity v :

$$\frac{\partial c}{\partial t} + \nabla \cdot (c v) - \nabla \cdot (D \nabla c) = Q_{sw}. \quad (2.12)$$

This is a standard advection-diffusion equation. Even though that in aquifer systems the groundwater velocity is fairly small, for the scenarios we consider (and model) in this work, it is the dominant process compared to dispersion.

Discretization and solution of the solute tracer model

Both governing equations (2.9) and (2.12) are discretized on staggered grids, with c and h placed in the cell centers and fluxes at the cell faces (see in Figure 2.1). The velocity field (specific discharge) q is computed at the cell faces to avoid long differences when computing the spatial gradient of h and improve accuracy of the discretization scheme. The cell faces values of porous media properties such as dispersion, hydraulic conductivity K or porosity, that are necessary to calculate the velocity v , are obtained in our model by harmonic averaging from the values in cell centers.

Discretization of the spacial derivatives is done using a finite volume approach. For

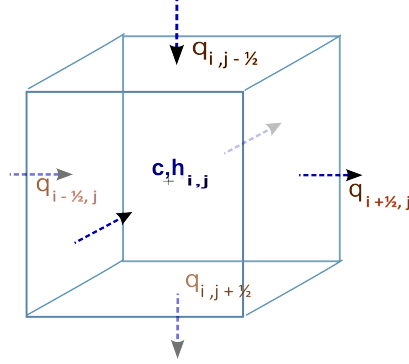


Figure 2.1: A single cell in the staggered grid of the discretized groundwater model, hydraulic head h and solute concentration c live in the cell centers, fluxes are computed at the cell faces.

time integration we use operator splitting, where we first solve the advective part with a Semi-Lagrangian integrator and then parabolic part with an implicit Euler method (for details see [37]). The discretized system for the solute tracer groundwater model is then:

$$A(\mathbf{K}) \mathbf{h} = \mathbf{q}_{gw} \quad (2.13)$$

$$\frac{c^{n+1} - S(\mathbf{v})c^n}{\Delta t} = A(\mathbf{D}) c^{n+1} + \mathbf{q}_{sc}, \quad (2.14)$$

$$\text{where } A(\mathbf{K}) = -\text{Div } \mathbf{A}_v(\mathbf{K}) \text{Grad}, \quad A(\mathbf{D}) = \text{Div } \mathbf{A}_v(\mathbf{D}) \text{Grad}$$

The matrices Div and Grad represent the divergence and gradient operators and $\mathbf{A}_v(\cdot)$ harmonically averages the values of a model property in the x, y and z direction from cell centers onto cell faces. $S(\mathbf{v})$ represents the Lagrangian push forward operator moving the solute along the flow lines given by velocity \mathbf{v} (discussed in the next paragraph), Δt is the time step size and external flux \mathbf{q}_{gw} accounts for the pumping rates and also the fixed head boundary effects. Similarly \mathbf{q}_{sc} represent the sink/source term for the solute.

The solution of fluid mass balance is straightforward; the hydraulic head h from Eq. 2.13 is simply obtained as

$$\mathbf{h} = A(\mathbf{K})^{-1} \mathbf{q}_{gw}, \quad (2.15)$$

which can be solved directly or by Conjugate Gradient method for large scale problems.

The solute mass balance equation (2.14) is solved by operator splitting. The choice of a Semi-Lagrangian method here for the advection part is motivated by the ability to take an arbitrary large time step which is especially important for inverse problems, where the

velocity field may not be known. Standard explicit techniques may require changing the time step during the inversion process which could lead to instabilities in the computation of the gradient.

Our Semi-Lagrangian method belongs to the family of modified methods of characteristic (MMOC) first introduced in [26]. The main advantages are in the alleviation of the Courant number restriction due to the Lagrangian advection step [16] and mass conservation. The Eulerian - Lagrangian scheme is also effective in overcoming numerical dispersion for advection dominated problems [89]. Similar approaches are taken for example by codes such as the MOC3D model for solute transport [58], or later MT3DMS for variable density flow in connection with Modflow [60, 62]. In the context of review on Eulerian-Lagrangian localized adjoint methods (ELLAM)[85] our approach is a finite difference Eulerian-Lagrangian type, where we do not solve the solute transport equation using an integral equation but instead use a projection matrix.

In our implementation, particles are placed at the cell centers at each time step and tracked forward. The solute content of each transported particle is interpolated to its neighboring cells yielding the solution at the next time step (see in Figure 2.2). The Lagrangian push forward operator $S(\mathbf{v})$ is thus formed at each time step by coefficients that interpolate the transported particles (cell centers) onto the neighboring cells.

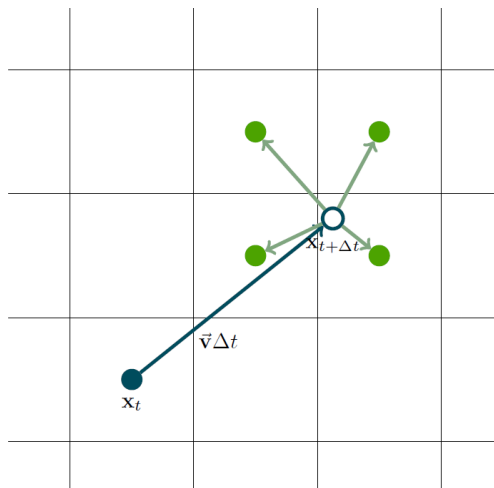


Figure 2.2: Visualization of the Semi-Lagrangian scheme in 2D: Interpolation of solute mass $\mathbf{x}_{t+\Delta t}$ which was advected from the cell center at \mathbf{x}_t to surrounding cells. We track the particles (cell centers) forward along the flowlines.

Afterward, we can add the dispersion step using Euler's method and equation (2.14) can be solved recursively in time as:

$$c^{n+1} = (I - \Delta t A(D))^{-1} (S(v)c^n + \Delta t q_{sc}). \quad (2.16)$$

Insight for Lagrangian methods

The basic idea behind Semi-Lagrangian methods can be well explained using a 1D advection equation with a fixed velocity:

$$\frac{\partial c}{\partial t} + v \frac{\partial c}{\partial x} = 0$$

The analytical solution is $c(x, t) = c_0(x - vt)$. Suppose we have a discretization over a uniform mesh where $x_i = i\delta x$ and $t^n = n\delta t$, the Lagrangian methods use this analytic solution to find c at time t^{n+1} as:

$$c(x_i, t^{n+1}) = c_0(x_i - v(n+1)\delta t) = c_0(x_i - v\delta t - vn\delta t) = c(x_i - v\delta t, t^n)$$

Similarly for

$$c(x_i, t^n) = c_0(x_i - v n\delta t) = c_0(x_i + v\delta t - v n\delta t) = c(x_i + v\delta t, t^{n+1})$$

For the Lagrangian methods we can therefore obtain an exact solution; however, at each time step we would have to change the mesh. The Semi - Lagrangian methods approximate instead the value based on the neighboring points using some interpolation technique. For 1D linear interpolation we can simply write c_i^{n+1} as:

$$c_i^{n+1} = \alpha c_{i-k-1}^n + (1 - \alpha) c_{i-k}^n$$

where

$$v \frac{\delta t}{\delta x} = k + \alpha, \quad k = \left\lfloor v \frac{\delta t}{\delta x} \right\rfloor.$$

For a 3D case we can proceed similarly, using trilinear interpolation, where the coefficients α and $1 - \alpha$ will create the matrix S and we can compute c at the next time step as

$$c^{n+1} = S c^n.$$

For a 3D domain with n cells in each direction, S is $n^3 \times n^3$ matrix containing the interpolation coefficients calculated using some interpolation procedure (e.g. linear interpolation leads to first order accuracy). The overall accuracy of the advection step depends on the chosen interpolation method when deriving the coefficients for the S matrix.

For the advection case a straightforward connection exist to the so called upwind scheme which is defined as:

$$c_i^{n+1} = c_i^n - v \frac{\delta t}{\delta x} \begin{cases} (c_{i+1}^n - c_i^n), & v < 0 \\ (c_i^n - c_{i-1}^n), & v \geq 0 \end{cases}$$

with the stability region $|v| \frac{\delta t}{\delta x} \leq 1$. Thus for $|v| \frac{\delta t}{\delta x} \leq 1$ the upwind scheme is the same as Semi-Lagrangian scheme above.

2.1.2 Variable density flow (VDF) model

The modeling of variable density flow (VDF) has various applications including contaminant transport, saline lakes hydrology, brine migration or nuclear waste disposal monitoring and any processes, where the fluid density changes with solute concentration or temperature. The physics of VDF can follow two very different processes. First, if the density of the fluid decreases with depth, or significantly denser fluid enters the system above lighter fluid, it may lead to unstable mixing processes (so called fingering) and for such cases the governing equations for VDF become highly nonlinear. On the other hand if the density increases with depth the process of mixing and flow is stable. This is the case for most groundwater systems where the density differs laterally but usually increases with depth [95]. In some case, for example salt tracer tests, the density changes are small enough not to effect the flow field and a standard solute transport model can be used instead.

VDF models are used in this study for seawater intrusion simulations, where the difference between freshwater and saltwater density is relatively small; however, the changes in the flow field due to solute dynamic still require the governing equations to be solved in a coupled manner.

For the variable density flow the situation time dependent term is a bit different than in the case of solute tracer model. We can again assume that porosity changes only with pressure, but the density now changes with both solute mass fraction and pressure, following the chain rule the term $\frac{\partial(\phi\rho)}{\partial t}$ can be written as

$$\frac{\partial(\phi\rho)}{\partial t} = \phi \frac{\partial\rho(p, \omega)}{\partial t} + \rho \frac{\partial\phi(p)}{\partial t} = \phi \frac{\partial\rho}{\partial\omega} \frac{\partial\omega}{\partial t} + \phi \frac{\partial\rho}{\partial p} \frac{\partial p}{\partial t} + \rho \frac{\partial\phi}{\partial p} \frac{\partial p}{\partial t} \quad (2.17)$$

$$= \phi \frac{\partial\rho}{\partial\omega} \frac{\partial\omega}{\partial t} + \left(\phi \frac{\partial\rho}{\partial p} + \rho \frac{\partial\phi}{\partial p} \right) \frac{\partial p}{\partial t}. \quad (2.18)$$

Similarly as in section 2.1.1 we can rewrite the fluid mass balance equation (2.1) using specific mass storativity $S_p^m = \rho(\alpha + \phi\beta) = \frac{1}{g}S$ as [6]:

$$\phi \frac{\partial\rho}{\partial\omega} \frac{\partial\omega}{\partial t} + S_p^m \frac{\partial p}{\partial t} + \nabla \cdot (\rho q) = \rho Q_{gw} \quad (2.19)$$

For confined aquifers we can expect $\left| S_p^m \frac{\partial p}{\partial t} \right| \ll |\rho Q_{gw}|$. The first term is equal to $\phi\rho\gamma \frac{\partial\omega}{\partial t}$, where γ is introduced in the state equation bellow (Eq.(2.22)) and for saltwater-freshwater density difference it is usually bellow 0.025. Therefore in many cases $\left| \phi\rho\gamma \frac{\partial\omega}{\partial t} \right|$ will be much

smaller than $|\rho Q_{gw}|$ and the steady state assumption can be justified.

The governing equations for variable density flow, with steady state assumption for pressure, are then

$$\nabla \cdot (\rho q) = \rho Q_{gw}, \quad \text{with } q(\rho) = -\frac{k}{\mu}(\nabla p + \rho g \nabla z), \quad (2.20)$$

$$\frac{\partial(\phi \rho \omega)}{\partial t} + \nabla \cdot (\rho \omega q) - \nabla \cdot (\phi \rho D \nabla \omega) = Q_{sw}. \quad (2.21)$$

We complete the system with the linearized state equation between fluid density ρ and solute mass fraction ω :

$$\rho = \rho_F(1 + \gamma \omega) \quad \text{with } \gamma = \frac{\rho_S - \rho_F}{\rho_F}, \quad (2.22)$$

where ρ_F is the freshwater and ρ_S the saltwater density.

Additional state equations can be considered for modeling VDF, the effect of pressure and temperature changes on density or the effect of solute content on viscosity μ . However, for our application and under isothermal conditions, the viscosity changes can be neglected and the solute content dynamic will have a much higher effect on density than pressure changes. Another simplification of our model involves keeping the hydrodynamic dispersion tensor D fixed, i.e. not dependent on Darcy's velocity q , which slightly reduces the computational burden, when solving the coupled governing PDEs iteratively. Still, using a full variable density flow model, as for example in [57], would not change the approaches described in the following chapters regarding solving the coupled inverse problem.

The two PDEs (2.20) and (2.21) are coupled via the velocity term q which is dependent on density ρ , respectively the solute mass fraction ω . The forward VDF model is therefore nonlinear and both equations need to be solved together. We can again apply a finite volume approach for spatial derivatives; averaging, gradient and divergence operators to discretize the fluid mass balance equation, which becomes:

$$\text{Div } R_{KM} (\text{Grad } p^n + (A_v \rho^n) \odot \mathbf{g}) = \rho^n \odot Q_{gw} \quad (2.23)$$

where $R_{KM} = \text{diag} \left(k \odot A_v \left(\frac{\mu}{\rho} \right)^{-1} \right)$, $\mathbf{g} = -g \text{ Grad } z$.

We use the Hadamard product $\mathbf{a} \odot \mathbf{b}$ for the element wise product of two vectors and A_v matrix operator for harmonic averaging from cell centers onto cell faces. The ad-script n

stands for the corresponding hydrological state at the $n - th$ time step. For now, assume that we know the density ρ at the n^{th} time step, the pressure p^n can be then solved directly

$$p^n = (-\text{Div } R_{KM}\text{Grad})^{-1} (\text{Div } R_{KM} (A_v \rho^n) \odot g - \rho^n \odot Q_{gw}), \quad (2.24)$$

by using Cholesky decomposition for matrix $-\text{Div } R_{KM}\text{Grad}$.

Given the pressure p^n we can compute the groundwater linear velocity v^n at the cell faces:

$$v^n = -\text{diag} \left(A_v \left(\frac{\mu\phi}{k} \right) \right)^{-1} (\text{Grad } p^n + (A_v \rho^n) \odot g). \quad (2.25)$$

For the solute mass balance equation (2.21) we can again apply operator splitting; however, it is not the solute concentration c this time but the mass of the particle $\rho\omega$ which is tracked forward during the advective step. The discretized form is then

$$\begin{aligned} \frac{(\rho \odot \omega)^{n+1} - S^n(\rho \odot \omega)^n}{\Delta t} &= \text{Div } A(D, \rho^{n+1}) \text{Grad } \omega^{n+1} + Q_{sw} \\ \text{with } A(D, \rho^{n+1}) &= \text{diag} \left(A_v \frac{1}{D \odot \rho(\omega^{n+1})} \right)^{-1}. \end{aligned} \quad (2.26)$$

Here again S^n represent the Semi-Lagrangian operator, containing the interpolation weights based on velocity field v^n . First, we integrate the advection step explicitly, obtaining some temporary solute mass $(\rho \odot \omega)^*$:

$$(\rho \odot \omega)^* = S^n(\rho \odot \omega)^n \quad (2.27)$$

Using the state equation (2.22), we can solve a local quadratic equation for ω^* , noting that only one root of the equation makes physical sense. Having the solution ω^* , we can now integrate the diffusion part, starting from ω^* with an implicit Euler method as:

$$(\rho \odot \omega)^{n+1} = (\rho \odot \omega)^* + \Delta t \text{Div } A(D, \rho^{n+1}) \text{Grad } \omega^{n+1} + Q_{sw} \quad (2.28)$$

The implicit diffusion step is nonlinear and is solved using a Picard iteration [2], updating the velocity field v^n and corresponding ω^* . For variable density flow with seawater, the density difference between the two fluids is fairly small, decreasing the nonlinearity of the coupled system and the number of Picard iterations (see the Algorithm 1). Even though the time step can be large given the stability of the Semi - Lagrangian method, care must

be taken with respect to the coupling with the flow equation [81]. Too large of a step would lead to a weak coupling and possibly erroneous calculations.

Algorithm 1 Picard scheme

Initialize $\omega_1^{n+1} = \omega^n, \rho_1^{n+1} = \rho^n$

For $k = 1$ to $iter_{max}$

- Calculate of pressure field: $p_k^{n+1} = f(\omega_k^{n+1})$;
 - Update velocity field: $v_{k+1}^{n+1} = -\frac{k}{\mu}(\nabla p_k^{n+1} + \rho_k^{n+1}g\nabla z)$
 - Advection step: $(\rho \odot \omega)^* = S^n(\rho \odot \omega)^n$
 - Dispersion step: $(\rho \odot \omega)_{k+1}^{n+1} = (\rho \odot \omega)^* + \Delta t \text{Div } A(D, \rho^*) \text{ Grad } \omega_{k+1}^{n+1} + Q_{S\omega}$.
 - Update pressure field given the new solute mass fraction: $p_{k+1}^{n+1} = f(\omega_{k+1}^{n+1})$
 - Check the error: $\|p_{k+1}^{n+1} - p_k^{n+1}\| < tol$ break else Step1
-

2.1.3 Testing the GW models

To verify the developed groundwater models, we first tested numerically the discretization errors. We computed the first and second derivatives for a known solution, which was then compared with the model result for a decreasing grid size. From the hydrogeological point of view we tested our model simulations against a classical benchmark problem for VDF and known solutions for a 1D advection diffusion equation in case of solute transport.

If we fix the velocity field for the system of equations in the solute tracer model, analytical solutions exist for the solute mass balance equation (2.12), either for advection only or with some specific initial conditions also for advection-diffusion process. Therefore, we can compare our model results with this analytical solution and also evaluate the accuracy of Semi-Lagrangian method against the Lax-Friedrich scheme. In a simple experiment we set the hydraulic head boundary conditions to be Dirichlet for the inflow and outflow, implying a uniform velocity field along the x axis. With such a setup the solute with a fixed concentration equal to 1 at the inflow moves with a steady velocity from left to right, and without any dispersion we would have a sharp interface. We solved this essential 1D advection problem with our 3D model for different time steps using both Semi-Lagrangian and Lax-Friedrich methods. The results (profiles of the concentration profiles) are shown in Figure 2.3, confirming the stability and lower numerical diffusion of the Semi-Lagrangian method.

To test the VDF model, we run our code for the Henry problem [43] which is a classical benchmark problem for VDF in 2D representing a simplified seawater intrusion case.

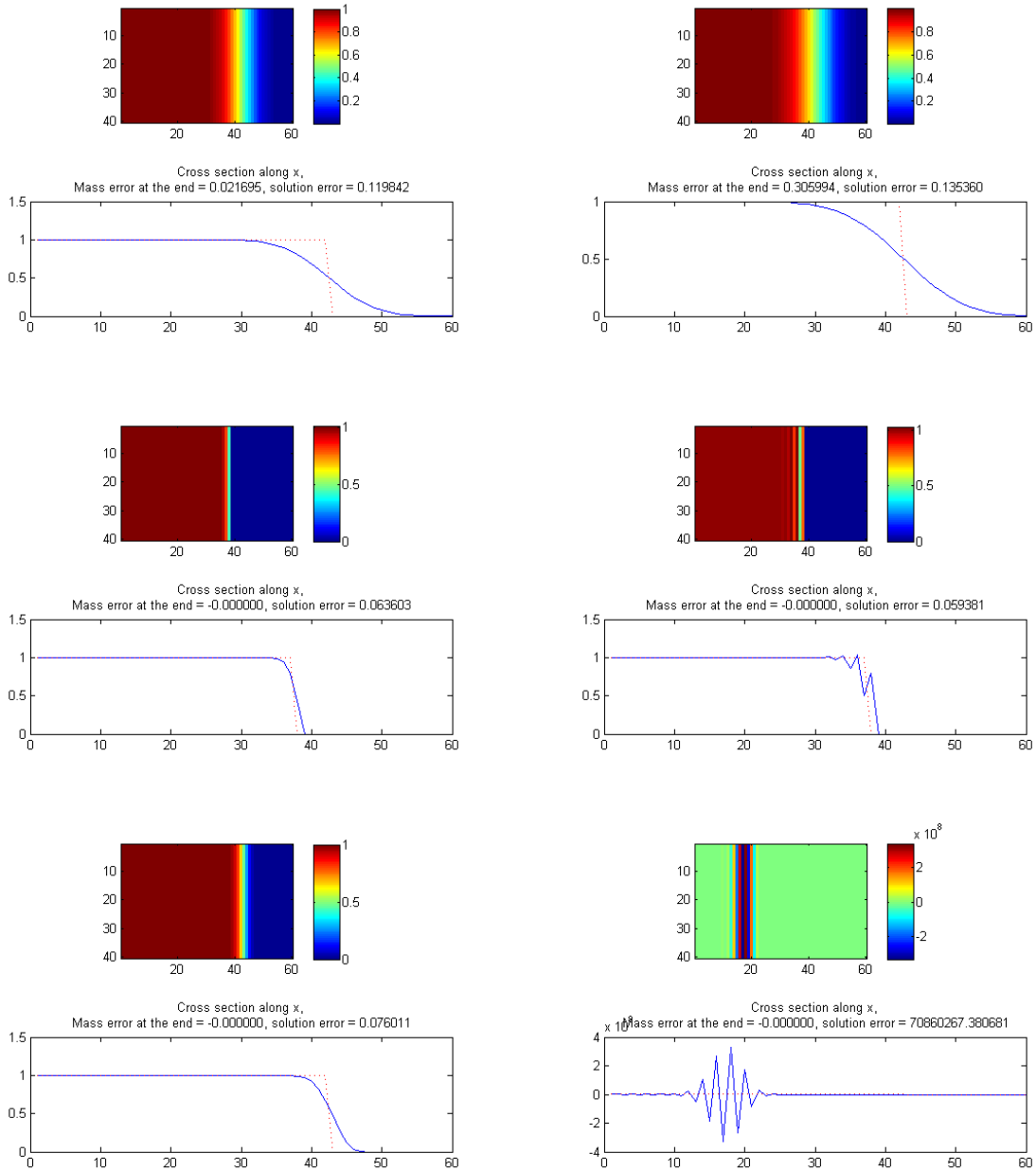


Figure 2.3: Test against analytical solution for advective transport: Semi-Lagrangian method (left) vs Lax-Friedrich implicit scheme (right). Simulations were run for three different time steps, from top to bottom, $t = 15, 40$ and 80 days, corresponding to Courant number $0.33, 1$ and 1.33 . The solid line is the modeled break through curve and the dashed one is the analytic solution.

The boundary conditions are set as impermeable on the top and bottom of the domain, the inland boundary is set as fixed freshwater inflow, and the seaside boundary is fixed hydrostatic pressure based on the seawater interface (see in Figure 2.4). We used the dimensionless parameters $a = 0.3214$ and $b = 0.1$ as in [1], and obtained similar results as in their study for a diffusive case of the Henry problem, i.e. when only molecular diffusion is consider with a fixed value for D and transverse and longitudinal dispersivities being zero (see in Figure 2.5).

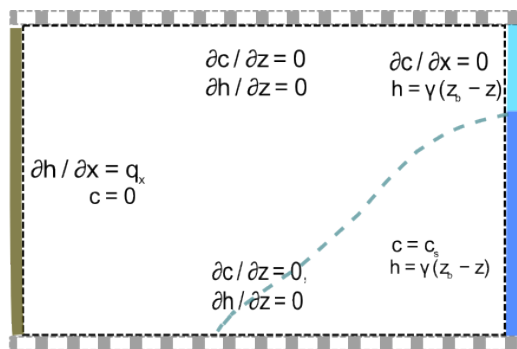


Figure 2.4: The boundary conditions setup for a Henry’s benchmark problem, seawater boundary is on right, freshwater inflow on the left.

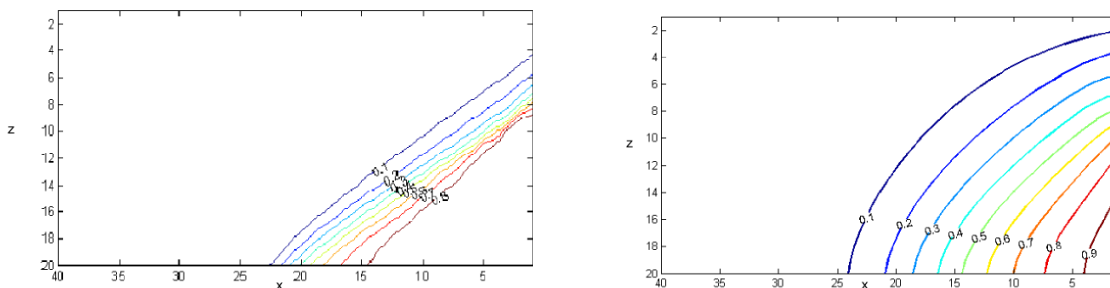


Figure 2.5: Contour plots for two cases of testing the Henry’s benchmark problem representing the steady state solutions for solute mass fraction. Left: the dimensionless parameters $a = 0.33, b = 0.01$; right: $a = 0.33, b = 0.1$, which correspond to the solutions in [1]

2.2 Geophysical modeling

2.2.1 Direct current resistivity survey

In order to estimate the physical properties of the porous media, we choose direct current (DC) resistivity, also referred to as Electrical Resistance Tomography (ERT). DC resistivity is sensitive to the electrical conductivity of the media. Since the conductivity of saltwater is a few orders of magnitude larger than that of freshwater, the DC resistivity method is often a natural choice, where the fluid conductivity changes as a result of the solute dynamic. Moreover, DC has several advantages when compared to other electromagnetic methods: relatively easy and inexpensive data acquisition and minimal computational effort.

In DC experiments, a current is injected into the ground creating an electrical potential distribution, which is then measured using pairs of electrodes placed on or under the surface (Figure 2.6). Multiple receiver and source electrodes can be utilized in a surface survey, creating many options for the experimental design scheme, with the goal of capturing the variability of the 3D subsurface conductivity distribution.

To model this process, we used the steady state form of Maxwell's equations:

$$\begin{aligned} \nabla \cdot (-\sigma \nabla \varphi) &= \mathbf{I}(\delta(\mathbf{r} - \mathbf{r}_{s+}) - \delta(\mathbf{r} - \mathbf{r}_{s-})) \\ \mathbf{n} \cdot \nabla \varphi &= 0 \quad \text{on } \Gamma_{nc} \end{aligned} \tag{2.29}$$

where σ represents the media's electrical conductivity, φ is the electric potential, \mathbf{I} is the current source, δ is a Dirac delta function and $r_{s+,s-}$ stands for the location of positive and negative current electrodes. The boundary conditions were set as no flux across the boundaries, Γ_{nc} . When solving the forward problem, the electrical conductivity model, σ , is known and potentials everywhere can be calculated using a finite volume approach on a 3D grid. Since the discretized DC equation is essentially the same type of equation (Poisson equation) as the flow equation (2.13), we follow the same procedure to solve it as it has already been described in section 2.1.1. The cell-centered finite volume approach for the discretization of the problem leads to a linear system of equations:

$$\begin{aligned} \mathbf{A}(\boldsymbol{\sigma})\mathbf{u} &= \mathbf{q} \\ \text{where } \mathbf{A}(\boldsymbol{\sigma}) &= -\text{Div} \text{diag} \left(\frac{1}{(\mathbf{A}_v \boldsymbol{\sigma}^{-1})} \right) \text{Grad}. \end{aligned} \tag{2.30}$$

The electrical conductivity σ is averaged harmonically from the cell centers onto cell faces (via matrix operator A_v), q is the source term and u represents the potentials. The forward model solves for the potential everywhere given a conductivity model. Using a data projection matrix Q_e , we obtain observed data

$$\mathbf{d}_e = Q_e \mathbf{u} \quad (2.31)$$

measured at the receivers.

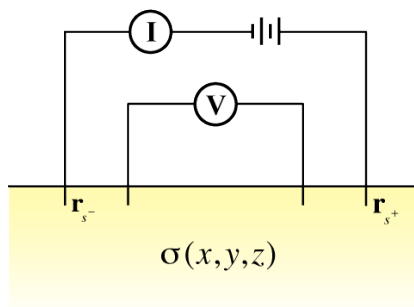


Figure 2.6: DC survey scheme for a single source and receiver.

2.2.2 Time domain electromagnetic survey (TDEM)

All electromagnetic surveys employ the induction effect that creates magnetic field due to changes in electric field and vice versa. The way how the changes are initiated and the data are recorded give different type of surveys, here though, we focus just on one specific type that leads to a particular set of governing equations and following discretization of the electromagnetic process.

In our experiments, a direct current runs through the transmitter loop to create a steady-state magnetic field. The current is then abruptly shutoff, causing a rapid change in magnetic field, which induces so called eddy currents that flow in electrically conductive bodies in the subsurface. These eddy currents will generate secondary magnetic fields that can be measured by receivers at the earth surface. Similarly as DC resistivity, TDEM survey is thus sensitive to changes in electrical conductivity of the subsurface.

Maxwell's equations for the electric field e and magnetic density b , where we already

substitute in the constitutive relations, can be written as:

$$\nabla \times e + \frac{\partial b}{\partial t} = 0 \quad (2.32)$$

$$\nabla \times \mu^{-1}b - \sigma e - \epsilon \frac{\partial e}{\partial t} = s_r(t) \quad (2.33)$$

and BC:

$$\vec{n} \times b = 0, \quad b(0, x) = b^0, \quad e(0, x) = 0 \quad (2.34)$$

where e is the electric field, b is the magnetic flux, μ represents the magnetic permeability, σ is the electrical conductivity, ϵ electrical permittivity and s_r is the source current. The first equation is often referred to as Maxwell's Faraday equation, and the second one as Ampere's law.

We can apply the quasi static approximation here due to the initial shutoff of the source. Since the permittivity ϵ is very low and we can assume small changes of electric field e , the term $\epsilon \frac{\partial e}{\partial t}$ can be dropped out and for $t > 0$ (after the current shutoff) we can simplify the equation (2.33) to:

$$\nabla \times \mu^{-1}b - \sigma e = 0 \quad (2.35)$$

Discretization and solving the forward model

After elimination of b in Eq.(2.35) by substituting e from Eq.(2.32), we can write:

$$\nabla \times \mu^{-1} \nabla \times e - \sigma \frac{\partial e}{\partial t} = 0, \quad (2.36)$$

where the only unknown is the electric field e .

Using a staggered grid, the discretized form of the governing equations (2.32) and (2.36) in time is then:

$$C e^n + \alpha(b^n - b^{n-1}) = 0 \quad (2.37)$$

$$C^T M(\boldsymbol{\mu})^{-1} C e^n + \alpha M(\boldsymbol{\sigma}) e^n = \alpha M(\boldsymbol{\sigma}) e^{n-1} \quad (2.38)$$

$$\text{where } M(\boldsymbol{\mu}) = \text{diag} (A_f \boldsymbol{\mu}^{-1}) \quad M(\boldsymbol{\sigma}) = \text{diag} (A_v \boldsymbol{\sigma}).$$

The electric field is placed on the edges and the magnetic density occurs on the cell faces (see in Figure 2.7). C is the curl matrix operator, $\alpha(i)$ is $\frac{1}{\delta t}$ and A_e, A_v correspond to averaging matrix operators from cell centers onto edges and cell faces respectively.

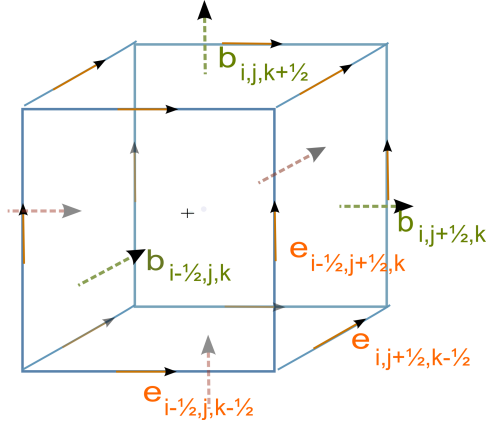


Figure 2.7: Staggered discretization for the TDEM model, properties such as permeability μ and electrical conductivity σ are at the cell centers, magnetic field b is computed at the cell face and electric field e on edges.

In order to proceed with the forward calculation in time, we need to know the initial field e^0 and magnetic flux b^0 . The initial magnetic field is calculated using the Biot-Savart law and integrating over the current ellipse (loop). Substituting into Eq.(2.35) we obtain the initial electric field as

$$e^0 = M(\sigma)^{-1}(C^T M(\mu)b^0).$$

Once we have the initial fields, we need to solve the time dependent Eq.(2.38) for e , at each time step we thus solve the following system for e^{i+1} :

$$\left(C^T M(\mu) C + \alpha_i M(\sigma)\right) e^{i+1} = \alpha_i M(\sigma) e^i$$

This system is solved with the Conjugate Gradient method, for which we implemented the A-phi preconditioner [37]. The magnetic density at $i + 1^{th}$ time step is obtained directly from Eq.(2.37) as

$$b^{i+1} = b^i - \frac{1}{\alpha_i} C^T e^{i+1}.$$

The “measured data”, changes in magnetic field are then:

$$d^i = Q C e^{i+1}, \tag{2.39}$$

where the projection matrix Q interpolates the data from the cell faces onto receivers

locations.

Both geophysical models were tested using artificial sources. These were analytically derived based on known conductivity fields, which could be then compared against model solutions.

Chapter 3

Inverse problem for a single model

The focus of this work is on the joint inversion of two different data sets. However, before we start to explore the beauty of joint inversion, it is worthwhile to at least briefly summarize solving the inverse problem for a single data set since it is a building block for any coupled minimization scheme. We restrict the two following sections to a general solution of an inverse problem for a single model, but leave some space to discuss specifics related to each, groundwater and geophysical, type of data. In the last section of this chapter we derive the data sensitivities, which are necessary if we want to proceed with any type of Newton method for a single or coupled inversion.

3.1 Ill-posedness and regularization

Usually the data we collect provide some indirect, less often direct, information about the model we are trying to recover. One could try to estimate this model by considering only the data alone and minimize the norm of the data residuals:

$$\min_{\mathbf{m}} \Phi = \frac{1}{2} \|\mathbf{Q} \mathbf{F}(\mathbf{m}) - \mathbf{d}_{obs}\|^2, \quad (3.1)$$

where $\mathbf{F}(\mathbf{m})$ is some forward model operator, e.g. mapping the model \mathbf{m} to hydrological states or geophysical potentials (and most likely involving some inverse matrix computation), matrix \mathbf{Q} projects the simulated groundwater or geophysical states onto the data locations and the vector \mathbf{d}_{obs} represents the observed data for some groundwater or geophysical states which are dependent on the model \mathbf{m} that we are trying to recover. Lets assume a linear case, where we can write $\mathbf{A}\mathbf{m} = \mathbf{Q}\mathbf{F} \mathbf{m}$, the least square solution of Eq. (3.1)

would then give $\hat{\mathbf{m}}$ [66]:

$$\hat{\mathbf{m}} = (\mathbf{A}^\top \mathbf{A})^{-1} \mathbf{A}^\top \mathbf{d}_{\text{obs}} \quad (3.2)$$

If the data are coming from some physical experiment, are scarce and contain measurement errors, the minimization will rarely lead to success. Moreover, the forward operator $\mathbf{F}(\mathbf{m})$ can behave well for a simple groundwater model but it is rarely well behaved for geophysical modeling. With indirect data for \mathbf{m} , the matrix $(\mathbf{A}^\top \mathbf{A})$ may not be invertible. Even if we obtain direct GW data, for example solute concentration, the \mathbf{Q} operator has nonzero entries only for few data location points in the observation wells, making the recovery of a full 3D model difficult (i.e. nonunique solution).

Both groundwater and geophysical data provide only a limited “picture” of the subsurface, whereas we want to recover a full 3D model, whether it is solute concentration or soil bulk conductivity. Therefore, we need to add some a-priori information to limit the solutions to physically realistic estimates, which are hopefully close to the true ones. This can be achieved using regularization. The inverse problems are usually regularized by assuming that the model (estimate) should be close to some reference model, which can be simply an initial guess or derived from geological information. Clearly, the way we choose our a-priori information and incorporate it in the regularization will have a huge impact on the final estimate.

If we set $\mathcal{R}(\cdot)$ to be some regularization operator and Σ to be the covariance matrix based on measurement errors and the norm $\|r\|_{\Sigma^{-1}}^2 = r^\top \Sigma^{-1} r$, we can obtain the maximum-a-posteriori estimate of the model \mathbf{m} by minimizing the following functional:

$$\min_{\mathbf{m}} \Phi = \frac{1}{2} \|\mathbf{Q} \mathbf{F}(\mathbf{m}) - \mathbf{d}_{\text{obs}}\|_{\Sigma^{-1}}^2 + \alpha \mathcal{R}(\mathbf{m}), \quad (3.3)$$

The regularization parameter, α , should be chosen in such a way that the inversion is guided by the data misfit term. In other words, we prefer the data to be the steering mechanism in the minimization rather than the a-priori information, which may be biased or incorrect. The parameter α can be set by a trial and error or by Cross-Validation [37].

Since the model to be estimated in our application is based on differing fluid conductivity we do not expect to have sharp boundaries due to dispersion in porous media. Therefore, for our application, L_2 quadratic regularization turned out to be a good choice, as it favors

smooth solutions. After discretization the quadratic $\mathcal{R}(\mathbf{m})$ gives

$$\mathcal{R}(\mathbf{m}) = \frac{1}{2} \|\mathbf{L}(\mathbf{m} - \mathbf{m}_{ref})\|^2, \quad (3.4)$$

where \mathbf{L} is the gradient operator, and \mathbf{m}_{ref} is the reference model. The matrix operator \mathbf{L} consists of gradient fields in x, y and z directions; $\mathbf{L} = [\alpha_x \text{Grad}_x \ \alpha_y \text{Grad}_y \ \alpha_z \text{Grad}_z]^\top$, and each of the components can be proportionally decreased or increased if one expects more smoothness in a particular direction. For example, in the case of seawater intrusions with solute coming from the seaward boundary, the variation along this boundary can be penalized more than other directions. The selection of the reference model is up to personal preference, in geophysics a uniform model is a popular option, unless we have more information about the geology. The reference model can be also updated during the iterative minimization process.

An important thing to note here is that often we do not estimate the conductivity or solute concentration directly but rather estimate some function of \mathbf{m} . For example $f(\mathbf{m}) = \exp(\mathbf{m})$ ensures that the resulting field attain only positive values. In the case of seawater intrusion modeling the $\tanh(x)$ function turned out to be useful to parametrize the solute concentration. The electrical conductivity, resp. solute fraction, was modeled as

$$\sigma = 1 - \tanh(\mathbf{m}),$$

where \mathbf{m}_{ref} varies only along x coordinate (flow direction) and is bounded so that σ stays attains only positive values. In Figure 3.1 we show a slice through the reference model along the x axis, the reference model \mathbf{m}_{ref} increases gradually along the x direction, while the resulting σ_{ref} mimics the seawater intrusion expected profile (i.e. solute coming from the left seaward boundary).

3.2 Gauss-Newton method

Let us recall the objective function in equation (3.3), after substituting the quadratic regularization for \mathbf{m} we have:

$$\Phi(\mathbf{m}) = \frac{1}{2} \|\mathbf{Q} \mathbf{F}(\mathbf{m}) - \mathbf{d}_{obs}\|_{\Sigma^{-1}}^2 + \frac{\alpha}{2} \|\mathbf{L}(\mathbf{m} - \mathbf{m}_{ref})\|^2,$$

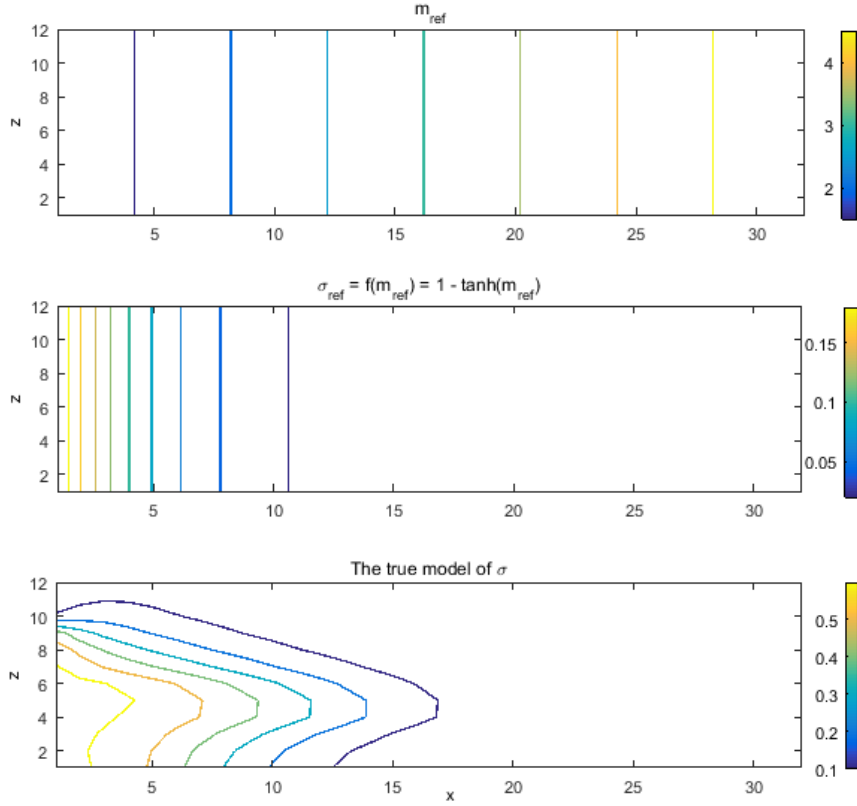


Figure 3.1: The reference model for SWI inverse problem. The resulting conductivity σ_{ref} has high solute mass fraction along the seaward boundary on the left, as expected in real conditions.

which can be minimized by a Gauss-Newton method. The gradient of $\Phi(\mathbf{m})$ is then

$$\mathbf{g}_m = \mathbf{J}^\top \mathbf{W}^\top \mathbf{W} (\mathbf{F}(\mathbf{m}) - \mathbf{d}_{obs}) + \alpha \mathbf{L}^\top \mathbf{L} (\mathbf{m} - \mathbf{m}_{ref}), \quad (3.5)$$

where \mathbf{J} represents the sensitivity of data with respect to model \mathbf{m} , $\mathbf{J} = \frac{\partial \mathbf{F}(\mathbf{m})}{\partial \mathbf{m}}$, and $\mathbf{W} = \text{diag}(\hat{\sigma}^{-1}) \mathbf{Q}$. The Hessian can be approximated by

$$\mathbf{H}_m = \mathbf{J}^\top \mathbf{W}^\top \mathbf{W} \mathbf{J} + \alpha \mathbf{L}^\top \mathbf{L}. \quad (3.6)$$

The computation of the sensitivities \mathbf{J} is the subject of the following section.

At each iteration we update the estimate \mathbf{m}^k by a step in the direction:

$$\mathbf{s}_k = -\mathbf{H}_m^{-1} \mathbf{g}_m, \quad (3.7)$$

which is solved using a preconditioned conjugate gradient (CG) method. The advantage of a CG method is that it does not require computing the gradient or Hessian explicitly, only matrix vector products need to be computed. The CG method thus eases the computational burden especially for large scale problems or when solving the problem on a fine scale. For further acceleration of the iterative process it is wise to choose a good preconditioner; for a single type of data we used an approximation of the inverse of $\frac{\partial^2 R(\mathbf{m})}{\partial \mathbf{m}^2}$, the regularization part in Hessian. The step size μ is determined afterward using an Armijo line search [75] giving the update for \mathbf{m} as:

$$\mathbf{m}^{k+1} = \mathbf{m}^k + \mu \mathbf{s}_k. \quad (3.8)$$

The number of iterations differs for groundwater and geophysical data, as the problems have different convergence behavior.

3.3 Sensitivities

To apply any type of Newton method, we need to know the sensitivities, or so called Jacobians, of collected data with respect to parameters or states of interest. In this section we show how to derive them analytically based on the discretized systems of equations, using a closed form formula. Such analytically derived sensitivities enable us to speed up the inversion process and ease the computational burden.

For the solute transport model (the system of governing equations was presented in the section 2.1.1) we need to compute the groundwater data sensitivities: $\frac{\partial \mathbf{c}}{\partial \mathbf{m}}$ and $\frac{\partial \mathbf{h}}{\partial \mathbf{m}}$, where \mathbf{m} represents either hydraulic conductivity \mathbf{K} or initial solute concentration \mathbf{c}^0 .

The derivation of sensitivities of hydraulic heads \mathbf{h} w.r.t. hydraulic conductivity \mathbf{K} is quite straightforward, the fluid mass balance in Eq.(2.13) can be rewritten as $F(\mathbf{K}, \mathbf{h}) = 0$ and differentiating w.r.t. \mathbf{K} we obtain

$$\frac{\partial F}{\partial \mathbf{K}} + \frac{\partial F}{\partial \mathbf{h}} \frac{\partial \mathbf{h}}{\partial \mathbf{K}} = 0.$$

Rearranging, we have

$$\frac{\partial h}{\partial K} = - \left(\frac{\partial F}{\partial h} \right)^{-1} \frac{\partial F}{\partial K} = -A(K)^{-1} \text{Div} \text{diag} (\text{Grad } h) A_v. \quad (3.9)$$

The sensitivities of solute concentration data w.r.t. initial solute c^0 can be solved recursively from the discretized equation (2.14):

$$\frac{\partial c^{n+1}}{\partial c^0} = (I - \Delta t A(D))^{-1} S \frac{\partial c^n}{\partial c^0}. \quad (3.10)$$

Jacobian w.r.t to the initial conditions, c^0 , is therefore solved as a by-product when performing the forward calculations. The adjoint can be solved similarly by a backward time stepping process.

It is important to note that by using Krylov subspace methods (CG in particular) for solving the direction update in Gauss-Newton method (Eq.(3.7)), we do not need to store the explicit sensitivity matrix J and can instead work only with matrix-vector products: Jv and adjoint $J^T w$.

In particular, for a given vector v and sensitivity $\frac{\partial c^n}{\partial c^0}$, at each k^{th} step we first calculate $S \frac{\partial c^{k-1}}{\partial c^0} v$, then we solve a linear system $(I - \Delta t A(D)) \mathbf{x} = S \frac{\partial c^n}{\partial c^0} v$ for \mathbf{x} at each time step, and the solution \mathbf{x} at the last time step gives Jv . Similarly for the adjoint product $J^T w$, we start from the last time step and solve system $(I - \Delta t A(D))^T \mathbf{y} = w$, and then multiply the solution \mathbf{y} by S^T . After all backward time stepping we obtain $J^T w$. Therefore, for the sensitivity computation we only need to solve a linear system corresponding to the size of vector c^n .

For the variable density flow model (section 2.1.2) the system of governing equations is nonlinear, which complicates the sensitivity derivation. One way to look at it is that during the forward simulation we solve the system of two partial differential equations, and at the end of each time step the pressure p^n is given by the solute distribution and boundary conditions. The groundwater velocity v^n can be therefore expressed as a function of ω^n and p^n only and the system thus reduces to the second equation for solute transport (2.26).

For the sake of simplicity, lets proceed using the solute mass fraction formulation alone, the time stepping process in equation (2.26) can be then written as

$$(I - \Delta t A(D)) \omega^n - S^{n-1} \omega^{n-1} - \Delta t q_{BC,ex}^{n-1} = 0. \quad (3.11)$$

Due to the operator splitting approach, we can explicitly derive the sensitivity of the mass ω^{n+1} at each time step with respect to ω^n , the solute fraction at the previous time step. This is a two step calculation, step 1 being the advection part and step 2 being the diffusion part. The sensitivity of the final solute fraction can therefore be calculated recursively during the forward groundwater model run. However, unlike in the solute transport case, the Semi-Lagrangian matrix operator S^n is now dependent on velocity v^n , which is dependent on ω^n . This extra term makes the derivation more tedious.

Let T^n be the sensitivity of $S^n(\rho\omega)^n$ with respect to spatial coordinates:

$$\mathsf{T}^n = \frac{\partial(S^n(\rho\omega)^{fixed,n})}{\partial x_i}.$$

The sensitivity of the advected mass w.r.t ω^0 can be then expressed as

$$\frac{\partial(\rho\omega)^{n+1,ad}}{\partial\omega^0} = S^n \frac{\partial(\rho\omega)^n}{\partial\omega^0} + \Delta t \mathsf{T}^n \frac{\partial v^n}{\partial\omega^0}. \quad (3.12)$$

The sensitivity of $\frac{\partial v^n}{\partial\omega^0}$ can also be (after some work) expressed as linearly dependent on $\frac{\partial(\rho\omega)^n}{\partial\omega^0}$ since v^n is a function of pressure p^n and density ρ^n and thus the term $\frac{\partial(\rho\omega)^{n+1,ad}}{\partial\omega^0}$ can be solved recursively.

More generally, we can also consider all time steps together:

$$\mathsf{F}(\omega) = \begin{pmatrix} I - \Delta t A(D) & & & & \\ -S^1 & I - \Delta t A(D) & & & \\ & -S^2 & I - \Delta t A(D) & & \\ & & \dots & & \\ & & & -S^{n-1} & I - \Delta t A(D) \end{pmatrix} \begin{pmatrix} \omega^1 \\ \omega^2 \\ \dots \\ \omega^n \end{pmatrix} - \begin{pmatrix} S^0 \\ 0 \\ \dots \\ 0 \end{pmatrix} \omega_0 - \Delta t \begin{pmatrix} q_{BC,ex}^1 \\ q_{BC,ex}^2 \\ \dots \\ q_{BC,ex}^n \end{pmatrix} = 0,$$

We can then write the forward model in a compact form as

$$\mathsf{A}_{\mathsf{T}\mathsf{S}}\omega - \mathsf{B}_0\omega_0 - \hat{q} = 0, \quad (3.13)$$

where $\mathsf{A}_{\mathsf{T}\mathsf{S}}$ is the time stepping matrix that is block bidiagonal and B_0 is the matrix that multiplies ω_0 . The vector \hat{q} involves the boundary conditions and sources and vector ω is set here as $\omega = [\omega_1^\top, \dots, \omega_n^\top]^\top$.

Differentiating F with respect to ω_0 we obtain that

$$\frac{\partial F(\omega, \omega_0)}{\partial \omega} \frac{\partial \omega}{\partial \omega_0} + \frac{\partial F(\omega, \omega_0)}{\partial \omega_0} = 0, \quad (3.14)$$

and therefore

$$\frac{\partial \omega}{\partial \omega_0} = -\frac{\partial F(\omega, \omega_0)}{\partial \omega}^{-1} \frac{\partial F(\omega, \omega_0)}{\partial \omega_0}. \quad (3.15)$$

Using (3.13) we see that sensitivity J is

$$\frac{\partial \omega}{\partial \omega_0} = A_{TS}^{-1} B_0. \quad (3.16)$$

Since in our synthetic examples we collect data only for the last time step, we compute the sensitivities recursively during the forward simulation.

In a similar way, the sensitivities of magnetic flux changes with respect to the conductivity σ are solved recursively during the time stepping process. Differentiating the first governing equation (2.37) for the time domain electromagnetic modeling (which is not directly dependent on σ) we can write:

$$C \frac{\partial e^n}{\partial \sigma} + \alpha \left(\frac{\partial (b^n - b^{n-1})}{\partial \sigma} \right) = 0. \quad (3.17)$$

Afterward, if we differentiate the second governing equation (2.38) for the electric field and move some of the terms on the right hand side we obtain:

$$C^\top M(\mu)^{-1} C \frac{\partial e^n}{\partial \sigma} + \alpha M(\sigma) \frac{\partial e^n}{\partial \sigma} = \alpha \frac{\partial M(\sigma) e^{n-1, \text{fixed}}}{\partial \sigma} + \alpha M(\sigma) \frac{\partial e^{n-1}}{\partial \sigma} - \alpha \frac{\partial M(\sigma) e^{n, \text{fixed}}}{\partial \sigma} \quad (3.18)$$

The left side has the same matrix multiplication as the original equation (2.37), except that now we are solving for $\frac{\partial e^n}{\partial \sigma}$ and the right hand side is dependent only on σ , $\frac{\partial e^{n-1}}{\partial \sigma}$ and e^n . Therefore, to compute $\frac{\partial e^{i+1}}{\partial \sigma}$ we can just apply the same TDEM forward problem solver, but with a different right hand side. The sensitivity of magnetic flux data with respect to σ is then:

$$\frac{\partial d}{\partial \sigma} = Q C \frac{\partial e^{i+1}}{\partial \sigma}. \quad (3.19)$$

The adjoint product is solved recursively with backward time stepping.

The sensitivities of the potentials measured by DC resistivity method, $\frac{\partial \varphi}{\partial \sigma}$, follow the

same lines as the sensitivity of hydraulic head with respect to hydraulic conductivity in equation (3.9), since in both cases a Poisson type of equation is discretized. Again, only matrix-vector products are calculated.

Chapter 4

Coupled inverse problem

The idea of jointly evaluating different data goes back as far as 1975, when Vozoff and Jupp [97] jointly inverted two different kinds of geophysical measurements (DC resistivity and magnetotelluric data) by considering a simple three layer model. Inverting jointly hydrological and geophysical data has much more recent history, first studies were published about a decade ago and focused on unsaturated zone, as for example in [59], where the authors tested the joint inversion approach on two synthetic examples, combining GPR data with water saturation data. There are two main reasons for a relatively recent history of joint hydrogeophysical inversion. First, while in geophysics often both types of data relate to the same physical property, in hydrogeophysics this is usually not the case and a relationship between the groundwater and geophysical variable of interest has to be established. This gives ample space to create a framework for coupling geophysical and groundwater data, but the particular coupling can also be potentially the main source of error when jointly inverting these two datasets. Second, the groundwater and geophysical data are usually collected and analysed by two different research communities, with limited communication in between. Here, we bridge this gap by implementing both models within one computational framework. First, in section 4.1, we describe different approaches to couple the groundwater and geophysical variables, in section 4.2 we formulate the coupled inverse problem, and finally in the sections 4.3 and 4.4 we show different approaches to solve the coupled inverse problem.

4.1 Coupling the GW and geophysical variables

The necessary condition to proceed with any coupled inversion is that both the geophysical and groundwater data, directly or indirectly, relate to the same physical property, whether it is fluid conductivity, porosity, fluid saturation etc. The actual relation is then commonly defined by some empirical petrophysical relationships that couples the geophysical and hydrological states or parameters, for example electrical conductivity with solute content or seismic velocity with porosity, fluid conductivity or geological facies location. Such petrophysical relationships have to be either calibrated in the field or can be estimated from the laboratory analysis.

An alternative to a petrophysical relationship is applying a structural constraint in the minimization that has a preference for structure similarity between the two models, however, the two models do not need to coincide. The consistency between the models ideally results from the data and not from the assumed petrophysical relations.

In the next two sections we therefore discuss both approaches to couple the geophysical and groundwater variables; petrophysical relationships and structure similarity. Both of these options are later applied in our synthetic examples.

4.1.1 Petrophysical relationships

Petrophysical relationships represent the simplest and probably the most common way to couple the two different models. Widely used Archie's law was introduced already in 1942 [3] and provides a link between electrical conductivity, σ_b , and fluid conductivity σ_w . Another example of petrophysical relationship is the link between the hydraulic conductivity and charge density when measuring the self-potentials [50]. In saturated porous media the fluid has usually the major effect on the overall soil bulk electrical conductivity. At the same time, the fluid conductivity is often directly related to the amount of solutes in groundwater, which is our quantity of interest. Therefore, in the context of this work, the Archie's law relating fluid and soil bulk conductivity is the most relevant petrophysical relationship and is the subject of the next paragraph.

Coupling the salt mass fraction and electrical conductivity

The soil bulk electrical conductivity of a porous media is dependent on fluid conductivity, rock/soil porosity, permeability, saturation, temperature and also mineral composition [56]. In the saturated sediments of coastal aquifers, soil bulk conductivity is usually mainly

affected by the fluid (groundwater) salinity, though if the groundwater composition does not change then surface conductivity of fluid-grain interfaces, porosity or amount of saturation can be the main factors influencing the overall soil bulk conductivity. For fully saturated sediments the Archie's law can be written as:

$$\sigma_b = \frac{1}{\alpha} \sigma_w \phi^n, \quad (4.1)$$

where σ_b is the bulk electrical conductivity, σ_w is the fluid electrical conductivity and ϕ porosity. α and n are empirical parameters related to a geological material, which can be calibrated based on soil core samples, a field survey or recommended values from geological characterization. In this form of Archie's law the surface conductivity is neglected, which is a valid assumption for most of clay free sand and gravel aquifers, however, not for environments with a high clay content [56]. In many cases though, the differences in conductivity due to the variation in geological material are negligible compared to the increase in conductivity due to solute dynamic in groundwater.

The fluid conductivity in natural waters increases with the amount of dissolved solids and ions [42]. Linear relationships can be found for a fixed temperature between total dissolved solids (TDS) and fluid electrical conductivity. For example the seawater is usually dominated by sodium chloride ions and we can assume a linear relationship between salt mass fraction and fluid conductivity as

$$\sigma_w = b \omega + \sigma_F, \quad (4.2)$$

where σ_F is conductivity of freshwater, b is a constant and ω is salt mass fraction. The electrical conductivity of seawater is approximately two orders of magnitude higher than that of freshwater. After substituting into Archie's law, we have

$$\sigma_b = \frac{1}{\alpha} (b\omega + \sigma_F) \phi^n. \quad (4.3)$$

In this petrophysical relationship one assumes that the bulk conductivity is affected only by the electrical conductivity of the fluid in the porous matrix, the variations in temperature are small, and that the surface conductivity of porous material is negligible.

Equation (4.3) is used to generate electrical conductivity models based on the salt mass fraction from groundwater model simulations in the synthetic examples in section 5.1. For field applications it is more common to record the fluid conductivity σ_w of groundwater

samples, and only later by using a linear relationship to transform it to an actual solute mass fraction or concentration. However, this linear relationship is different from the general petrophysical relationship, having a different error and lower uncertainty. Therefore, in this work, we prefer to relate the solute fraction (or concentration) and soil bulk conductivity.

4.1.2 Structure-based coupling

As it has been pointed out in [70], most petrophysical relationships were originally defined for a scale of a representative elementary volume and therefore it is generally hard to determine and properly parametrize them for the field conditions. Another caveat of applying the petrophysical relations is the assumption that the properties such as porosity or saturation are homogeneous or known, a fixed parameter setting is then unlikely to be valid over the entire domain in environments with different geological units.

To avoid applying the petrophysical relationship one can assume instead that the two models have a common interface, or lithological units [70]; however, for such an assumption we need to have a good a-priori knowledge about the geology of the area, which may not be readily available, especially if we are about to model the processes in 3D. Application of this approach can be found in [13]. Another way to alleviate the need of explicit petrophysical link is by assuming a strong correlation between the groundwater and geophysical variables [54].

A more robust structure similarity measure seems like a good alternative to imposing a strict dependence by a petrophysical link, assuming a correlation or defining a-priori some fixed geological model. We consider two models m_1 and m_2 to have a similar structure if they change in the same locations (their transition zones coincide) [38]. The sign of change does not need to be the same; however, for the models of soil bulk electrical conductivity and solute content this is the case. The review paper of [35] provides different examples of applying the structure similarity measures in multiphysics geophysical imaging, where most of them involve computation of spatial gradients of the two different models (variables). The gradients can be normalized as in [27], serve to detect edge locations [39] via some model curvature function or become an input for a cross-gradient function or joint total variation.

The edge detection idea [39] lies in defining a polynomial with some threshold τ_1, τ_2 :

$$S(m) = \begin{cases} 0 & \text{if } |\nabla^2 m| < \tau_1 \\ P_5(|\nabla^2 m|) & \tau_1 \leq |\nabla^2 m| \leq \tau_2 \\ 1 & \text{if } \tau_2 \leq |\nabla^2 m| \end{cases} \quad (4.4)$$

This give smooth operator $S(m)$, fifth degree polynomial, which is also twice differentiable and thus convenient for Gauss-Newton type of minimization.

Joint total variation (JTV) of the two gradient fields is becoming popular in multimodal geophysical inversion and is based on the idea of sparse signal joint recovery. It encourages the two gradients to occur at the same location. For multiple geophysical data it has been applied in [38] or [28], though the idea originates in processing of the color images [10, 88]. For two models m_1 and m_2 it is

$$\Phi_{JTV}(m_1, m_2) = \int \sqrt{|\nabla m_1|^2 + |\nabla m_2|^2} dx,$$

where m_1 and m_2 represent the two, possibly different, models with a similar structure.

Computing the cross-gradient field product (CGP) is another convenient option to evaluate structure similarity between two models:

$$\Phi_{CGP}(m_1, m_2) = \int |\nabla m_1 \times \nabla m_2|^2 dx.$$

In geophysics it was introduced by [33] to jointly invert seismic and DC resistivity data and in [65] it was first applied for hydrological and geophysical data inversion.

Both JTV and CGP similarity measures can be differentiated with respect to both models and JTV is also convex. One thing to note is that if one of the models is flat, (i.e. having a single value everywhere) then its gradient field is equal to zero. The Φ_{JTV} then changes to standard total variation regularization operator for the other model, but in case of Φ_{CGP} the overall similarity term goes to zero.

This is important to keep in mind when evaluating the coupled objective function. If the gradient $|\nabla m_1| \approx 0$, the other model m_2 will not be penalized for any variations as ϕ_{CGP} goes to zero. Additional L_2 smooth regularization can reduce these variations but will be in conflict with creating a “structure”. Therefore, in [38] it was proposed to add

another term in ϕ_{CGP} to stabilize the problem in areas where $|\nabla m_1| \approx 0$, which is

$$\int |\nabla m_2| \chi_\theta (|\nabla m_1|) dx, \quad \text{where } \chi_\theta(t) = \frac{1}{2} (\tanh(\theta t) + 1). \quad (4.5)$$

The parameter θ is chosen so that the value of $\theta |\nabla m_1|$ is large enough, where we consider ∇m_1 to be significant.

In this work we tested Cross Gradient product and Joint Total variation as structure similarity measures. Both of them are easy to implement and can be also differentiated.

4.1.3 Discretization of the coupling terms

Lets start with the petrophysical relationship, which as a part of the objective function will change to

$$\Phi_{PR} = \|\sigma(\omega) - \sigma\|^2, \quad (4.6)$$

in other words we will minimize the norm of the difference between the soil bulk conductivity, and the soil bulk conductivity given by the solute mass fraction. We need to differentiate it with respect to both models and thus obtain the gradients with respect to σ and ω . These sensitivities can be easily derived as:

$$\nabla_\sigma \Phi_{PR} = -(\sigma(\omega) - \sigma), \quad \nabla_\omega \Phi_{PR} = \frac{\partial \sigma(\omega)}{\partial \omega} (\sigma(\omega) - \sigma) = \frac{b}{\alpha} \phi^m (\sigma(\omega) - \sigma). \quad (4.7)$$

And the second derivatives are as follows

$$\nabla_\sigma^2 \Phi_{PR} = -\mathbf{I}, \quad \nabla_\omega^2 \Phi_{PR} = \left(\frac{b}{\alpha} \phi^m\right)^2 \mathbf{I}, \quad (4.8)$$

with \mathbf{I} being the identity matrix.

The discretization of the JTV term is quite straightforward as well, we just need to keep in mind that the gradient fields occur at the cell faces and need to be averaged back on the cell centers values. Let Grad be the gradient operator and \mathbf{A}_f averaging matrix operator (from cell faces onto cell centers), the discretized JTV for the two models m_1 and m_2 is then:

$$\begin{aligned} \Phi_{JTV}(m_1, m_2) &= v^T \sqrt{\mathbf{M}}, \\ \text{where } \mathbf{M} &= \mathbf{A}_f \left((\text{Grad } m_1)^2 + (\text{Grad } m_2)^2 \right) \end{aligned} \quad (4.9)$$

and v is a vector corresponding to the cell sizes of the domain and sums up the term under the square root.

We can twice differentiate Φ_{JTV} with respect to m_1 and m_2 , which is necessary to solve the inverse problem by Gauss-Newton method. The gradient w.r.t. m_1 is:

$$\nabla_{m_1} \Phi_{JTV} = \text{Grad}^T \text{diag}(\text{Grad } m_1) A_f^T M^{-\frac{1}{2}} \quad (4.10)$$

and the Hessian is:

$$\begin{aligned} \nabla_{m_1}^2 \Phi_{JTV} = & \text{Grad}^T \text{diag}(A_f^T M^{-\frac{1}{2}}) \text{Grad} \\ & - \text{Grad}^T \text{diag}(\text{Grad } m_1) A_f^T M^{-\frac{3}{2}} A_f \text{diag}(\text{Grad } m_1) \text{Grad} \end{aligned} \quad (4.11)$$

For practical calculations the first term in (4.11) is semi-positive definite and therefore a good approximation to Hessian.

We could also directly discretize the cross-gradient field product (CGP), but that is generally numerically unstable due to the long differences that are needed to discretize the cross product. Therefore, we avoid the direct discretization of the cross product, and use the Lagrange's identity in a vector form instead and write ϕ_{CGP} as:

$$\phi_{CGP}(m_1, m_2) = \int |\nabla m_1 \times \nabla m_2|^2 dx = \int (|\nabla m_1|^2 |\nabla m_2|^2 - |(\nabla m_1)^T \nabla m_2|^2) dx. \quad (4.12)$$

In this case only dot products are used, derivatives along the same directions are multiplied and Φ_{CGP} term can be then discretized as

$$\begin{aligned} \Phi_{CGP}(m_1, m_2) = & \\ & \frac{1}{2} v^T \left(A_f (\text{Grad } m_1)^2 \odot A_f (\text{Grad } m_2)^2 - (A_f (\text{Grad } m_1) \odot A_f (\text{Grad } m_2))^2 \right), \end{aligned} \quad (4.13)$$

where again v is a vector corresponding to the cell sizes of the domain and A_f is averaging matrix operator (from cell faces onto cell centers).

Following the equation (4.13), the gradient w.r.t. m_1 for cross-gradient field product is

$$\begin{aligned} \nabla_{m_1} \Phi_{CGP} = & v^T \text{diag}(A_f \text{Grad } m_2) A_f \text{diag}(\text{Grad } m_1) \text{Grad} \\ & - v^T \text{diag}(A_f (\text{Grad } m_1) \odot (\text{Grad } m_2)) A_f \text{diag}(\text{Grad } m_1) \text{Grad}, \end{aligned} \quad (4.14)$$

and the Hessian is

$$\begin{aligned} \nabla_{\mathbf{m}_1}^2 \Phi_{CGP} = & \text{Grad}^T \text{diag} (A_f \text{Grad } \mathbf{m}_2) A_f^T \text{diag} (v) \text{Grad} \\ & - \text{Grad}^T \text{diag} \left((\text{Grad } \mathbf{m}_2) A_f^T \text{diag} (v) \text{diag} (\text{Grad } \mathbf{m}_2) \right) A_f \text{diag} (\text{Grad } \mathbf{m}_2) \text{Grad}. \end{aligned} \quad (4.15)$$

Both terms were implemented in our inversion code for the Hessian calculation.

4.2 Formulation of the coupled problem

Up to now we have described how to discretize and solve both groundwater and geophysical forward models, how to solve a single inverse problem including necessary regularization and also two different options for coupling the groundwater and geophysical variables. We are thus in a good shape to proceed to a coupled problem and solve it with a joint approach.

To keep the discussion general, we can assume that we are interested in some GW state or parameter (model) \mathbf{m} which can represent the hydraulic conductivity K or initial conditions for solute content (or also external fluxes, dispersion or other parameters). The groundwater data are dependent on model \mathbf{m} , with $s(\cdot)$ representing some hydrological state (solute concentration or hydraulic head). The geophysical model to be estimated is the soil bulk electrical conductivity, σ , that is affected mainly by the fluid conductivity and therefore is expected to have a similar structure as groundwater solute distribution.

Assume now that we have obtained both types of data at a single time, that is we have

$$\mathbf{d}_e = \mathbf{Q}_e u(\boldsymbol{\sigma}) + \boldsymbol{\epsilon}_e \quad (4.16)$$

$$\mathbf{d}_f = \mathbf{Q}_f s(\mathbf{m}) + \boldsymbol{\epsilon}_f \quad (4.17)$$

where \mathbf{Q}_e and \mathbf{Q}_f are sparse matrices that project the geophysical states, $u(\boldsymbol{\sigma})$, and the hydrological states, $s(\mathbf{m})$, onto their measurement locations, respectively. Let $\boldsymbol{\epsilon}_e$ and $\boldsymbol{\epsilon}_f$ be vectors with the errors associated with each measurement, which are assumed to be Gaussian, independent and identically distributed with covariance matrices $\boldsymbol{\Sigma}_e$ and $\boldsymbol{\Sigma}_f$.

We now develop a procedure to estimate the groundwater model \mathbf{m} and the electrical conductivity $\boldsymbol{\sigma}$ by the regularized maximum likelihood estimate [30, 37, 67]. This leads to

the following constrained optimization problem

$$\min_{\boldsymbol{\sigma}, \mathbf{m}} \frac{1}{2} \|\mathbf{d}_e - \mathbf{Q}_e u(\boldsymbol{\sigma})\|_{\boldsymbol{\Sigma}_e^{-1}}^2 + \alpha_e R(\boldsymbol{\sigma}) + \delta \frac{1}{2} \|\mathbf{d}_f - \mathbf{Q}_f s(\mathbf{m})\|_{\boldsymbol{\Sigma}_f^{-1}}^2 + \alpha_f R(\mathbf{m}) \quad (4.18)$$

$$\text{s.t.} \quad \Phi_S(s(\mathbf{m}), \boldsymbol{\sigma}) \leq \tau \quad (4.19)$$

Here R is the regularization operator (discussed in section 3.4) and α_e, α_f and δ are regularization parameters. δ specifically weights the contributions of two different data misfits. The constraint (4.19) here represents either petrophysical relationship (Archie's law) or some structure similarity constraint between hydrological state $s(\mathbf{m})$ and soil bulk conductivity $\boldsymbol{\sigma}$. The choice of τ , representing the error bound for the similarity constraint, depends on the particular similarity coupling, if it is set to zero, we impose an exact similarity between groundwater and geophysical model. In the next few sections we will discuss possible ways of minimizing this functional.

4.3 Minimization with an explicit petrophysical constraint

Lets first assume we do know the explicit petrophysical relationship between the two models,

$$\boldsymbol{\sigma} = \eta s(\mathbf{m}) + \boldsymbol{\sigma}_{fb} = p(\mathbf{m}), \quad (4.20)$$

which is based on the Archie's law introduced in the equation (4.3), and therefore $s(\mathbf{m})$ refers here to solute mass fraction. We lumped a few parameters into $\eta = \frac{c}{\alpha} \phi^n$, and $\boldsymbol{\sigma}_{fb}$ corresponds to the conductivity of porous media with freshwater only (or without any solute) and is equal to $\boldsymbol{\sigma}_{fb} = \frac{1}{\alpha} \phi^n \sigma_F$. To recall, the objective function for the coupled inverse problem (equation (4.18)) is then:

$$\min_{\boldsymbol{\sigma}, \mathbf{m}} \frac{1}{2} \|\mathbf{d}_e - \mathbf{Q}_e u(\boldsymbol{\sigma})\|_{\boldsymbol{\Sigma}_e^{-1}}^2 + \alpha_e R(\boldsymbol{\sigma}) + \delta \frac{1}{2} \|\mathbf{d}_f - \mathbf{Q}_f s(\mathbf{m})\|_{\boldsymbol{\Sigma}_f^{-1}}^2 + \alpha_f R(\mathbf{m}) \quad (4.21)$$

$$\text{s.t.} \quad \boldsymbol{\sigma} - p(\mathbf{m}) = 0 \quad (4.22)$$

A number of different approaches may be taken to solve the optimization problem above. One possibility is a direct substitution of $p(\mathbf{m})$ for $\boldsymbol{\sigma}$ and work with \mathbf{m} alone. In such case we solve the problem with an exact constraint and the objective function (where we omit

the extra regularization term for $\boldsymbol{\sigma}$) is

$$\Phi(\mathbf{m}) = \delta_e \frac{1}{2} \|\mathbf{d}_e - \mathbf{Q}_e u(p(\mathbf{m}))\|_{\boldsymbol{\Sigma}_e^{-1}}^2 + \delta_f \frac{1}{2} \|\mathbf{d}_f - \mathbf{Q}_f s(\mathbf{m})\|_{\boldsymbol{\Sigma}_f^{-1}}^2 + R(\mathbf{m}). \quad (4.23)$$

This approach has the advantage of solving a smaller problem, however, it complicates other aspects of the inversion. First, we are required to choose two weights, δ_e and δ_f , for the data misfits with respect to regularization term at each iteration. Despite abundant research on choosing one regularization parameter, there are almost no criteria for setting two parameters during the iterative minimization process when each data misfit has a different speed of convergence. A more detailed discussion can be found in [17], where the authors used magnetotelluric data together with controlled source EM data. Even though both data sets can be modeled by changes in conductivity, non-trivial weighting was needed in order to jointly invert them. Second, the multiplication of Jacobians and data misfit can have a very different computational cost for each data misfit, which can make each iteration very unbalanced and does not favor parallelization. Finally, if the relationships between $\boldsymbol{\sigma}$ and $p(\mathbf{m})$ are inexact, forcing them may lead to inversion artifacts. Therefore, rather than solving the problem “all at once” we decided to apply the alternating direction method of multipliers (ADMM) to minimize this coupled objective function.

4.3.1 ADMM

The main advantage of ADMM is that the groundwater and geophysical parts can be solved separately, that is, we do not need to weight the two different data misfits in one objective function, but instead we split the minimization into two subproblems. This enables us to use existing inversion methodologies and even software packages only with minor changes. It also takes the advantage of the existing parallelization for an inversion of a single model (discussed in the previous chapter) and therefore substantially increase the efficiency when solving large scale problems. Furthermore, since the petrophysics is enforced as a constraint, it is not applied exactly throughout the path of optimization which yields additional degrees of freedom to the optimization algorithm.

Following the ADMM approach, the augmented Lagrangian for (4.21) is

$$\begin{aligned} \mathcal{L}(\boldsymbol{\sigma}, \mathbf{m}, \mathbf{y}) = & \frac{1}{2} \|\mathbf{d}_e - \mathbf{Q}_e u(\boldsymbol{\sigma})\|_{\boldsymbol{\Sigma}_e^{-1}}^2 + \alpha_e R(\boldsymbol{\sigma}) + \frac{1}{2} \|\mathbf{d}_f - \mathbf{Q}_f s(\mathbf{m})\|_{\boldsymbol{\Sigma}_f^{-1}}^2 + \alpha_f R(\mathbf{m}) \\ & + \mathbf{y}^\top (\boldsymbol{\sigma} - p(\mathbf{m})) + \frac{\rho}{2} \|\boldsymbol{\sigma} - p(\mathbf{m})\|^2 \end{aligned} \quad (4.24)$$

Here \mathbf{y} is a Lagrange multiplier and ρ is a parameter that can be chosen somewhat arbitrarily. The k^{th} iteration of ADMM is summarized in Algorithm 2.

Algorithm 2 ADMM

- Approximately minimize the augmented Lagrangian with respect to $\boldsymbol{\sigma}$.
 - Approximately minimize the augmented Lagrangian with respect to \mathbf{m} .
 - Update the Lagrange multiplier $\mathbf{y}^{k+1} = \mathbf{y}^k + \rho(\boldsymbol{\sigma}^{k+1} - p(\mathbf{m}^{k+1}))$.
-

We now discuss the solution of each subproblem and show that by using small modifications to existing inversion codes, the ADMM iteration can be carried out efficiently.

Geophysical imaging block descent

At each step of minimizing the augmented Lagrangian with respect to $\boldsymbol{\sigma}$, we approximately solve:

$$\min_{\boldsymbol{\sigma}} \Phi(\boldsymbol{\sigma}) = \frac{1}{2} \|\mathbf{d}_e - \mathbf{Q}_e \mathbf{u}(\boldsymbol{\sigma})\|_{\Sigma_e^{-1}}^2 + \alpha_e \mathbf{R}(\boldsymbol{\sigma}) + \mathbf{y}^\top (\boldsymbol{\sigma} - p(\mathbf{m})) + \frac{\rho}{2} \|\boldsymbol{\sigma} - p(\mathbf{m})\|^2 \quad (4.25)$$

The objective function consists of a data misfit and a regularization part, as in usual inverse problems, and coupling terms involving also \mathbf{m} , the groundwater variable. We can proceed using the Gauss-Newton method to minimize (4.25) with respect to $\boldsymbol{\sigma}$. Compared to a standard inverse problem, we need to know also the derivatives of the coupling terms with respect to $\boldsymbol{\sigma}$, however, these are, in this case, straightforward since \mathbf{m} is fixed and were already derived in section 4.1.3.

If we set $\mathbf{J}_e = \frac{\partial \mathbf{u}(\boldsymbol{\sigma})}{\partial \boldsymbol{\sigma}}$ and assume for simplicity that $\Sigma_e = \mathbf{I}$, the derivative $\frac{\partial \Phi}{\partial \boldsymbol{\sigma}}$ is

$$\frac{\partial \Phi}{\partial \boldsymbol{\sigma}} = \mathbf{J}_e^T \mathbf{Q}_e^T (\mathbf{Q}_e \mathbf{u}(\boldsymbol{\sigma}) - \mathbf{d}_e) + \alpha_e \mathbf{L}^T \mathbf{L} (\boldsymbol{\sigma} - \boldsymbol{\sigma}_{ref}) + \mathbf{y} + \rho (\boldsymbol{\sigma} - p(\boldsymbol{\omega})) = 0 \quad (4.26)$$

and the search direction at each time step is

$$\Delta \boldsymbol{\sigma} = - (\mathbf{J}_e^T \mathbf{Q}_e^T \mathbf{Q}_e \mathbf{J}_e + \alpha_e \mathbf{L}^T \mathbf{L} + \rho \mathbf{I})^{-1} \frac{\partial \Phi}{\partial \boldsymbol{\sigma}}. \quad (4.27)$$

The model is then updated by a “soft” Armijo line search [75], $\boldsymbol{\sigma}^{k+1} = \boldsymbol{\sigma}^k + \mu \Delta \boldsymbol{\sigma}$, similarly as for a standard inverse problem described in section 3.2. The parameter μ is adjusted to ensure sufficient decrease of Φ , where k refers to k^{th} iteration of the geophysical descent. We take a small fixed number of Gauss-Newton steps, and as has been already mentioned in 3.4,

we do not search directly for the electrical conductivity σ model \mathbf{m} , where $\sigma = 1 - \tanh(\mathbf{m})$.

Groundwater model block descent

Similarly, the objective function for the augmented Lagrangian with respect to groundwater model \mathbf{m} , can be written as:

$$\min_{\mathbf{m}} \Phi(\mathbf{m}) = \frac{1}{2} \|\mathbf{d}_f - \mathbf{Q}_f s(\mathbf{m})\|_{\Sigma_f^{-1}}^2 + \alpha_f \mathbf{R}(\mathbf{m}) + \mathbf{y}^\top (\boldsymbol{\sigma} - p(\mathbf{m})) + \frac{\rho}{2} \|\boldsymbol{\sigma} - p(\mathbf{m})\|^2 \quad (4.28)$$

Now the geophysical variable $\boldsymbol{\sigma}$ is fixed and the derivatives of the coupling terms with respect to \mathbf{m} involve the sensitivity $\mathbf{J}_f = \frac{\partial s(\mathbf{m})}{\partial \mathbf{m}}$, which were derived in section 3.3.

Again, we assume a quadratic regularization for \mathbf{m} , which gives the gradient of $\Phi(\mathbf{m})$ as

$$\frac{\partial \Phi}{\partial \mathbf{m}} = \mathbf{J}_f^\top \mathbf{Q}_f^\top (\mathbf{d}_f - \mathbf{Q}_f s(\mathbf{m})) + \alpha_f \mathbf{L}^\top \mathbf{L} (\mathbf{m} - \mathbf{m}_{ref}) - \eta \mathbf{J}_f^\top \mathbf{y} + \rho \eta \mathbf{J}_f^\top (\boldsymbol{\sigma} - p(\mathbf{m})) = 0. \quad (4.29)$$

The groundwater model minimization follows the same Gauss-Newton approach as has been described above for geophysical imaging.

ADMM stopping criteria

The ADMM algorithm is stopped when the norm of the residual r_k , i.e. the constraint given by the petrophysical relationship $r_k = \boldsymbol{\sigma} - p(\mathbf{m})$, is sufficiently small or the changes in $\|r_k\|$ between the last few iterations are below some threshold value. At this point, we have the capability of fitting both the geophysical and groundwater data such that the geophysical and groundwater model agree.

It has been shown that ADMM has a linear rate of convergence¹, where for some applications the desired precision can be reached in a relatively small amount of steps/descents [11]. The penalty term ρ has an effect on the speed of convergence [23, 36]; however, under mild conditions any positive value of ρ will lead to convergence [36], both in terms of the residual $r_k \rightarrow 0$ and finding an optimal solution for both models. In our study we set up ρ by a trial and error procedure, where $\rho \in [0.1, 1]$ provided similar results. In some cases better rate of convergence can be achieved by so called Over-relaxed ADMM, or by adding

¹Note that Gauss-Newton has a linear rate of convergence as well although the constant in Gauss-Newton may be better than the ADMM constant.

a scaling parameter for the Lagrangian multiplier, the work of [74] provides actual rate bounds based on the parameter choices.

4.4 Minimization without an explicit petrophysical constraint

As we already elaborated on in section 4.1.2, the petrophysical relationship used in ADMM minimization is often not known a-priori, its parametrization is uncertain or has to be calibrated. If we instead apply some structure similarity measure Φ_S , we can again change the constrained formulation of the coupled objective function in Eq.(4.18) to the unconstrained one and obtain:

$$\begin{aligned} \min \Phi(\mathbf{m}, \boldsymbol{\sigma}) = & \frac{1}{2} \|\mathbf{Q}_e u(\boldsymbol{\sigma}) - d_e\|_{\boldsymbol{\Sigma}_e^{-1}}^2 + \alpha_e \|\mathbf{L}_e(\boldsymbol{\sigma} - \boldsymbol{\sigma}_{ref})\| + \\ & \delta \frac{1}{2} \|\mathbf{Q}_f s(\mathbf{m}) - d_f\|_{\boldsymbol{\Sigma}_f^{-1}}^2 + \alpha_f \|\mathbf{L}_g(\mathbf{m} - \mathbf{m}_{ref})\| + \beta \Phi_S(s(\mathbf{m}), \boldsymbol{\sigma}) \end{aligned} \quad (4.30)$$

We can apply a Gauss - Newton method and minimize $\Phi(\mathbf{m}, \boldsymbol{\sigma})$ simultaneously for both models, the soil bulk conductivity $\boldsymbol{\sigma}$ and groundwater model \mathbf{m} . However, care has to be taken with regard to a different convergence speed and data misfit magnitudes of the groundwater and geophysical models. An alternative is to apply a Block Coordinate Descent Method (BCDM), which, similarly as ADMM, splits the coupled objective function into two subproblems, and treats each separately with a Gauss-Newton method.

4.4.1 BCDM

Block Coordinate Descent method minimizes each subproblem with respect to one of the models and hence we do not need to readjust weights during minimization to accommodate the different speed of convergence of the two models. Additionally, both inversion codes are altered only by adding the similarity term to the original inversion for a single type of data. The drawback of the block descent is slower convergence (linear) towards the optimal solution. This method is sometimes referred to as a Block Gauss-Seidel method. The algorithm is as follows:

Following the Eq.(4.30), letting the Jacobians $\mathbf{J}_e = \frac{\partial u(\boldsymbol{\sigma})}{\partial \boldsymbol{\sigma}}$ and $\mathbf{J}_f = \frac{\partial s(\mathbf{m})}{\partial \mathbf{m}}$, and for simple notation consider the measurement error matrices $\boldsymbol{\Sigma}_e^{-1}$ and $\boldsymbol{\Sigma}_f^{-1}$ to be unity, the GW and geophysical descents can be summarized as

Algorithm 3 BCDM

Approximately minimize Φ with respect to $\boldsymbol{\sigma}$
Approximately minimize Φ with respect to \mathbf{m}
Update $\boldsymbol{\sigma}, s(\mathbf{m})$, if $\Delta\mathbf{m} \leq \text{const.}$ terminate

DC descent step

$$\begin{aligned}\nabla_{\boldsymbol{\sigma}}\Phi &= \mathbf{J}_e^T \mathbf{Q}_e^T (\mathbf{Q}_e u(\boldsymbol{\sigma}) - d_e) + \alpha_e \mathbf{L}^T \mathbf{L} (\boldsymbol{\sigma} - \boldsymbol{\sigma}_{\text{ref}}) + \beta \nabla_{\boldsymbol{\sigma}} \Phi_S(s(\mathbf{m}), \boldsymbol{\sigma}) \\ \nabla_{\boldsymbol{\sigma}}^2 \Phi &= \mathbf{J}_e^T \mathbf{Q}_e^T \mathbf{Q}_e \mathbf{J}_e + \alpha_e \mathbf{L}^T \mathbf{L} + \beta \nabla^2 \Phi_S(s(\mathbf{m}), \boldsymbol{\sigma}) \\ \Delta\boldsymbol{\sigma} &= -(\nabla_{\boldsymbol{\sigma}}^2 \Phi^{-1}) \nabla_{\boldsymbol{\sigma}} \Phi \\ \boldsymbol{\sigma}^{k+1} &= \boldsymbol{\sigma}^k + \mu \Delta\boldsymbol{\sigma}\end{aligned}\tag{4.31}$$

GW descent step

$$\begin{aligned}\nabla_{\mathbf{m}}\Phi &= \mathbf{J}_f^T \mathbf{Q}_f^T (\mathbf{Q}_f s(\mathbf{m}) - d_f) + \alpha_f \mathbf{L}^T \mathbf{L} (\mathbf{m} - \mathbf{m}_{\text{ref}}) + \beta \mathbf{J}_f^T \nabla_{\mathbf{m}} \Phi_S(s(\mathbf{m}), \boldsymbol{\sigma}) \\ \nabla_{\mathbf{m}}^2 \Phi &= \mathbf{J}_f^T \mathbf{Q}_f^T \mathbf{Q}_f \mathbf{J}_f + \alpha_f \mathbf{L}^T \mathbf{L} + \beta \mathbf{J}_f^T \nabla^2 \Phi_S(s(\mathbf{m}), \boldsymbol{\sigma}) \mathbf{J}_f \\ \Delta\mathbf{m} &= -(\nabla_{\mathbf{m}}^2 \Phi^{-1}) \nabla_{\mathbf{m}} \Phi \\ \mathbf{m}^{k+1} &= \mathbf{m}^k + \mu \Delta\mathbf{m}\end{aligned}\tag{4.32}$$

We still need to assign the weights α and β to balance the contribution of regularization and similarity term. Weights α were set the same as for single data inversions and weights β were readjusted during the inversion process based on the data misfit Φ_d and Φ_S :

$$\beta = w \frac{\Phi_d}{\Phi_S} \quad \text{where } w \in [0, 1].\tag{4.33}$$

The parameter μ , determining the size of the update for a given direction, is searched via soft Armijo line search [75]. The convergence of BCDM where each block is not solved exactly has been a subject of [83], more about the general convergence and conditions for the sublinear rate can be found in [9].

BCDM can be also applied if we know the petrophysical relationship, in such case the similarity term Φ_S would be simply replaced by the petrophysical constraint. However, in such case, the ADMM is expected to converge faster towards optimal solution than BCDM, and would be thus the preferred method.

4.4.2 Joint Gauss-Newton method (JGN)

In the context of this work, by Joint Gauss-Newton method we refer here to solving the coupled problem jointly, updating both the groundwater and geophysical variable during each iteration. This means that all the terms of the objective function in Equation (4.30) are evaluated together. Hence compared to the BCDM discussed above, we keep both data misfit terms together in one objective function, i.e. no splitting to groundwater and geophysical subproblems occurs. The advantage of this approach is overall lesser number of iterations; however, we are now solving a larger system. Additionally, we need to determine all weights in equation (4.30) to balance the contribution of the different data misfits and the regularization and coupling terms.

At each Gauss-Newton step we then update the vector v that contains both conductivity σ and groundwater parameter \mathbf{m} , $v = (\mathbf{m}, \sigma)^\top$:

$$\begin{pmatrix} \Delta \mathbf{m} \\ \Delta \sigma \end{pmatrix} = - \begin{pmatrix} \nabla_{\sigma}^2 \Phi & \nabla_{\sigma} \nabla_{\mathbf{m}} \Phi \\ \nabla_{\mathbf{m}} \nabla_{\sigma} \Phi & \nabla_{\mathbf{m}}^2 \Phi \end{pmatrix}^{-1} \begin{pmatrix} \nabla_{\mathbf{m}} \Phi \\ \nabla_{\sigma} \Phi \end{pmatrix}. \quad (4.34)$$

The sensitivities with respect to \mathbf{m} and σ , which are in fact implemented as matrix times vector routines, are likely to have a different computational time; however, in this setup can not be solved in parallel. Therefore, despite the over all lower number of iterations the computational time for JGN might not be significantly better than for BCDM minimization.

The off-diagonal terms of the Hessian matrix are coming from the structure similarity term Φ_S only, since we do not have an explicit petrophysical relationship and need to be derived analytically.

$$\begin{aligned} \nabla_{\sigma} \nabla_{\mathbf{m}} \Phi &= \nabla_{\sigma} \left(\mathbf{J}_f^\top \mathbf{Q}_f^\top (\mathbf{Q}_f s(\mathbf{m}) - d_f) + \alpha_f \mathbf{L}^\top \mathbf{L} (\mathbf{m} - \mathbf{m}_{\text{ref}}) + \beta \mathbf{J}_f^\top \nabla_{\mathbf{m}} \Phi_S(s(\mathbf{m}), \sigma) \right) \\ &= \nabla_{\sigma} \left(\beta \mathbf{J}_f^\top \nabla_{\mathbf{m}} \Phi_S(s(\mathbf{m}), \sigma) \right) \\ \nabla_{\mathbf{m}} \nabla_{\sigma} \Phi &= \nabla_{\mathbf{m}} (\beta \nabla_{\sigma} \Phi_S(s(\mathbf{m}), \sigma)) \end{aligned} \quad (4.35)$$

Schemes for both of the methods are depicted in Figure 4.1.

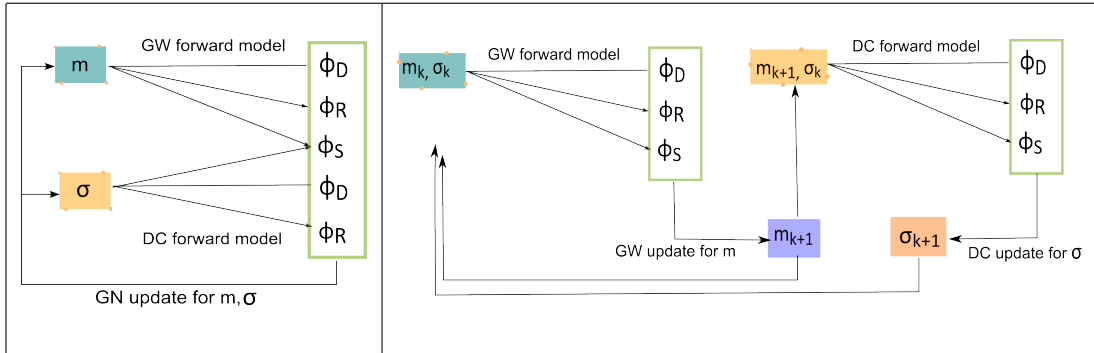


Figure 4.1: Comparison of the JGN and BCDM scheme. Left: The scheme for a single iteration of the Joint Gauss - Newton minimization, the two data misfit terms Φ_D , regularization terms Φ_R and a similarity term Φ_S are computed for the initial estimates of \mathbf{m} and $\boldsymbol{\sigma}$, both models are then updated via a Gauss-Newton iteration (Eq.(4.34)). Right: BCDM minimization starts with the Gauss-Newton descent for the groundwater model \mathbf{m} only (Eq.(4.32)) involving also the similarity term, the new GW model \mathbf{m}_{k+1} serves as an input for the geophysical Gauss-Newton descent (Eq.(4.31)), leading to an update for the geophysical model, $\boldsymbol{\sigma}_{k+1}$, the next BCDM iteration starts with \mathbf{m}_{k+1} and $\boldsymbol{\sigma}_{k+1}$.

Chapter 5

Applications - synthetic examples

5.1 Seawater intrusion - state estimation with ADMM

The first synthetic example follows a seawater intrusion scenario, where the variable density flow brings more complexity to groundwater modeling, but due to the increased conductivity of seawater it is also an ideal target for most of the electromagnetic methods. Therefore, both groundwater and geophysical data are often collected to monitor seawater intrusions.

Seawater intrusion (SWI) is a complex process that occurs naturally due to small differences in density between freshwater and saltwater. Depending on the hydrogeological setting, seawater can enter the coastal aquifers through preferential flow pathways far into the interior, or remain in a close proximity to the coast [4]. Increased groundwater extraction, reduced recharge into aquifers, and other human activities can cause the SWI to propagate further inland (Figure 5.1). To monitor the SWI and manage coastal aquifers, representative groundwater models need to be developed. Such models can then provide explanations for saltwater origin in the area, and can be used to validate different pumping scenarios to manage the saltwater front propagation and future freshwater demands ([29, 55, 61] or [87]).

Numerous research studies have been published regarding mapping the seawater intrusions progress by geophysical methods, especially large scale surveys are convenient for SWI delineation ([19, 31, 72, 93] or [68]). Due to the complex character or governing equations for seawater intrusion process, the groundwater and geophysical model usually stay separate in most of the studies. Hence, in the coupled approaches the information is exchanged only via some extra data or reference models.

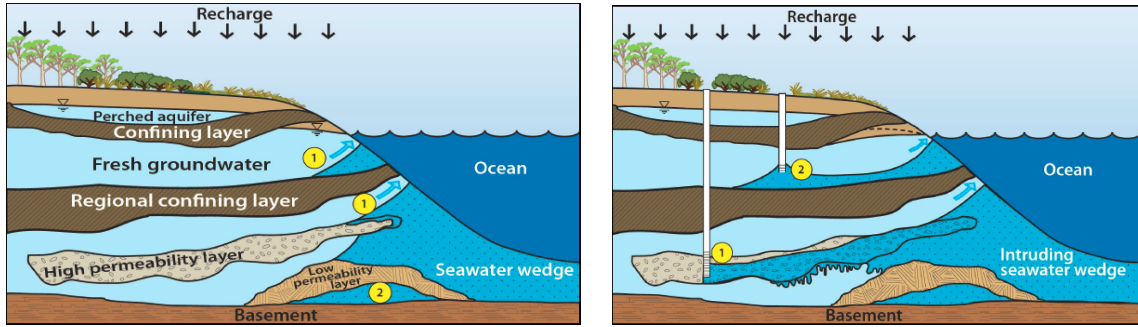


Figure 5.1: Effect of increased pumping on the propagation of the SWI front. Source: A.D. Wenner, P.E. Jacobsen, L.K. Morgan - Understanding seawater intrusions [poster]. 2013

For example, in the work of Herckenrath et al.[45], the geophysical estimates from 1D TDEM soundings served as extra observations for the GW model (after transforming via petrophysical relationship - Archie's law). In their coupled approach the GW model is used to interpret the data and guide the geophysical inversion. A different way of transforming the information from geophysical estimates was introduced in Beaujean et al.[8]. The ERT derived conductivities were transformed via Archie's law to salt mass fraction estimates. These estimates were then filtered using a cumulative sensitivity based on squared Jacobians and served as extra data for hydrological inversion next to groundwater salt mass fraction data. The inversion was performed with PEST using a gradient based method, and therefore it was not applicable to large scale problems.

In the following synthetic example, we solve the inverse problem by minimizing both types of data, and assume the knowledge of the petrophysical relationship, which provides the constraint in the minimization. We use groundwater and geophysical data (well salinity data and electrical potentials) collected only for a single instance in time, and we estimate the unknown current and initial solute distribution based on this data. Since in this case we assume to know the petrophysical relationship, we can apply ADMM method for the joint minimization. Besides, we also show results for the direct substitution approach discussed at the beginning of section 4.3.

The fact that we solve for the solute content-electrical conductivity only, with the assumption of at least an approximate knowledge of other GW parameters can be regarded as naive; however, the same framework can be established for GW parameters such as hydraulic permeability, external fluxes and other GW variables as long as appropriate

sensitivities are derived. We do not try here to estimate all of these parameters at once, since despite having two different sets of data, the inverse problem is essentially highly ill-posed, and most of these parameters vary over the entire domain. However, to test the robustness of the proposed minimization scheme we alter the “known” GW parameters used in the inversion such as hydraulic permeability and dispersion values, to see the effect on estimates.

First, in section 5.1.1 we introduce the two cases of seawater intrusion scenarios, both of them have a similar boundary conditions setup, but different permeability and thus lead to different SWI fronts. We also describe both groundwater and geophysical data survey designs. In section 5.1.2 we present the results of ADMM joint minimization and the errors of the salinity estimates for a specific groundwater data survey; besides, we run multiple inversions to see how the change of GW data locations affects the estimate errors. The results for altering the true GW parameters during the inversion are also presented in section 5.1.3. In the last section we discuss and summarize all findings from the quantitative and qualitative point of views.

5.1.1 Parametrization for the synthetic scenarios

We created two different model problems in 3D representing seawater intrusion; one with a homogeneous permeability field (Case 1) and one with heterogeneous permeability field (Case 2). The heterogeneous case is based on the field study at the Kidd2 site in the Fraser River Delta in Richmond, BC [71], where the delta slope deposits confine the sandy deltaic deposits and a seawater wedge enters from the river. In both cases the boundary conditions followed the Henry’s benchmark problem with hydrostatic pressure for the seaward boundary and freshwater inflow rate for the inland boundary. The actual parameter values are presented in the Table 5.6 including the external fluxes representing the pumping rates.

For the initial “unknown” solute mass fraction distribution at time t_0 we let the GW model run forward up to a certain time. During this simulation, a pumping well is placed in the southwest part of the area. Afterward, we altered the external fluxes, and a single pumping well was placed in the north-east area while the freshwater inflow flux was decreased. The GW simulation then ran from the initial state at t_0 up to time t_1 for 300 days, with a time step 15 days. The “true” initial and final solute distributions for both cases can be seen in Figure 5.3. The external fluxes are changed at time t_0 so that the GW

| GW model | Heterogeneous case | Homogeneous case |
|-------------------------------------|---|----------------------------------|
| Grid | 44x32x12 cells | 44x32x12 cells |
| Cell size | 1 x 1 x 1 m | 1 x 1 x 1 m |
| Permeability k | | |
| Silty sand | $k_x = 2 \times 10^{-12} m^2, k_y = 4.4 \times 10^{-11}, k_z = 2 \times 10^{-14} m^2$ | $k_x = 4.4 \times 10^{-11} m^2,$ |
| Fine and medium sand | $k_x = 4.4 \times 10^{-11} m^2, k_y = 4.4 \times 10^{-11}, k_z = 4.4 \times 10^{-12} m^2$ | $k_y = 2.4 \times 10^{-11},$ |
| Silty clay (Fig. 5.2) | $k_x = 10^{-14} m^2, k_y = 4.4 \times 10^{-11}, k_z = 10^{-17} m^2$ | $k_z = 1 \times 10^{-12} m^2$ |
| Porosity ϕ | 0.35 | 0.35 |
| Dispersion D | 0.0032 $m^2/year$ | 0.0032 $m^2/year$ |
| Viscosity | 0.001 | 0.001 |
| Freshwater density | 1000 kg/m^3 | 1000 kg/m^3 |
| Saltwater density | 1025 kg/m^3 | 1025 kg/m^3 |
| Q_{GW} , pumping rate up to t_0 | $[x,y] = [8,14], 0.16 d^{-1}$ | $[x,y] = [8,14], 0.16 d^{-1}$ |
| Q_{GW} , pumping rate up to t_1 | $[x,y] = [26,26], 0.13 d^{-1}y$ | $[x,y] = [26,32], 0.13 d^{-1}$ |

| Geophysical model | |
|---------------------|--------------------|
| Grid | 50 x 38 x 12 cells |
| Cell size | 1 to 4 m |
| Arhie's law m | 1.7 |
| Background σ | 0.0065 S/m |

Table 5.1: Parametrization for the seawater intrusion Cases 1 and 2.

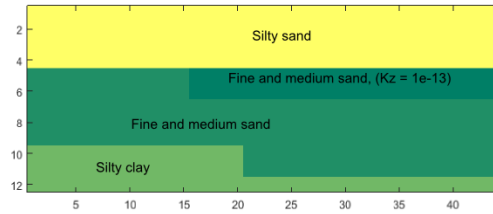


Figure 5.2: The geological layers for the heterogeneous case based on Kidd2 site in Fraser River delta [71], schema for k_z field.

model, used in the coupled inversion, could not simulate the initial solute content from a zero distribution. Moreover, changes to external fluxes (such as different pumping schemes or reduced discharge) are also likely to happen in real conditions.

We collect both types of data only at time t_1 . For the GW sampling we have two transects of wells (with spacing of 7 m) and 3 depth samples collected (depth = 4, 7 and 11 m) in Case 1, and two depth samples ($z = 5$ and 9 m) for the heterogeneous Case 2. The position of the transects was later altered to test different experimental designs, however, here we present in detail the case with west-east locations $x = 16$ m and $x = 24$ m, see in Figure 5.4. Gaussian random noise with standard deviation 0.05 was added to all measured solute fraction values. No hydraulic head or pressure data were used in the

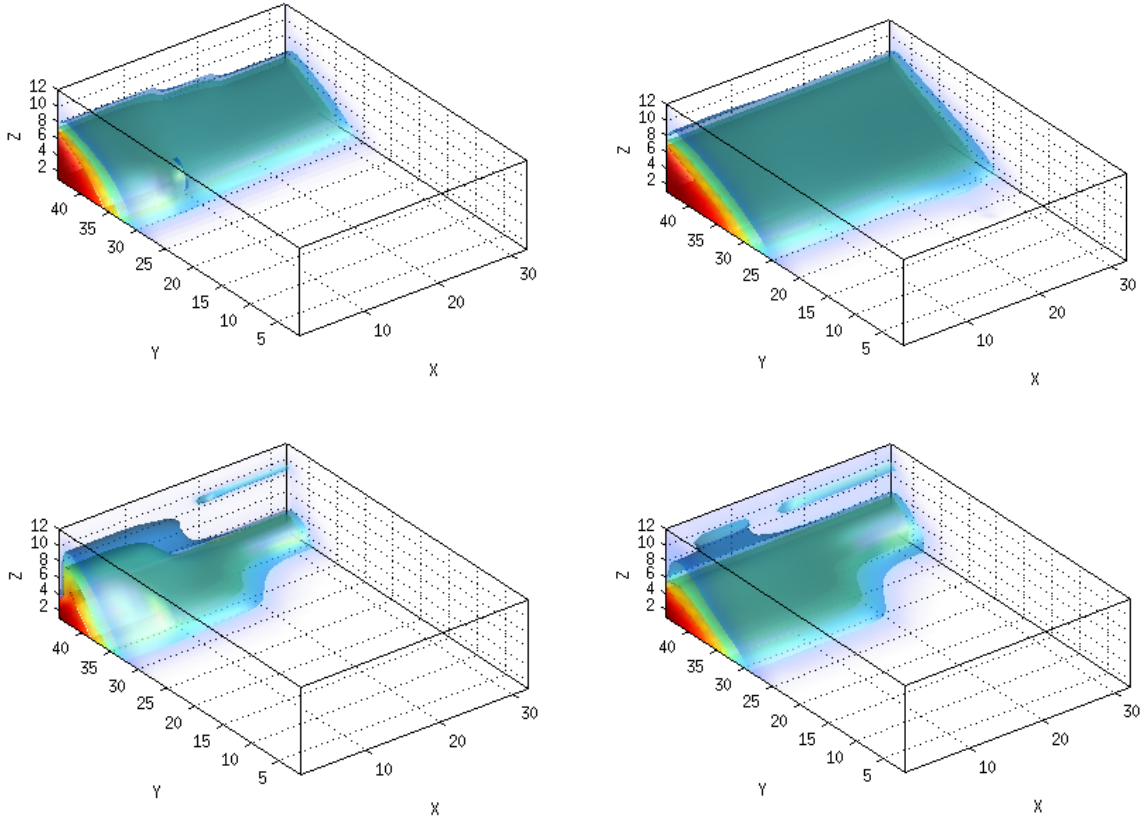


Figure 5.3: Seawater intrusion scenario: Upper left and right: True models for initial and final solute distribution for Case 1; Bottom left and right: True models for initial and final solute distribution for Case 2. Isosurfaces at $\omega = 0.25, 0.5$ and 0.75 are displayed.

coupled inversion.

For the geophysical data, the simulated solute fraction at time t_1 was converted through Archie's law into bulk electrical conductivity, and potentials were solved through the DC forward model described in Section 2.2.1. There are many different options for the electrode layout and measurement scheme; the following one was chosen based on the sensitivities of measured data, while trying to maximize the depth resolution for data collected only at the surface. The electrode layout corresponds to a regular grid with spacing 3m in x direction and 4m in y direction, giving in total 72 electrodes. A positive electrode was fixed close to the seaward boundary (west) and the negative charge was moving along the x profile,

towards east. For each source pair (72 in total) potential differences were measured on all receivers, where one of the receiver couples was always fixed and placed in the north west corner (see Figure 5.4). 3% Gaussian random noise was added to the measured potentials.

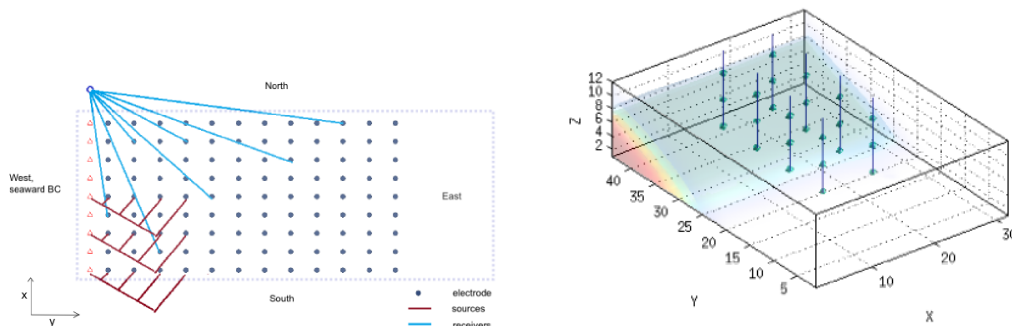


Figure 5.4: Data collection. Left: Experimental design for the DC survey: Dark blue points represent the electrodes on the surface placed on a regular grid, saltwater is coming in from the west boundary. Right: GW wells locations, 8 wells in total are placed along two transects at $x = 16$ m and $x = 24$ m distance, later labeled as b and c , other experimental designs for GW data are plotted in Figure 5.10.

5.1.2 Joint inversion with ADMM

The ADMM minimization starts with the GW model descent and continues as long as the constraint residual r_k decreases (or up to 5 runs of GW and geophysical descent). The residual r_k represents the difference between bulk electrical conductivity and electrical conductivity derived from the GW model via Archie's law. Since this is a synthetic example we can record the actual initial and final errors next to the data misfits for both the groundwater and geophysical data during the minimization. By actual error we mean the norm $\epsilon(\omega_k) = \|\omega_k - \omega_{true}\|$. Due to the ADMM approach we do not need to weight the two different data misfits, however, weights still need to be assigned for the regularization term α and the so called penalty term, ρ (see the augmented Lagrangian formulation in (4.24)). The choice of the regularization parameter α has already been largely discussed in the literature (see [41, 94] and reference within), and can be determined either based on initial values for ϕ_D, ϕ_S and ϕ_R , or by a trial and error procedure. The choice of the penalty parameter ρ was discussed in the section 4.3.1. A particular set of weights were applied to obtain all results presented here in; $\alpha_e = 10^{-3}$, $\alpha_f = 5 \times 10^{-3}$ and $\rho = 0.4$.

The number of Gauss-Newton iterations (within each ADMM descent) was 3-4 for the GW block descent, and between 6 to 10 for the geophysical block descent.

In the Figure 5.5, the actual errors scaled against the error of initial estimates are plotted together with the residual r_k as they decrease during the minimization. Initial estimates are based on the forward simulation starting with the GW reference model. Both r_k and ϵ_k decrease during the ADMM minimization. The estimates of ω_0 can be seen in the contour profiles in Figure 5.6, resp. Figure 5.7 for $x = 10$ and $x = 20$ m or their 3D plots in Figure 5.8.

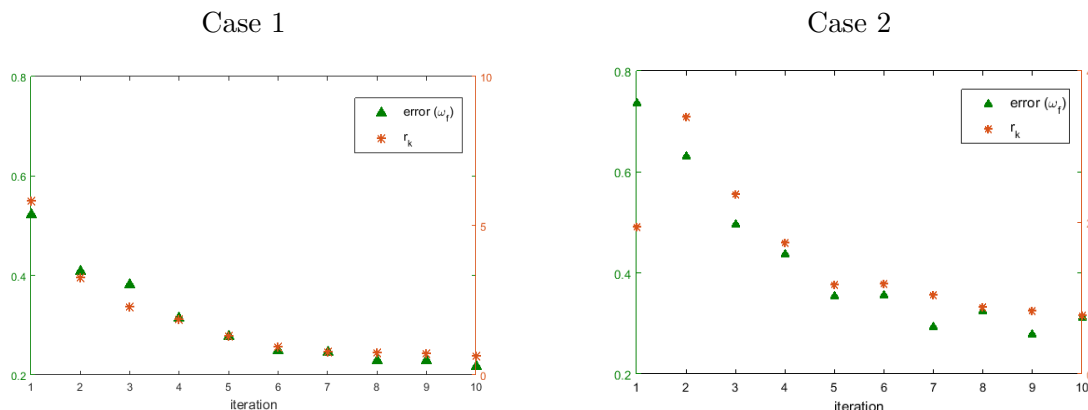


Figure 5.5: The error and residual decrease during the ADMM descents: Green triangles represent the scaled error for the final solute fraction ω_f , orange stars correspond to updated r_k values, where $r_k = \sigma_f(k) - p(\omega_f(k))$. The GW wells in this case were placed along $x = 16$ m and $x = 24$ m

For comparison, we also solved the inverse problem with a simpler coupled approach and by a Gauss-Newton method with a direct substitution (equation (4.23)). In the simple coupled approach both models can run independently. We first solve the inverse problem for GW data only and then apply Archie’s law to transform the estimate to electrical conductivity at t_1 . This estimate then constrains the geophysical inversion as a reference and initial model, and as such it is computationally easier to implement with no extra coupling terms in any of the objective functions. The actual errors of solute mass fraction at t_0 and t_1 and final data misfits for the ADMM and the coupled approach are presented in Table 5.2. In Table 5.2 we recorded for the coupled approach the lower error from GW or geophysical inversion. With the ADMM approach we decreased the error for the final solute fraction ω_f by roughly 50% compared to the coupled approach, and also decreased

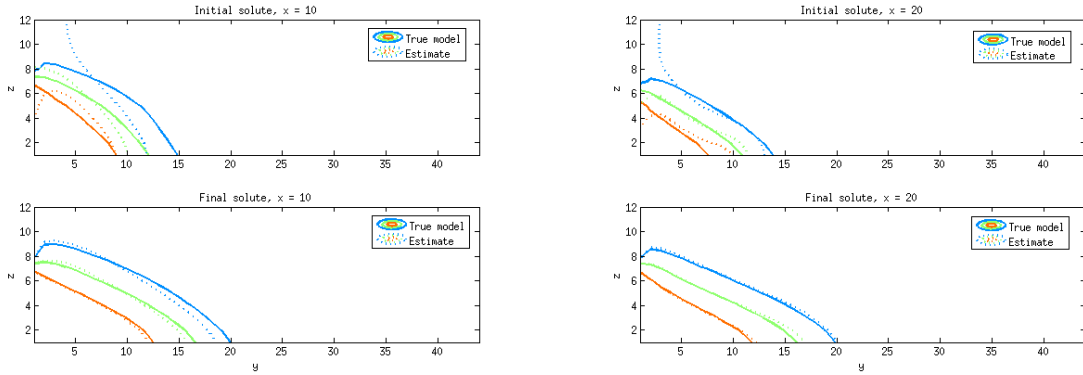


Figure 5.6: ADMM estimates for Case 1: Contour profiles at $x = 10$ and $x = 20$. The dashed lines are estimates from the joint inversion (ADMM), and the full contour lines are the actual locations corresponding to $\omega = 0.25$ (blue), $\omega = 0.5$ (green) and $\omega = 0.75$ (red).

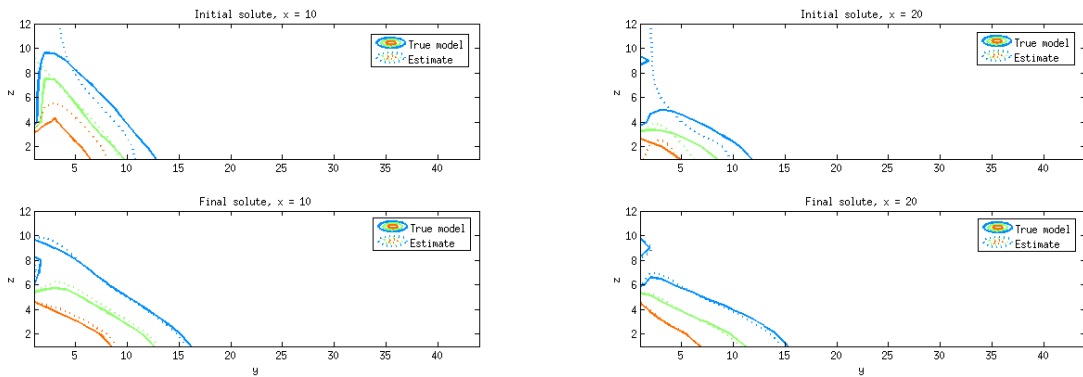


Figure 5.7: ADMM estimates for Case 2: Contour profiles at $x = 10$ and $x = 20$. The dashed lines are the estimates from the joint inversion (ADMM), and the full contour lines are for true locations corresponding to $\omega = 0.25$ (blue), $\omega = 0.5$ (green) and $\omega = 0.75$ (red).

the error for the initial estimate ω_0 .

Direct substitution

The Gauss-Newton minimization with a direct substitution for σ follows the objective function in equation (4.23). We run the Gauss-Newton minimization applying three different strategies of adjusting the weights and summarized the results for Case 1 in Table 5.3. In

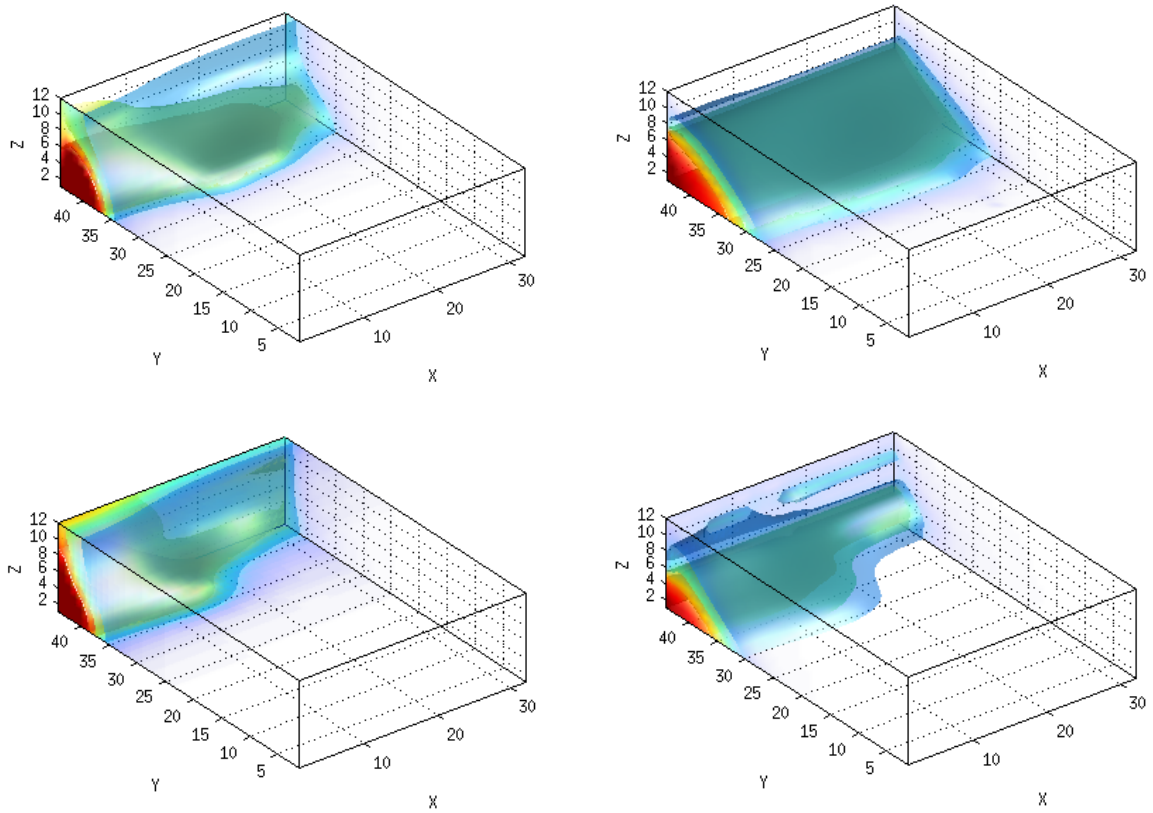


Figure 5.8: ADMM estimates. Upper left and right: Estimates for initial and final solute distribution for Case 1. Bottom left and right: Estimates for initial and final solute distribution for Case 2. Isosurfaces at $\omega = 0.25, 0.5$ and 0.75 are displayed. The true models are plotted in Figure 5.3

| Case 1 | $\epsilon(\omega_f)$ | $\epsilon(\omega_0)$ | $\phi_{GW}(\rho\omega)$ | $\phi_{DC}(u(\sigma))$ |
|-----------|----------------------|----------------------|-------------------------|------------------------|
| Initially | 14.2 | 22.6 | 14.4 | 1046 |
| Coupled | 6.28 | 13.56 | 4.6 | 1.6 |
| ADMM | 3.1 | 10 | 1.1 | 1.4 |
| Case 2 | | | | |
| Initially | 9.3 | 16.8 | 7.4 | 1940 |
| Coupled | 6.6 | 13.8 | 3.4 | 1.0 |
| ADMM | 2.8 | 11.5 | 0.8 | 0.9 |

Table 5.2: Errors, $\epsilon(\omega_k) = \|\omega_k - \omega_{true}\|$, for the solute content at time t_0 and t_1 for the two different cases.

the first option we initially fixed both δ_e and δ_f to make the initial data misfit magnitudes equal. In the second option we fixed the geophysical data misfit weight δ_e , and adjust the groundwater data misfit weight δ_f at each iteration as $\delta_f = \frac{\phi_{D,e}}{\phi_{D,f}}$. In the third option we were adjusting the geophysical weight δ_e instead, at each iteration as $\delta_e = \frac{\phi_{D,f}}{\phi_{D,e}}$. Since the estimates by substitution approach were worse than computationally much simpler coupled approach described above, we left the substitution approach out of further comparison.

| Case 1 | $\epsilon(\omega_f)$ | $\epsilon(\omega_0)$ | ϕ_{GW} | ϕ_{DC} |
|----------------------------|----------------------|----------------------|-------------|-------------|
| Initially | 14.2 | 22.6 | 974 | 1046 |
| Fixed δ_e, δ_f | 10.8 | 27.4 | 7.97 | 43.74 |
| Adjusted δ_f | 8.49 | 21.3 | 1.78 | 144.24 |
| Adjusted δ_e | 7.07 | 20.6 | 3.2 | 71.12 |

Table 5.3: Errors, $\epsilon(\omega_k) = \|\omega_k - \omega_{true}\|$, for the solute content at time t_0 and t_1 for Gauss-Newton method with the substitution of σ ; 1. The weights were fixed throughout the minimization based on the initial data misfits; 2. δ_f was adjusted as $\delta_f = \frac{\phi_{D,e}}{\phi_{D,f}}$ at each iteration; 3. δ_e was adjusted as $\delta_e = \frac{\phi_{D,f}}{\phi_{D,e}}$ at each iteration. GN inversion run up to 10 iterations.

Different GW experimental designs

Additionally, we tested the ADMM and the coupled approach for different locations of GW wells without changing the DC survey design. The scaled errors are plotted for all simulations in Figure 5.9. The different transects of wells are plotted in Figure 5.10. We did not use the same combinations of transects for Case 1 and 2, as the final SWI front reached further in the Case 2 compared to Case 1. In most of simulations we managed to substantially reduced the error for final solute mass fraction ω_f (about 25% of the initial error for homogeneous Case 1 and 35% for the heterogeneous Case 2). The errors for initial solute estimate were fairly consistent and satisfactory for the homogeneous Case 1 (50% reduction), less so for the Case 2 (60 to 80%).

5.1.3 Joint inversion by ADMM with inexact GW parameters

In order to test our method for the case, where the reservoir parameters are not known exactly or only approximately, we solve the problem for an inaccurate permeability field and dispersion. In the first test, we used the original GW model parameters, but decreased the homogeneous permeability field and dispersion to 70% when running the ADMM or coupled

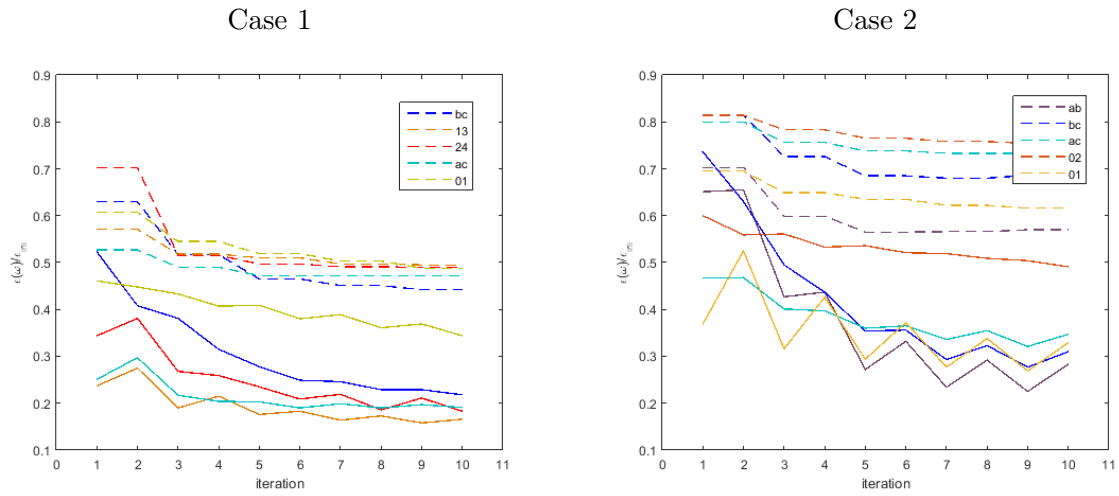


Figure 5.9: The relative error decrease for five different GW sampling designs; the dotted line is for the ω_0 relative error, the full line for the ω_f relative error decrease. In all cases the error decrease slows down with further iterations. The plotted results are based on different transects of wells plotted in Figure 5.10.

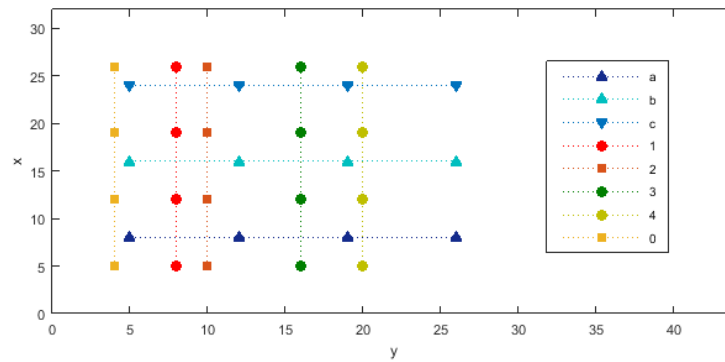


Figure 5.10: The transects along x and y axis in plan view. For the homogeneous Case 1 the sampling depths were $z = [3, 7, 11]$, and for the heterogeneous Case 2 $z = [5, 9]$. each design had two vertical or horizontal transects.

approach. The ADMM joint approach converged, but the actual errors were higher than when the correct GW parameters are used. In Figure 5.11 you can see the error evolutions for both the ADMM with correct and incorrect GW parameters, also the error $\epsilon(\omega_f)$ from the coupled approach (a single value), Table 5.4 provides the summary of errors for both methods.

In the second test, we used the homogeneous Case 1 and altered the permeability field by adding a 3D random Gaussian field to the original one (see in Figure 5.12). The addition of the Gaussian random field thus changed the original anisotropic homogeneous permeability field to a heterogeneous field, which leads to a differing solute distribution. The ratio of change in the observed solute fraction data due to different permeability compared to original data was 18%. GW data based on this simulation were used in ADMM inversion, but leaving the permeability field homogeneous as in the previous calculations for Case 1. For comparison we again ran the coupled approach with the same input as used in ADMM. The scaled errors and residual r_k are plotted in Figure 5.13 for both correct and incorrect GW parameters.

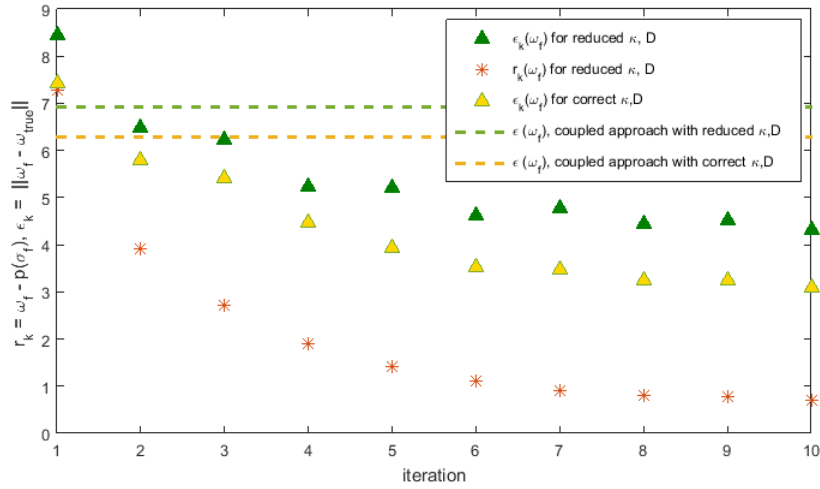


Figure 5.11: Altering the GW parameters: Errors decrease for ω_f estimate and residual r_k when correct and altered GW parameters (D, k) are used in ADMM. The errors for ω_f for the coupled approach are plotted as well with a dashed line, it is just a single value.

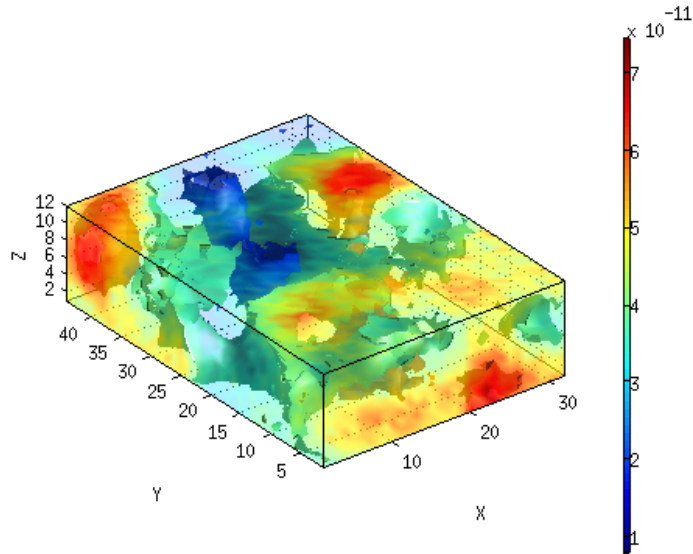


Figure 5.12: Altering the GW parameters: The true permeability field in x direction k_x in the second test. For solving the inverse problem a fixed value $k_x = 4.4 \cdot 10^{-11}$ was used instead, while the true field is shown in this figure. The true k_y and k_z were altered similarly when simulating GW data.

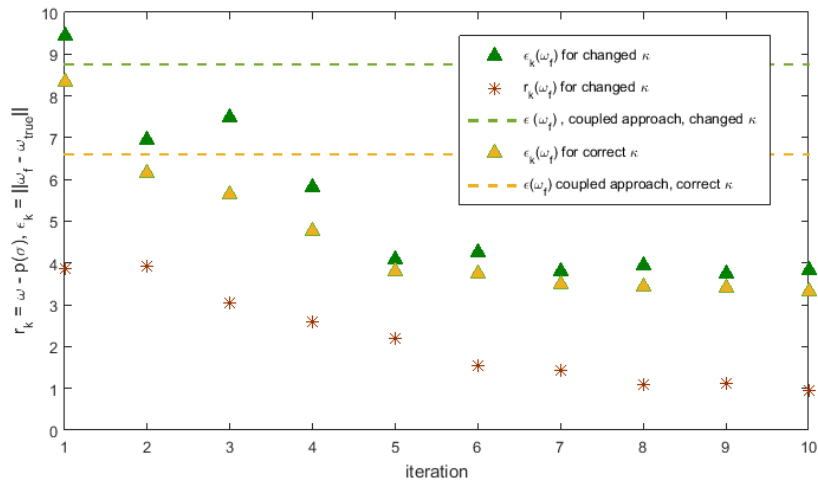


Figure 5.13: Altering the GW parameters: Errors decrease for ω_f estimate and residual r_k when correct and altered GW permeability is used in ADMM. The errors for ω_f for the coupled approach are plotted with a dashed line.

| Test 1 | $\epsilon(\omega_f)$ | $\epsilon(\omega_0)$ | $\phi_{GW}(\rho\omega)$ | $\phi_{DC}(u(\sigma))$ |
|-----------|----------------------|----------------------|-------------------------|------------------------|
| Initially | 12.2 | 20.7 | 63 | 1150 |
| Coupled | 7.35 | 16.2 | 3.64 | 2.18 |
| ADMM | 3.85 | 10.4 | 2.04 | 1.57 |
| Test 2 | | | | |
| Initially | 17 | 22.6 | 17.2 | 1140 |
| Coupled | 6.92 | 13.1 | 4.0 | 1.95 |
| ADMM | 4.32 | 9.26 | 1.7 | 1.48 |

Table 5.4: Errors, $\epsilon(\omega_k) = \|\omega_k - \omega_{true}\|$, for the solute content at time t_0 and t_1 when different from true GW parameters are used in the ADMM inversion or coupled approach. Test 1 - change in permeability field. Test 2 - 70% reduction in permeability and dispersion values.

5.1.4 Summary

We can conclude that the ADMM approach proved to be advantageous compared to the simple coupled approach, direct substitution of the constraint or the separate groundwater and geophysical inversions. In all tested examples, the joint inversion with ADMM achieved a lower error for both the initial and final solute fraction distributions compared to the simple coupled approach.

More particularly:

- Based on the different examples presented herein the error for ω_f estimate by ADMM was roughly 50% of the error by a coupled approach in homogeneous case, and 60% for the heterogeneous case. For the initial solute fraction ω_0 the improvement by ADMM was 60% and 70% respectively.
- The estimates for the final solute distribution were generally better than for the initial solute mass fraction due to the fact that the DC data were collected at the final time, and also the coupling constraint between ω_f , solute fraction, and σ_f , electrical conductivity was enforced for the final time t_1 .
- In all cases the ADMM converged to minimum, though it shows some of its typical aspects: a relatively quick drop during the first few iterations and a slow decrease towards the end. However, for the case of groundwater modeling applications, the initial decrease in error might be sufficient. Our synthetic study confirmed the theoretical results about the convergence of this method.

Of course, the ADMM comes at a higher computation cost compared to the simple coupled approach, which is due to the repeated computation of the GW and geophysical descent, for four or five times. For example, using the simple coupled approach for the Case 1, we ran the forward GW model 10 times, while the ADMM required 57 forward model runs. Similarly, the coupled approach required 7 DC forward model runs as opposed to 32 runs by ADMM. In the Table 5.5 we summarized the computation cost in terms of forward geophysical and groundwater model runs and the actual running time; we also included the time scale of the Gauss-Newton method with a direct substitution.

Note that, when the relative weighting and regularization parameters are unknown, the ADMM can be easily faster than the Gauss-Newton optimization (with substitution for ω_0), which also needs to be solved a number of times due to testing different regularization parameters, however, unlike ADMM, where each iteration consists of solving a single

physical model, the fully coupled Gauss-Newton method requires solving both problems for each weighting and regularization parameters.

| Method | GW f.m. runs | DC f.m. runs | time [min] |
|--|--------------|--------------|------------|
| Substitution (8 iterations) | 20 | 18 | 59 |
| Coupled (4 and 7 iterations) | 10 | 7 | 27 |
| ADMM (5 descents x 3 and 6 iterations) | 57 | 32 | 113 |

Table 5.5: Computational cost overview for the forward model (f.m.) runs and actual run time of the inversion; all results displayed were executed on a desktop with Intel(R) Core(TM)i7-2860 QM processor and 16GB RAM. Parameters for line search procedure were the same for all methods, amount of iteration counts is displayed in the brackets next to each method.

For the first set of simulations with Case 1 and Case 2 we assumed the GW model parameters were known, excluding the initial solute content. This can be regarded as an overly simplifying approach, but is justified for testing the feasibility of the joint inversion strategy. To demonstrate the robustness of the ADMM method with respect to variations in GW parameter values, we altered the GW model parameters in the inversion process. As expected, this led to estimates with higher error compared to solving the problem with the correct parameters. Nevertheless, the ADMM converged to estimates with lower error than the simple coupled approach (see in Figure 5.11), as it could be partially “corrected” by information from geophysical data. We are aware that further increasing of the error in the GW model parametrization would also lead to worse estimates, but in that case any coupled approach will not be able to provide a more accurate estimates.

5.2 Solute tracer test - Parameter and state estimation without an explicit petrophysical relationship

The solute tracer test provides a relatively simple case, on which we can test using implicit structure similarity measures. Abundant research has been published on the hydrogeophysical inversion for solute tracer tests, for both field and synthetic studies; however, only few studies have been published which did not use an explicit petrophysical link.

For example in [13] authors implemented a level set method in the objective function and assumed the parameter of interest is mainly affected by geological facies. The approach was tested with seismic and hydrological tomography data on a synthetic example. Due to the level set method there was no need for a direct link between seismic velocity and hydraulic conductivity; however, in this application the structure similarity was enforced by the a priori assumption, i.e. the knowledge of geological facies location, and could be applied only due to the fact that both geophysical and hydrological data were directly dependent on the same geological property.

A different way to alleviate the need of petrophysical relationship is to assume a strong correlation between the variables of interest, in the study of [54] between the solute concentration and soil bulk conductivity. In particular in their synthetic study for a solute tracer test, the authors used ERT time lapse sampling together with groundwater head and fluid conductivity data to determine the hydraulic conductivity. In their approach they maximized the correlation between transient changes in the fluid and soil bulk conductivity and thus avoid solving the ERT inversion; the input for the ERT forward model were fluid conductivity changes alone. The correlation “coupling” term was then added when solving the standard groundwater inverse problem to estimate hydraulic conductivity. The hydraulic head and fluid conductivity sensitivities were solved by perturbation method in parallel and hydraulic conductivity was parametrized by Pilot points method with a linear interpolation; a high performance cluster was necessary to run the inverse problem. The presented example showed that even indirect geophysical information can improve the estimates for hydraulic conductivity.

To our knowledge, the first work applying a structural constraint in hydrogeophysical inverse problem is the study of Lochbuhler et al.[65]. The authors combined two datasets, ground-penetrating radar data with hydraulic tomography or tracer mean arrival times, to estimate hydraulic conductivity. A cross product of the spatial gradients of the geophysical and groundwater models was implemented as a structural constraint, creating a penalty

in the coupled objective function. Their study tested the structural coupled approach on 2D synthetic case as well as field data from the Widen gravel aquifer in Switzerland. The recovered models did indeed displayed similar structure, though not following a simple linear petrophysical relationship, and the hydraulic conductivity estimates were in accordance with previous field studies.

In our synthetic case, we implemented a full 3D inversion and jointly inverted the geophysical and hydrological data that are not directly dependent on the property of interest. We used the Cross Gradient field product as a structure similarity coupling term in the objective function in Eq. 4.30 and solved the inverse problem for either initial solute state or hydraulic conductivity field. Two computationally different methods, Block Coordinate Descent (section 4.4.1) and Joint Gauss Newton (section 4.4.2) were tested and compared with the results of separate geophysical and groundwater inversions.

5.2.1 Parametrization

We set up two different concentration plumes, first one is initially a standard Gaussian plume (Example 1), and the second one has a more complex shape (Example 2). For the first two examples we estimate the initial conditions for solute concentration, c_0 , in the last case (Example 3) we used the same initial concentration as in Example 1 but estimate the hydraulic conductivity K instead. For each case, the boundary conditions are set either no flow or fixed head boundary, such that the natural hydraulic head gradient is along the x coordinate. Injection and pumping wells are placed in the domain to create flow pathways also along the y and z axis. The solute plume moved from time t_0 to time t_1 , and the solute content at t_1 was then transformed via Archie's law to create an electrical conductivity model, and as such used in the Example 1. To imitate more realistic cases, in the subsequent examples the electrical conductivity model was altered by adding a heterogeneous spatially correlated field of more conductive material (see in Figure 5.14) than background. The actual parameters for both the groundwater and geophysical models can be found in Table 5.6.

Both groundwater and geophysical data were collected at a single instance of time, t_1 , though multiple time collection would not change computationally the algorithms presented in chapter 4. The groundwater measurements were collected from a few nested wells, to obtain solute concentration data. For the Example 3 we also recorded the hydraulic head data.

Table 5.6: Parametrization for the solute tracer Examples 1, 2 and 3.

| | |
|---------------------------|--|
| GW model | |
| Grid | 42x32x16 cells |
| Cell size | 1 x 1 x 1 m |
| Hydraulic conductivity K | |
| Example 1,2 | $k_x = 1m/d, k_y = 0.6m/d, k_z = 0.4m/d$ |
| Example 3 | $k_{x,y,z}, \log(\mu) = -1.8m/d, \sigma = 1, l_{x,y,z} = (60, 40, 10)$ |
| Dirichlet BC along x | $h(x = 0) = 21.6$ m, $h(x = 42) = 20$ m |
| Porosity ϕ | 0.35 |
| Dispersion D | $0.02 m^2/d$ |
| Q_{GW} , injection rate | $[x,y] = [8,8], 4 d^{-1}$ |
| Q_{GW} , pumping rate | $[x,y] = [34,18], 3.3 d^{-1}$ |

| | |
|---------------------|--------------------|
| Geophysical model | |
| Grid | 50 x 38 x 16 cells |
| Cell size | 1 to 4 m |
| Arhie's law m | 1.7 |
| Background σ | 0.0065 S/m |

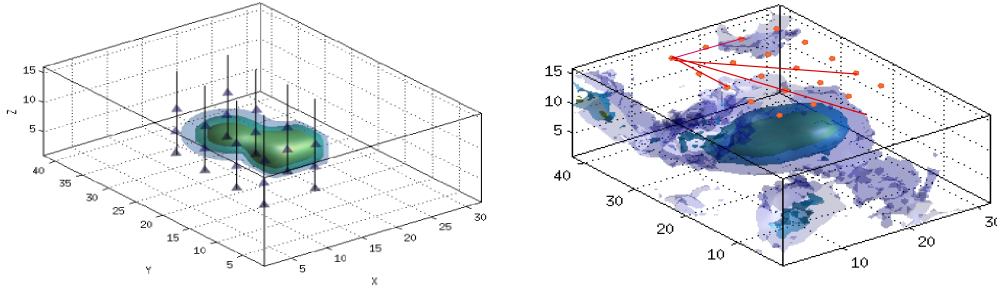


Figure 5.14: Solute tracer test. Left: A scheme for the GW survey design with two transect of wells, applied in Example 1 and 2. Right: A scheme for DC survey with receivers on surface only, in the background is the electrical conductivity model applied in Example 2 which spatially correlated more conductive field than background.

The placing of the wells has a huge impact on the inverse problem solution and it is generally hard to design without the actual knowledge of the solute plume location; therefore, we ran all the examples for different groundwater experimental designs, with wells randomly chosen from a regular grid of 4 x 5 sampling locations. All different GW surveys wells locations are plotted in Figure 5.15.

For the geophysical survey, the potentials were measured using surface electrodes only. A regular grid spacing was 4 m and 3m along the x and y coordinate. The source electrode couple was moved along x (north - south) coordinate and for each source the potentials

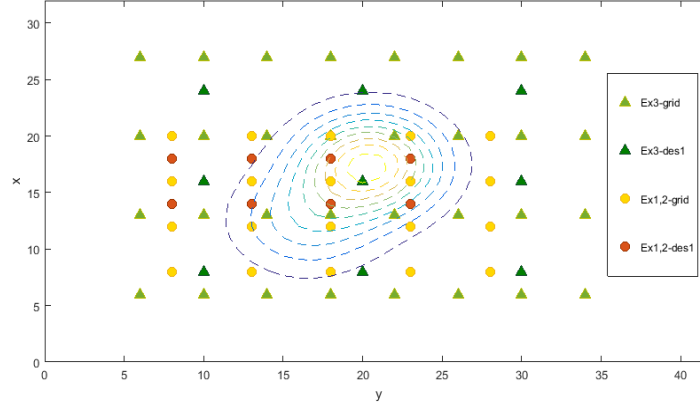


Figure 5.15: Different GW surveys for solute tracer test. Ex 1,2 - des1: Two transects of wells at $x = 14$ and 18 m applied in Example 1 and 2. Ex 1,2 - grid: 4×5 grid of wells from which 8 locations was chosen randomly for each run. Ex3-des1: 3×3 grid of wells locations for results presented in Table 5.11. Ex3-grid: Regular grid of well from which 10 wells were randomly chosen, corresponding results summarized in Table 5.12

| | | GW model | Geophysical model |
|------------|--------------------|-----------------------|-----------------------|
| Weights | α | $1e-3$ | $1e-4$ |
| | β_0 | 2^7 | 2^7 |
| | β | $0.5 \phi_D / \phi_S$ | $0.5 \phi_D / \phi_S$ |
| Iterations | separate inversion | 4 | 6 |
| | BCDM, GW / DC max | 3 | 4 |
| | JGN, | 7 | 7 |
| | Conjugate gradient | 8 | 8 |

Table 5.7: Minimization parameters for the inverse problem

were measured by all receivers with one electrode being fixed and located in the south-east corner. The design follows the one already used in the seawater intrusion example.

For all tested scenarios we first ran separate inversion for groundwater and geophysical data alone, and afterward, we apply two computational approaches for the joint inversion, Gauss-Newton method (JGN) to update both the groundwater and geophysical models at once, and BCDM with up to four groundwater or geophysical descents. Each inversion was stopped when the data misfit dropped below expected error or when the maximum of iterations was reached. The iterations and weights setup are summarized in Table 5.7.

To compare the different methods for parameter or state estimation, we computed the norm of errors (since the true parameters are known) for the initial and final solute

estimates, soil bulk electrical conductivity and in the last example also for the hydraulic head and conductivity estimates. We also evaluated the Cross Gradient similarity term before and after the structure coupled minimization. The visual comparison is somewhat limited as all the examples are in 3D, however, vertical and horizontal slices are presented.

5.2.2 Example 1 and 2: Estimation for initial state c_0

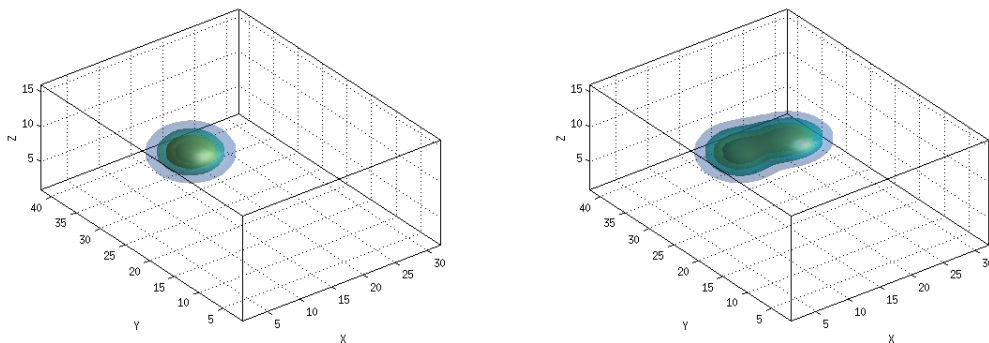


Figure 5.16: Solute tracer test. The true models for the initial solute concentration in Example 1 (left) and Example 2 (right), isosurfaces displayed at $c_0 = 0.2, 0.4, 0.6$ and 0.8 .

First, we applied the inversion framework to a simple case of a solute tracer test where the initial solute plume has a Gaussian shape (see in Figure 5.16). The true solute content c^n is related to electrical conductivity σ via Archie's law. Solute concentration and geophysical potentials were collected at time t_n . In the Table 5.8 we summarized the results of separate inversions and joint inversion with block coordinate method (BCDM) and direct Gauss-Newton method (JGN) for a particular placing of the GW wells (marked in Figure 5.15 as Ex1,2-des1). We recorded the final error estimates, data misfits and a drop in the similarity penalty term, cross gradient product ϕ_{CGP} . These errors are visualized in the bar plot in Figure 5.17, the separate (GW data only) inversion decreased the initial error of c^n to 60% while BCDM decreased the error to 45%. The joint inversion solved with JGN had worse performance, with 55% error decrease only. The errors for the estimate of initial solute differed less among the applied methods, separate inversion had 72%, BCDM 65% and JGN 70%. Although all results were computed in 3D, in the Figure 5.18 we show the 2D contour plots of solute estimates for c_n along $y = 16$ and depth slices at $z = 8$, the initial

solute estimates are plotted for $z = 8$.

| Method | $\epsilon(c_n)$ | $\epsilon(c_0)$ | $\phi_D(c_n)$ | $\epsilon(\sigma)$ | $\phi(\sigma)$ | $\Phi_{CGP}(\hat{c}_n, \sigma)$ | $\Phi_{CGP}(c_n, \hat{\sigma})$ |
|-----------------------------|-----------------|-----------------|---------------|--------------------|----------------|---------------------------------|---------------------------------|
| GW | 5.20 | 7.06 | 2.71 | - | - | 24.9 | - |
| DCI | - | - | - | 4.93 | 2.16 | - | 34.0 |
| JHI (GNm) with ϕ_{CGP} | 4.81 | 6.88 | 8.12 | 4.18 | 7.95 | 19.03 | 2.88 |
| BCDM with ϕ_{CGP} | 3.94 | 6.35 | 1.15 | 4.32 | 16.9 | 17.05 | 1.46 |

Table 5.8: Example 1: Summary of the errors for the solute distribution and electrical conductivity estimates, the data misfits and the cross-gradient coupling terms (between the estimate and the true field) by either separate inversion or joint inversion with cross-gradient product.

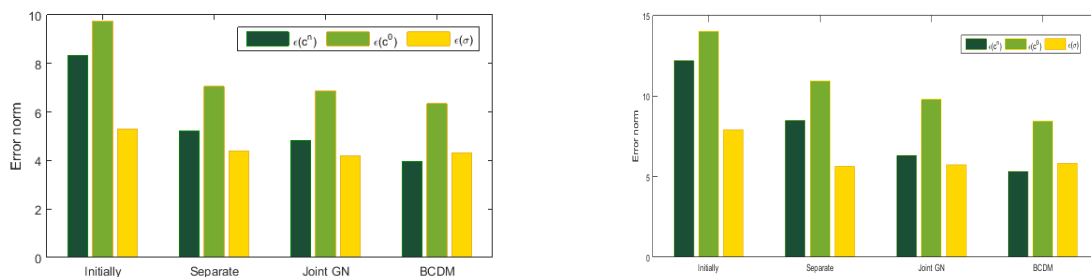


Figure 5.17: Example 1 and Example 2: Bar plots for the error estimates by different methods, the actual values are in Table 5.8, Table 5.10 respectively.

| Error | \hat{c}_n | \hat{c}_0 | $\hat{\sigma}$ |
|--|-------------|-------------|----------------|
| Example 1 mean ($\epsilon_{JGN}/\epsilon_{GWI/DC}$) | 0.88 | 1.25 | 0.98 |
| Example 1 mean ($\epsilon_{BCDM}/\epsilon_{GWI/DC}$) | 0.84 | 0.91 | 1.00 |
| Example 2 mean ($\epsilon_{JGN}/\epsilon_{GWI}$) | 0.91 | 0.99 | 1.1 |
| Example 2 mean ($\epsilon_{BCDM}/\epsilon_{GWI}$) | 0.78 | 0.84 | 1.11 |

Table 5.9: Example 1 and 2: Summary of the relative errors (joint inversion vs GW (or DC) data only) for the solute distribution and electrical conductivity estimates based on the results from 10 different GW survey designs.

For the Example 2 we altered the true initial solute distribution by adding a spatially correlated field of higher conductivity (see in Figure 5.16). Unlike in the previous example, the corresponding soil bulk conductivity is therefore not linearly dependent on solute concentration model. The summary of the estimate errors by different methods can be found in Table 5.10 and the slices of the actual estimates are plotted in Figure 5.19 for a particular

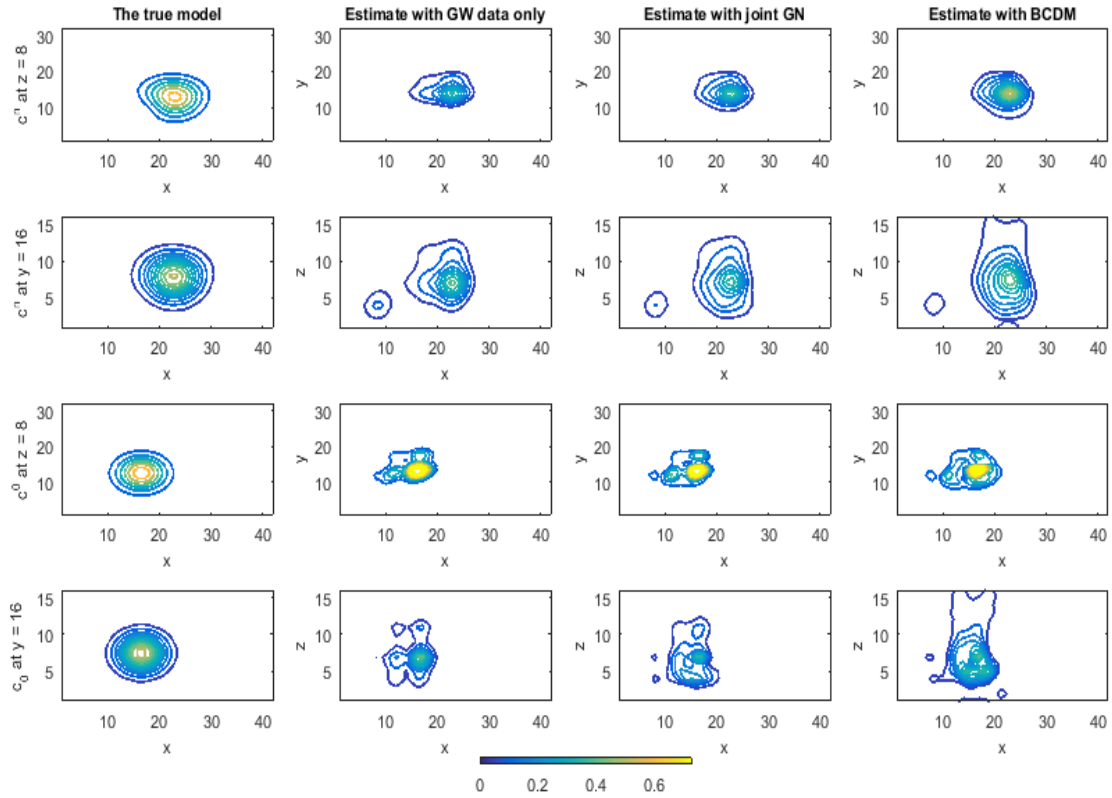


Figure 5.18: Example 1: The true models vs the estimates by GW data inversion and structure-coupled inversion, contours at $z = 8$ and $y = 18$ for final and initial solute c^n, c^0 are plotted.

well placing. Similarly as in Example 1, BCDM had lower errors than JGN, decreasing the initial error to 43% for the solute content c^n , and to 54% for c^0 . The separate inversion with GW data only decreased the error to 58% for c^n , respectively 70% for c^0 . The estimates for electrical conductivity were comparable regardless the method, only BCDM with Archie's law lead to significant estimate error reduction.

Afterward, we ran both Example 1 and 2 for different GW survey designs; each time eight wells locations were randomly picked from a regular grid covering the area of plume movement. In Table 5.9 we summarized the results of these experiments, the actual errors for each run of Example 2 setting are plotted in Figure 5.20. On average, BCDM reduces the error of the final solute content by 16 % in Example 1, and by 22 % in Example 2

compared to GW data inversion alone. For the initial solute the drop was 9% and 21% respectively. JGN also reduced the final c^n estimate errors, but has not improved the initial solute estimate compared to GW data inversion.

| Method | $\epsilon(c_n)$ | $\epsilon(c_0)$ | $\phi_D(c_n)$ | $\epsilon(\sigma)$ | $\phi(\sigma)$ | $\Phi_{CGP}(\hat{c}_n, \sigma)$ | $\Phi_{CGP}(c_n, \hat{\sigma})$ |
|-----------------------------|-----------------|-----------------|---------------|--------------------|----------------|---------------------------------|---------------------------------|
| GWI | 7.03 | 9.43 | 0.9 | - | - | 108.3 | |
| DCI | - | - | - | 6.85 | 6.4 | - | 32.6 |
| JHI (GNm) with ϕ_{CGR} | 6.29 | 8.53 | 6.8 | 7.04 | 7.1 | 73.9 | 9.4 |
| BCDM with ϕ_{CGR} | 5.18 | 7.29 | 0.9 | 6.93 | 7.3 | 32.6 | 6.9 |

Table 5.10: Example 2: Summary of the errors for the solute distribution and electrical conductivity estimates, the data misfits and the cross-gradient coupling terms (between the estimate and the true field) by either separate inversion or joint inversion with cross-gradient product.

5.2.3 Example 3: Estimation for hydraulic conductivity K

The 3D variable hydraulic conductivity K is usually parametrized so that its dimension is reduced. Multiple approaches, which can be generally cast as a linear combination of some M basis vectors (where M is usually much smaller than the mesh size) can represent the hydraulic conductivity K [76]. The simplest case is a zonation technique, where these basis vectors are constant over a part of the domain and zero everywhere else. Another common option is a pilot point technique; the hydraulic conductivity values are fixed at some points and the rest of the domain is determined by krigging interpolation. The choice of the locations of these points, or adding additional ones during the minimization leads to different approaches, examples can be found in [82, 86].

For Example 3 we assumed that the hydraulic conductivity field is log-normally distributed with some average value μ and covariance \mathbf{C} .

$$\ln(K) \approx N(\mu, \mathbf{C})$$

The covariance \mathbf{C} is usually derived assuming Gaussian or exponential correlation lengths in the x, y and z direction and some known variance (sometimes referred to as a semi-variogram). The semivariogram values are mostly obtained from geology borehole logs or other available data. Such geostatistical conceptualization is widely used, for example in [51] or [79]. Given this geostatistical interpretation, it is possible to apply Karhunen-Loeve

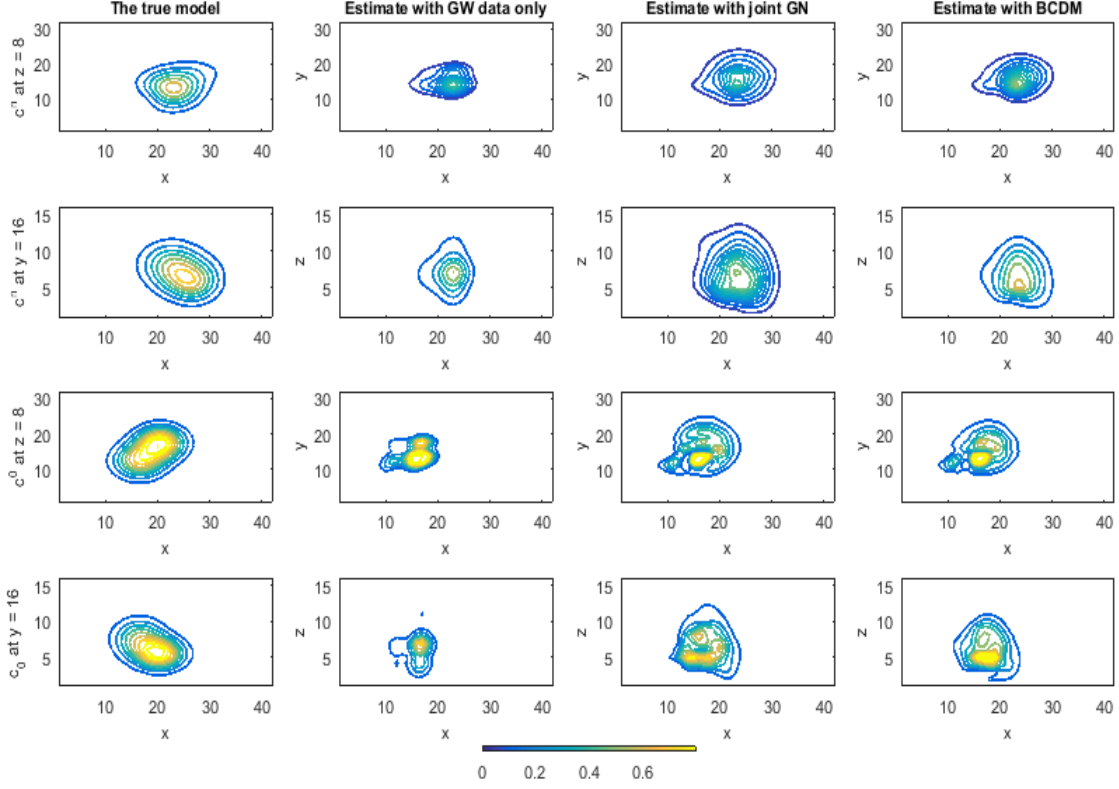


Figure 5.19: Example 2: The true models vs the estimates by GW data inversion and structure-coupled inversion, contours at $z = 8$ and $y = 18$ for final and initial solute c^n, c^0 are plotted.

decomposition and write the covariance for the discrete hydraulic conductivity field as

$$\mathbf{C} = \sum_{j=1}^N \lambda_j \mathbf{v}_j \mathbf{v}_j^\top, \quad (5.1)$$

where \mathbf{C} is an $N \times N$ discretization of the covariance operator, \mathbf{C} , the vectors, \mathbf{v}_j are its eigenvectors, that is, $\mathbf{v}_i^\top \mathbf{v}_j = 0$ if $i \neq j$ and 1 otherwise and λ_j are the (positive) eigenvalues.

When solving the inverse problem, we do not need to work with a full decomposition of the covariance matrix and rather replace it with the first M basis vectors,

$$\ln(\mathbf{K}) = \mu + \sum_{j=1}^M \mathbf{w}_j m_j = \mu + \mathbf{V} \mathbf{m} \quad (5.2)$$

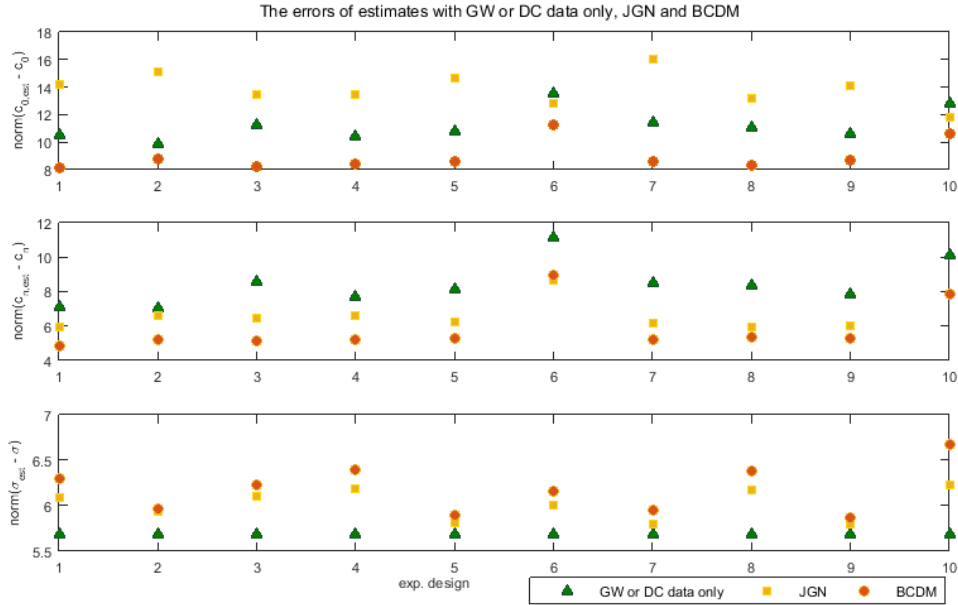


Figure 5.20: Example 2: The estimates for 10 different experimental designs, altering location of 8 wells from Ex 1,2 - grid design.

where $\mathbf{w}_j = \sqrt{\lambda_j} \mathbf{v}_j$ and $\mathbf{V} = [\mathbf{w}_1, \dots, \mathbf{w}_M]$. M should be large enough to capture the heterogeneity of the conductivity field K . This significantly reduces the size of the inverse problem to estimating the weights of these M basis functions, stored in the vector \mathbf{m} ; however, the drawback is that we limit any solution to a Gaussian random field given by the covariance matrix \mathbf{C} .

The unknown conductivity field K was thus parametrized as

$$K = \exp(\mu + \mathbf{V}\mathbf{m}), \quad (5.3)$$

and the covariance matrix in this example was computed based on Gaussian exponential model:

$$\mathbf{C}_{i,j} = -\frac{1}{2}\sigma^2 \exp\left(-\frac{(\mathbf{x}_i - \mathbf{x}_j)^2}{v}\right), \quad (5.4)$$

where v corresponds to correlation lengths in the x, y or z direction, σ is variance and $(\mathbf{x}_i - \mathbf{x}_j)$ is the distance between the two points. The values of vector v and σ^2 are later used to numerically solve the Karhunen - Loeve expansion of the covariance matrix \mathbf{C} up

to the first M vectors.

The number M can be estimated from the plot of eigenvalues, and verified by simply solving a linear least square problem with the actual data for $\ln(\mathbf{K})$:

$$\hat{\mathbf{m}} = (\mathbf{W}^\top \mathbf{W})^{-1} (\mathbf{W}^\top \ln(\mathbf{K})),$$

where \mathbf{W} is the matrix containing the basis vectors from the covariance matrix decomposition and a unit vector e representing the mean μ ; $\mathbf{W} = [e \ \mathbf{V}]$. The “reduced” hydraulic conductivity $\mathbf{K}(\hat{\mathbf{m}})$ can be then compared against the true hydraulic conductivity \mathbf{K} . In our case M ranged in the interval (30,60) to sufficiently describe the heterogeneity of the hydraulic conductivity, however this number is strongly dependent on the vector of correlation lengths v . The decomposition of the matrix \mathbf{C} was solved numerically using Cholesky factorization with Matlab built-in routines. Lanczos algorithm would be an alternative for large scale problems.

The setup of Example 3 is the same as in previous cases except that now we have a heterogeneous hydraulic conductivity \mathbf{K} and hydraulic head data were collected next to the solute concentration data, providing indirect information about hydraulic conductivity. First, we placed nine wells in regular spacing (see in Figure 5.15) and the inversion parameters were initially set as zero for the \mathbf{m} weights, and initial mean value $\mu_0 = -1$ and $M = 35$. We again recorded the estimate errors for final solute content and electrical conductivity, but this time also for hydraulic head, μ and $\ln(\mathbf{K})$ in the Table 5.11.

Afterward, we run the inversions for different groundwater sampling designs, choosing randomly 10 wells from the well points grid (5.15). The summary of these results can be found in Table 5.12 and the actual errors are plotted in the Figure 5.23. For all results the vector \mathbf{m} was set initially as zero vector, and the initial mean value as $\mu^0 = -1$.

In summary, the closer was the initial μ estimate to the true value, the better estimates (lower actual error) of solute distribution were obtained. The errors of the estimates of hydraulic conductivity and also final solute c^n were lower for BCDM and JGN compared to GW data inversion alone, however not in all cases BCDM outperformed uncoupled inversion and in some cases the final estimates were fairly comparable. On average JGN did not manage to minimize the hydraulic head data misfit, and BCDM had therefore overall better performance.

| Method | $\epsilon(c_n)$ | $\epsilon(h)$ | $\epsilon(\sigma)$ | $\epsilon(K)$ | $\hat{\mu}$ | $C(\hat{c}_n, \sigma)$ | $C(c_n, \hat{\sigma})$ |
|-----------------------------|-----------------|---------------|--------------------|---------------|-------------|------------------------|------------------------|
| GWI | 5.18 | 36.8 | - | 78.9 | -2.26 | 50.41 | - |
| DCI | - | - | 3.37 | - | - | - | 6.32 |
| JHI (GNm) with ϕ_{CGR} | 4.41 | 38.7 | 4.56 | 68.6 | -1.54 | 26.99 | 4.32 |
| BCDM with ϕ_{CGR} | 3.52 | 20.1 | 3.64 | 63.6 | -1.93 | 35.23 | 0.85 |

Table 5.11: Example 3: Estimation of hydraulic conductivity with KL expansion parametrization: Summary of the errors for the solute distribution, electrical conductivity and hydraulic conductivity estimates (and also the estimate for $\mu = \text{mean}(K)$, the true value was $\mu = -1.8$) by either separate inversion or joint inversion with cross-gradient product. A final cross-gradient product between c^n and σ is displayed too.

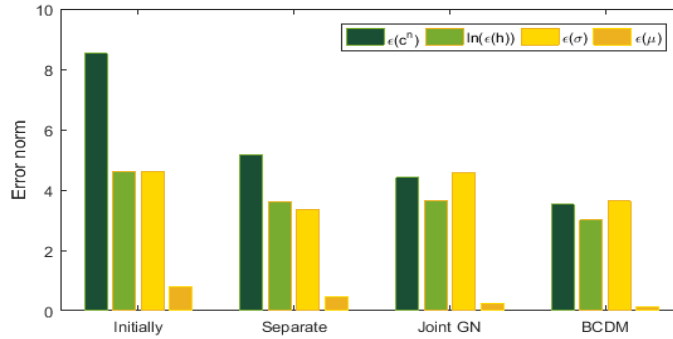


Figure 5.21: Example 3 : Bar plot for the errors by different methods, the actual values are in Table 5.11

| Error | \hat{c}_n | \hat{h} | $\ln(\hat{K})$ |
|---|-------------|-----------|----------------|
| Example 3 mean ($\epsilon_{JGN}/\epsilon_{GWI}$) | 0.88 | 2.15 | 0.86 |
| Example 3 mean ($\epsilon_{BCDM}/\epsilon_{GWI}$) | 0.77 | 0.92 | 0.8 |

Table 5.12: Example 3: Summary of the relative errors (joint inversion vs GW data only) for the solute distribution at c_n , hydraulic head h and logarithm of errors for conductivity K based the results from 10 different GW survey designs.

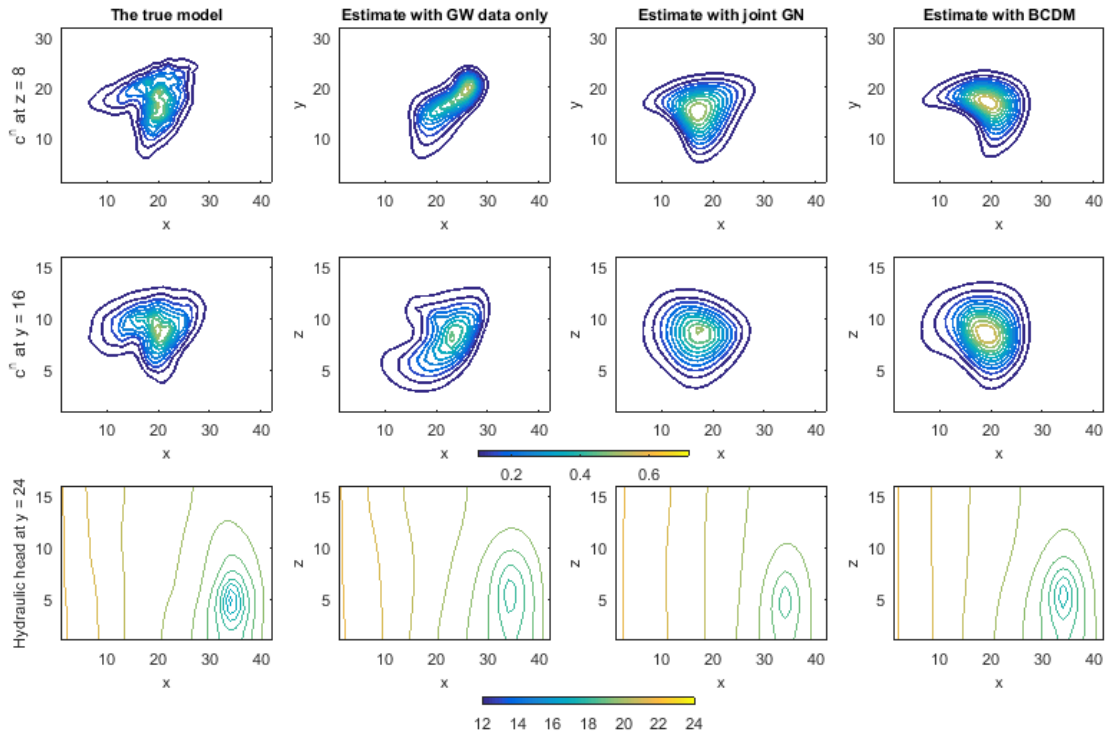


Figure 5.22: Example 3: The true models vs GW data and structure-coupled inversion estimates for the final solute concentration, contours at $z = 8$ and $y = 16$ are plotted and hydraulic head at $y = 24$.

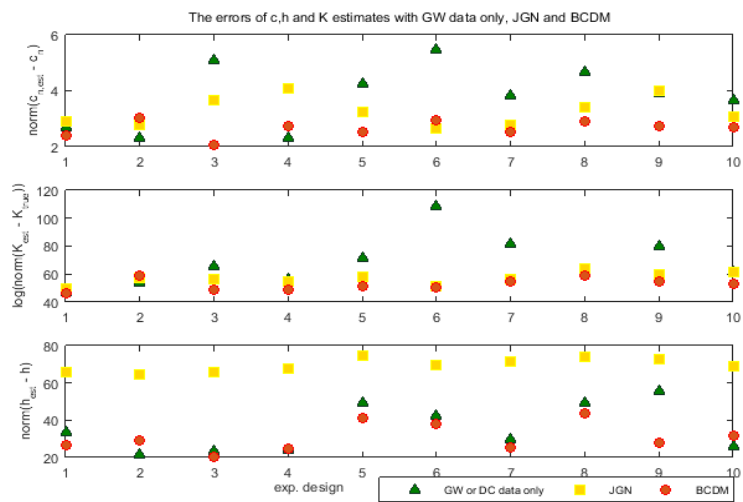


Figure 5.23: Example 3: The estimates for 10 experimental designs by different methods, altering the location of 10 wells in Ex3-grid design.

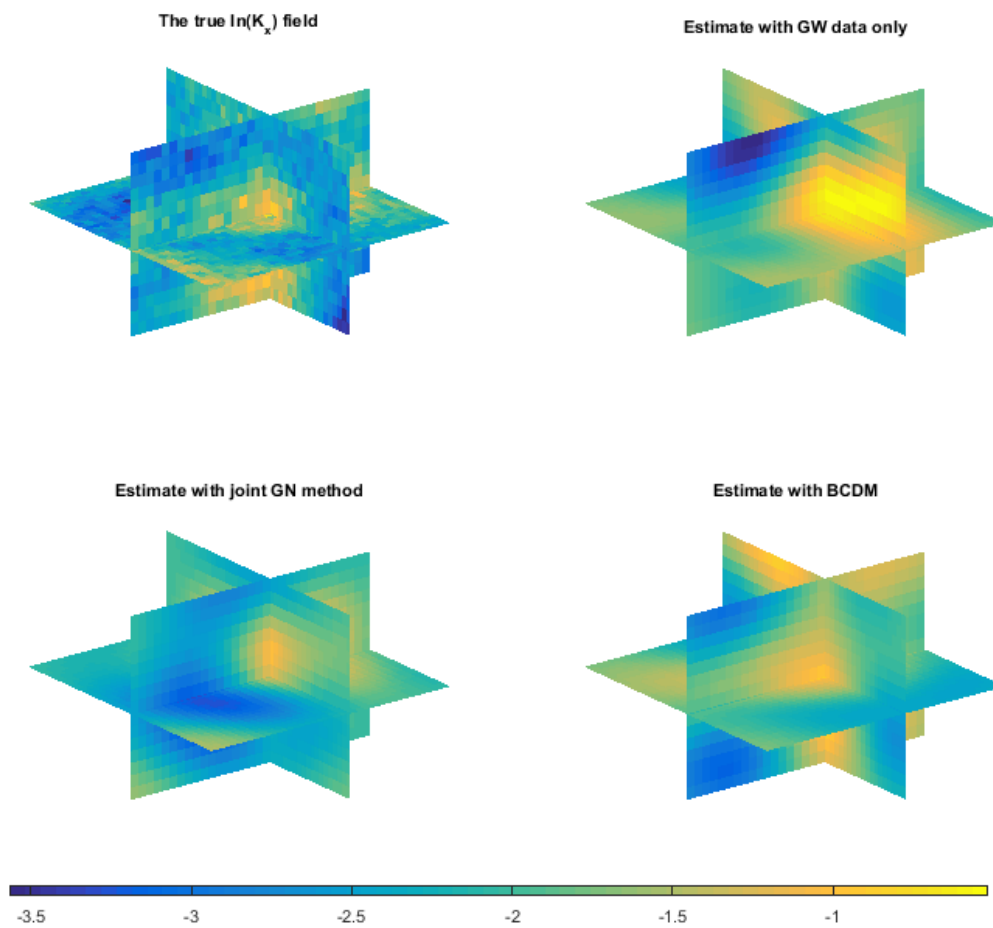


Figure 5.24: Example 3: The true field and estimates of hydraulic conductivity K by GW data only and JGN and BCDM.

5.2.4 Summary

Both methods, separate data inversion and joint approaches, were able to minimize the data misfits and provide physically realistic estimates for both hydrological and geophysical models. The coupled framework (joint inversion) reached better estimates for both initial solute content and hydraulic conductivity in most of the scenarios presented above and thus gave a promising improvement without a need for an explicit petrophysical link.

In particular, from evaluating the numerical results and comparing the actual estimates we can conclude the following points:

State estimation (Examples 1,2)

- BCDM had the lowest errors for both the initial and final solute estimate;
- JGN had lower errors for the final solute estimate in all cases compared to GW data inversion alone, however, for most experimental designs the initial solute estimate was worse than in GW data inversion alone;
- Soil bulk conductivity estimates were not improved by the joint inversion (both JGN and BCDM);
- The more complex Example 2 (no linear relationship between soil conductivity and solute content) lead to improvements for both BCDM and JGN methods compared to GW data inversion alone.

Parameter estimation (Example 3)

- JGN and BCDM provided comparable results in terms of $\epsilon(\mathbf{K})$ and $\epsilon(c)$;
- The initial estimate for μ does influence the final errors;
- In the hydraulic head estimation JGN performed worse than both GW data inversion and BCDM;
- The main features of the heterogeneous hydraulic conductivity \mathbf{K} were captured by both coupled and uncoupled inversion framework, however GW data inversion converged towards higher contrast in \mathbf{K} .

- To our knowledge, no structural inversion have been done using a parametric approach. Here, we explore the use of parametric approach together with a structural coupling.

The GW inversion is mainly limited by the scarce groundwater data, and as such it could not provide better results without implementing some smooth regularization, however, in that case, “a-priori” information needs to be introduced, which can not be always justified. Adding a coupling term in a form of structure similarity measure better constrains the ill-posed GW inverse problem and complements the GW data. This observation also partially explains why in Example 2 BCDM provided on average better estimates than in Example 1. Example 1 was set as a simple Gaussian plume, and thus standard L_2 regularization within GW inversion alone gave satisfying results, however, if more complexity is added (Example 2), then, the geophysical contribution within the CGP term contained sufficient information to constrain the estimates.

Both JGN and BCDM were easier to implement for the state estimation of the solute content c_0 , due to easier derivation of the data sensitivities. The coupled approach for state estimation had better results when compared with the coupled approach for parameter estimation. This stems from the fact that the similarity measure term is coupling the solute content c with the electrical conductivity σ . Other GW parameters such as hydraulic conductivity or, say, boundary fluxes are related to solute content c via the GW flow model only and this dependency has then a major effect on the success of parameter estimation.

5.3 Joint inversion with electromagnetic loop survey

The presented results follow the seawater intrusion example, except that now we have TDEM data instead of DC resistivity data. The details of this example were already described in section 5.1, and here we want to test the robustness of the ADMM approach if the geophysical data are altered. The groundwater model boundary conditions and forward simulations are identical, and again we estimate the initial and final solute distribution for the two cases with the homogeneous and heterogeneous permeability field, Case 1 and Case 2 (see Table 5.6).

To model geophysical electromagnetic data we placed a transmitter loop at the center of the area on surface. The current was initially shut down to produce changes in magnetic field, which were then recorded by receiver coils placed in a uniform grid on surface (see Figure 5.25 for the experimental design scheme). 3% Gaussian random noise was added to the measured data.

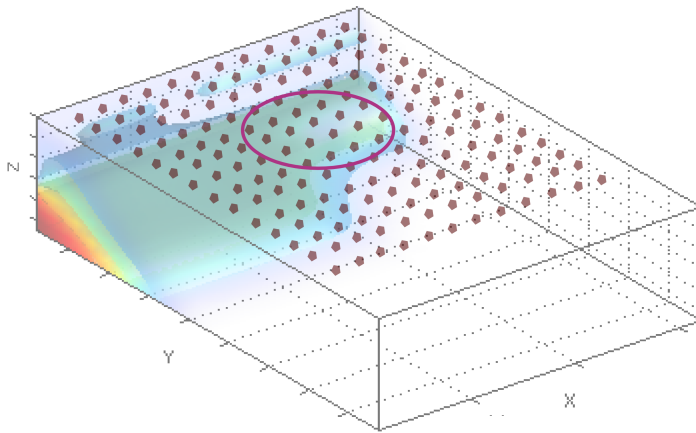


Figure 5.25: The experimental design for EM survey: Loop (transmitter) is placed in the center on surface, the receiver coils are placed on surface in an uniform grid.

For the GW experimental survey we again used the two transects at $x = 16 m$ and $x = 24 m$, with four wells each, to collect solute mass fraction data from three depth samples.

5.3.1 Joint inversion with ADMM

The ADMM starts with a groundwater descent, and continues as long as the constraint residual r_k decreases. The weights were set as $\alpha_e = 10^{-9}$, $\alpha_f = 5 \times 10^{-3}$ and $\rho = 0.4$. The summary of results for the case with well transects along $x = 16 \text{ m}$ and $x = 24 \text{ m}$ is in Table 5.13, Figure 5.26 shows the scaled errors (ϵ_k/ϵ_0) and the residuals r_k during each descent of ADMM method for this particular survey. Similarly as the results in section 5.1 showed for DC resistivity data, also when coupling groundwater with electromagnetic data the ADMM had the lowest errors for both initial and final solute mass fraction estimates.

| Case 1 | $\epsilon(\omega_f)$ | $\epsilon(\omega_0)$ | $\phi_{GW}(\rho\omega)$ | $\phi_{DC}(u(\sigma))$ |
|-----------|----------------------|----------------------|-------------------------|------------------------|
| Initially | 14.2 | 22.6 | 14.4 | 1.2 e5 |
| Coupled | 6.1 | 15.3 | 5.1 | 70.8 |
| ADMM | 2.6 | 13 | 2 | 69 |
| Case 2 | | | | |
| Initially | 9.3 | 16.8 | 7.4 | 7.1 e5 |
| Coupled | 5.2 | 14.1 | 2.9 | 75.7 |
| ADMM | 2.0 | 10.4 | 1.8 | 71.3 |

Table 5.13: Errors for the initial and final solute content at time t_0 and t_1 for the two different Cases 1 and 2.

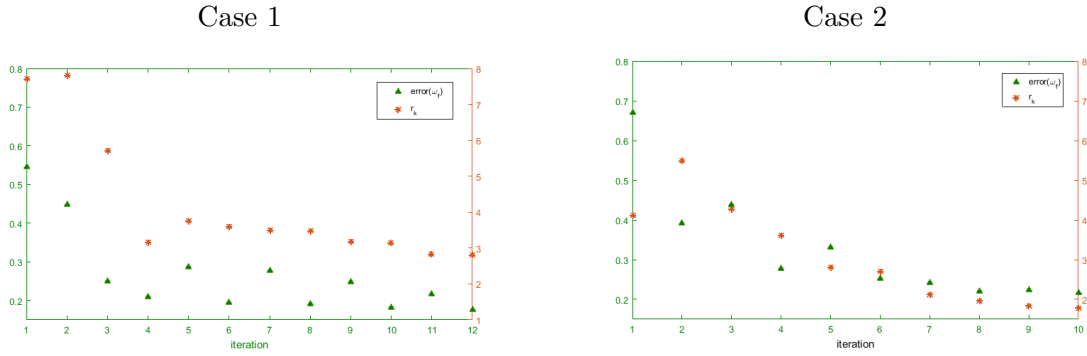


Figure 5.26: The error and residual decrease during the ADMM descents: Green triangles represent the scaled error for the final solute fraction ω_f , orange stars correspond to updated r_k values, where $r_k = \sigma_f(k) - p(\omega_f(k))$. The GW wells in this case were placed along $x = 16 \text{ m}$ and $x = 24 \text{ m}$

The profiles of initial and final solute mass fraction estimates versus the true models are plotted for Case1 and Case 2 in Figure 5.27, Figure 5.28 respectively.

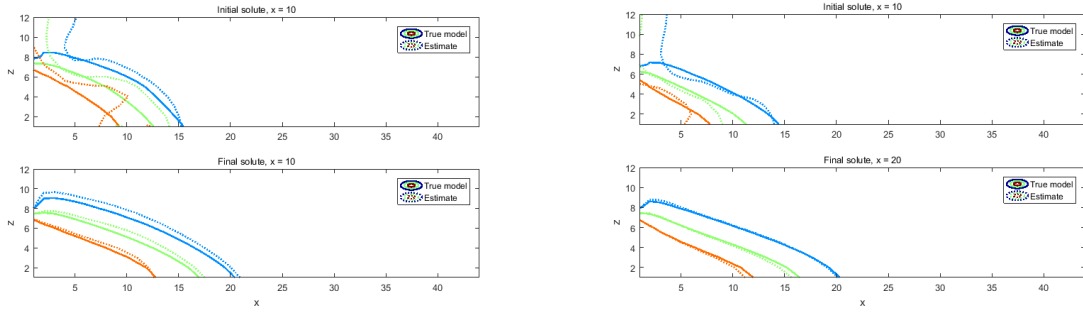


Figure 5.27: ADMM estimates for Case 1: Contour profiles at $x = 10$ and $x = 20$. The dashed lines are estimates from the joint inversion (ADMM), and the full contour lines are the actual locations corresponding to $\omega = 0.25$ (blue), $\omega = 0.5$ (green) and $\omega = 0.75$ (red).

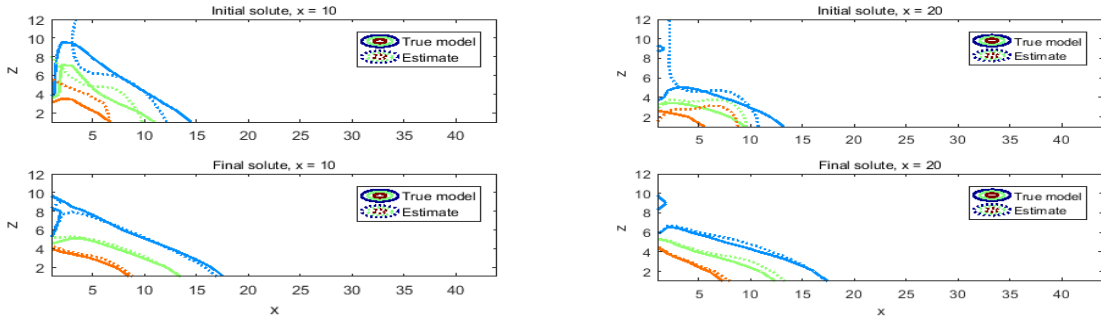


Figure 5.28: ADMM estimates for Case 2: Contour profiles at $x = 10$ and $x = 20$. The dashed lines are estimates from the joint inversion (ADMM), and the full contour lines are the actual locations corresponding to $\omega = 0.25$ (blue), $\omega = 0.5$ (green) and $\omega = 0.75$ (red).

Different GW experimental designs

Afterward, we run the joint inversion for different locations of GW data. We used the same combinations of transects as before, plotted in Figure 5.10, and recorded the scaled error decrease for the initial and final solute fraction estimates for each design (in Figure 5.30). Compared to coupling with DC resistivity data, in the heterogeneous Case 2 we obtained on average lower errors for the final solute estimates, in the homogeneous Case 1 though, the error of initial solute estimates were higher. In both cases the error decrease for the final estimate was fairly similar regardless the GW design.

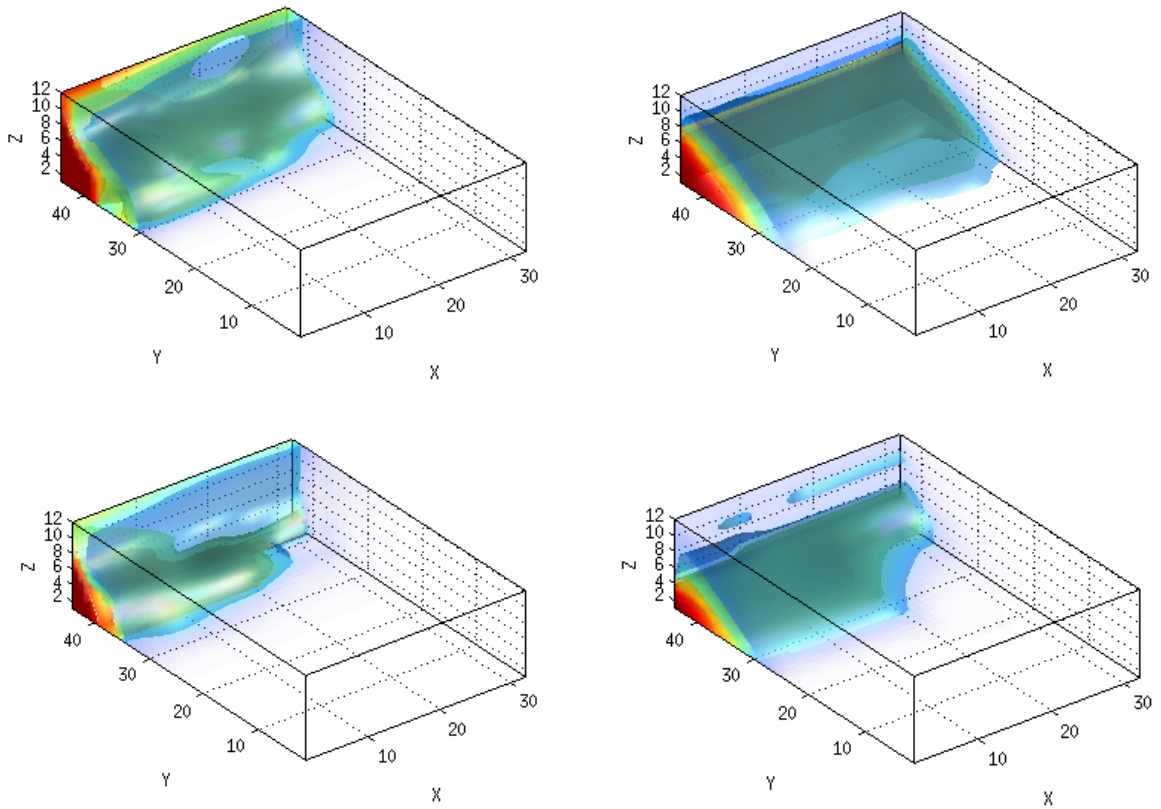


Figure 5.29: ADMM estimates. Upper left and right: Estimates for initial and final solute distribution for Case 1. Bottom left and right: Estimates for initial and final solute distribution for Case 2. Isosurfaces at $\omega = 0.25, 0.5$ and 0.75 are displayed. The true models are plotted in Figure 5.3

5.3.2 Summary

ADMM method applied to joint inversion with EM data lead to similar conclusions as when applied to seawater intrusion example in section 5.1 with DC resistivity data. The joint inversion with ADMM decreased the estimate errors in all cases compared to a simpler coupled approach only or a separate inversion. In the heterogeneous case, the ADMM approach managed to improve the estimates consistently even for different designs of groundwater data locations.

The main difference compared to coupling with DC resistivity data is thus increasing

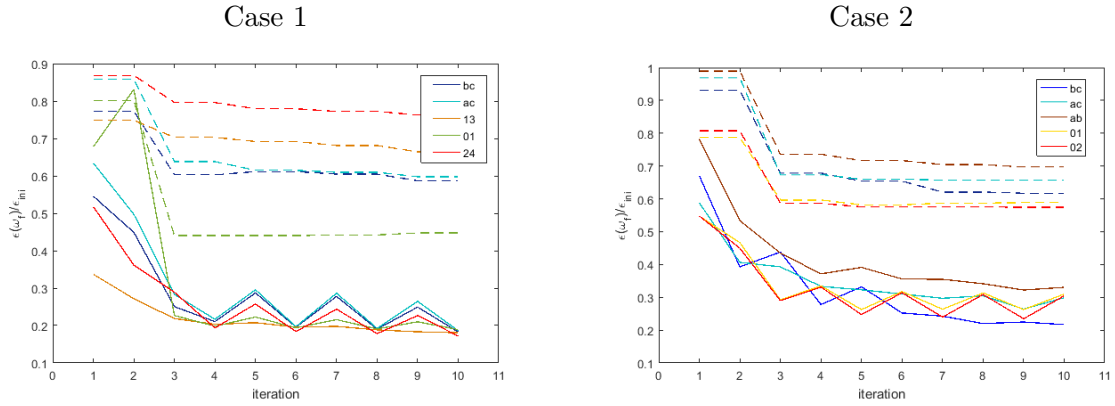


Figure 5.30: The relative error decrease for different GW sampling designs; the dotted line is for the ω_0 relative error, the full line for the ω_f relative error decrease. The plotted results are based on different transects of wells plotted in Figure 5.10.

the computational time due to the TDEM forward and inverse model. On the other hand, during our tests and implementation of the ADMM for EM data we could observe that the joint inversion is converging to a minimum, though possibly in more iterations, regardless the initial guess or particular weights setup. Coupling with TDEM data therefore seemed to be more robust, compared to coupling with DC resistivity data.

Chapter 6

Conclusions

Joint hydrogeophysical inversion is an attractive option to improve parameter and state estimates for groundwater models and to better monitor and predict solute transport processes. However, when evaluating the hydrological and geophysical data, simpler coupled approaches which use existing codes for groundwater or geophysical models are often preferred. In this thesis we developed both models in the same computational environment and derived the sensitivities analytically to reduce the computational burden of solving the inverse problem. With such a setup we were able to test different joint inversion schemes for problems in 3D, which was one of the goals of this thesis.

In chapter two, we introduced the groundwater models developed for this study. The first one enables solute transport calculations, such as salt tracer tests, and the second one is used to model more complex processes such as seawater intrusions by enabling variable density flow. For geophysical modeling we implemented DC resistivity and time domain electromagnetic surveys, which are both sensitive to changes in subsurface electrical conductivity (and thus also fluid conductivity). DC resistivity is a popular technique among hydrogeologists, since, compared to some other geophysical methods, it represents a relatively cheap method with easy data collection.

In most coupled approaches, the groundwater and geophysical properties are linked via an empirical petrophysical relationship, whose parameters need to be determined. For laboratory experiments, e.g. sand box with homogeneous soil, the parameter values can be easily calibrated, but in the field conditions the parameters are uncertain at best. Therefore, when coupling the groundwater and geophysical data, we need to consider two different situations: first, when the petrophysical relationship is known and second, when its param-

eters are unknown and we only assume some structure similarity between solute content and electrical conductivity. In both cases though, we minimize an objective function which contains the two data misfit terms, regularization terms and the coupling term coming from the petrophysical relationship or a structural constraint. The minimization can be computationally challenging due to the different speeds of convergence for the groundwater and geophysical models. In this work we propose computationally efficient strategies to minimize this objective function, which we tested for multiple synthetic examples, and compared with more standard approaches.

For the joint inversion with a known petrophysical constraint, we proposed here an alternating direction method of multipliers (ADMM), which splits the minimization into two subproblems; the GW and geophysical part. This is advantageous as the two different data misfits do not need to be weighted in one objective function, and we can still proceed with the joint minimization. We tested the ADMM approach on a seawater intrusion example, where we estimated the initial and final saltwater distribution, while assuming the knowledge of other groundwater model parameters. In addition to ADMM, we examined a simpler coupled approach, where the result of a groundwater data inversion served as the reference model for the geophysical inverse problem. ADMM reduced the estimate errors by roughly a half for the final solute estimates and to about 60% for the initial solute compared to a simpler coupled approach errors. Similar quantitative results were obtained when coupling the GW model with both DC resistivity and TDEM data. Moreover, altering the GW parameters used in the inversion from the true ones, still lead to significant improvement of ADMM estimates.

For the joint inversion without a known petrophysical constraint, we implemented the cross gradient field product and joint total variation as structure similarity measures and tested the joint inversion on synthetic examples with solute tracer. To minimize the objective function we applied two methods; the block coordinate descent method (BCDM), which also splits the minimization onto groundwater and geophysical part, and the joint Gauss-Newton (JGN) method that minimizes both models simultaneously. Both methods were compared to a single data inversion for groundwater data.

BCDM in all cases improved or at least provided equal estimates. In the case of joint Gauss-Newton minimization we need to set three different weights in the objective function, which is rather difficult, hence, the success in this task varies and so do the errors of estimates. Overall, the joint Gauss-Newton method was a less robust and reliable min-

imization technique. In terms of structure similarity measures, the coupled inversion with a cross gradient field product decreased the errors of state estimates compared to a single data inversion. However, using Joint total variation as a structure similarity measure did not improve the error of estimates regardless the chosen minimization method. The poor performance of Joint total variation can probably be attributed to the scarce groundwater sampling data we had in our study.

The structure coupled inversion was also applied to solve the inverse problem for parameter estimation, specifically to estimate the hydraulic conductivity K . We adopted the reduced parametrization via the Karhunen-Loeve expansion for the covariance matrix of the conductivity field, which was assumed to be lognormal. To our knowledge, no structural inversion has been done using a parametric approach. The improvement in terms of error was relatively small compared to the groundwater data inversion alone; however, the joint inversion led to lower heterogeneity contrast estimates of the conductivity K , which were closer to the true field.

In summary, based on all the synthetic studies conducted, we can confirm that the joint inversion approach leads to better estimates of states or parameters for GW models. The goodness of estimates was largely determined by the quality and amount of data available, which plays a key role in the success of solving any inverse problem. Different data sampling locations result in differing final estimate errors. Increasing the amount of groundwater data led to small improvements of the joint approach estimates compared to the coupled approach or single data inversion alone. Results also show that, if the amount of groundwater data samples was reduced, the joint approaches were still able to give reasonable estimates with lower errors, indicating that the joint approach is less sensitive to the amount of GW data samples.

However, the fact that the joint inversion improves the estimates of GW parameters and states is not surprising or new, many coupled approaches have been documented to improve the estimates by previous research studies. The main contribution of this work therefore lies in introducing the minimization techniques that can handle the joint inversion for 3D inverse problems.

To our knowledge, neither ADMM or BCDM have been applied to solve hydrogeophysical inversion problems before. In this work we implemented both methods, including the implicit computation of sensitivities and complex time stepping techniques, and showed that we can solve the inverse problems in 3D in a relatively short time. Moreover, the proposed

methods can also be applied to large scale problems, since they enable parallelization.

Structure coupled inversion in hydrogeophysics is still unexplored area, therefore, we picked a rather simple scenario to test the feasibility of such an approach. The results are promising, with some improvement even for the estimation of heterogeneous hydraulic conductivity. For future research in this area, it would be worthwhile to test the structure coupled inversion on more complex examples and with different types of geophysical data. However, without the knowledge of the petrophysical relationship, we have less information about the system and can not expect as much improvement as in the situation where a valid petrophysical relationship is implemented.

Bibliography

- [1] E. Abarca, J. Carrera, X. Sánchez-Vila, and M. Dentz. Anisotropic dispersive henry problem. *Advances in Water Resources*, 30(4):913–926, 2007. → pages x, 26
- [2] P. Ackerer, A. Younès, and M. Mancip. A new coupling algorithm for density-driven flow in porous media. *Geophysical research letters*, 31(12), 2004. → pages 23
- [3] G. E. Archie et al. The electrical resistivity log as an aid in determining some reservoir characteristics. *Transactions of the AIME*, 146(01):54–62, 1942. → pages 42
- [4] P. M. Barlow and E. G. Reichard. Saltwater intrusion in coastal regions of north america. *Hydrogeology Journal*, 18(1):247–260, 2010. → pages 57
- [5] P. Bauer-Gottwein, B. N. Gondwe, L. Christiansen, D. Herckenrath, L. Kgotlhang, and S. Zimmermann. Hydrogeophysical exploration of three-dimensional salinity anomalies with the time-domain electromagnetic method (tdem). *Journal of Hydrology*, 380(3):318–329, 2010. → pages 6
- [6] J. Bear and A. H.-D. Cheng. *Modeling groundwater flow and contaminant transport*, volume 23. Springer Science & Business Media, 2010. → pages 16, 21
- [7] J. Bear, A. H.-D. Cheng, S. Sorek, D. Ouazar, and I. Herrera. *Seawater intrusion in coastal aquifers: concepts, methods and practices*, volume 14. Springer Science & Business Media, 1999. → pages 15
- [8] J. Beaujean, F. Nguyen, A. Kemna, A. Antonsson, and P. Engesgaard. Calibration of seawater intrusion models: Inverse parameter estimation using surface electrical resistivity tomography and borehole data. *Water Resources Research*, 50(8): 6828–6849, 2014. → pages 6, 8, 58
- [9] A. Beck and L. Tetrushvili. On the convergence of block coordinate descent type methods. *SIAM Journal on Optimization*, 23(4):2037–2060, 2013. → pages 54
- [10] P. Blomgren and T. F. Chan. Color tv: total variation methods for restoration of vector-valued images. *IEEE transactions on image processing*, 7(3):304–309, 1998. → pages 45

- [11] S. Boyd, N. Parikh, E. Chu, B. Peleato, and J. Eckstein. Distributed optimization and statistical learning via the alternating direction method of multipliers. *Foundations and Trends® in Machine Learning*, 3(1):1–122, 2011. → pages 12, 52
- [12] M. B. Cardenas and M. R. Kanarek. Soil moisture variation and dynamics across a wildfire burn boundary in a loblolly pine (*pinus taeda*) forest. *Journal of Hydrology*, 519:490–502, 2014. → pages 3
- [13] M. Cardiff and P. Kitanidis. Bayesian inversion for facies detection: An extensible level set framework. *Water Resources Research*, 45(10), 2009. → pages 10, 44, 73
- [14] A. Cardona, J. Carrillo-Rivera, R. Huizar-Alvarez, and E. Graniel-Castro. Salinization in coastal aquifers of arid zones: an example from santo domingo, baja california sur, mexico. *Environmental Geology*, 45(3):350–366, 2004. → pages 4
- [15] J. Carrera, J. J. Hidalgo, L. J. Slooten, and E. Vázquez-Suñé. Computational and conceptual issues in the calibration of seawater intrusion models. *Hydrogeology journal*, 18(1):131–145, 2010. → pages 2
- [16] M. A. Celia, T. F. Russell, I. Herrera, and R. E. Ewing. An eulerian-lagrangian localized adjoint method for the advection-diffusion equation. *Advances in Water Resources*, 13(4):187–206, 1990. → pages 19
- [17] M. Commer and G. A. Newman. Three-dimensional controlled-source electromagnetic and magnetotelluric joint inversion. *Geophysical Journal International*, 178(3):1305–1316, 2009. → pages 50
- [18] M. Commer, M. B. Kowalsky, J. Doetsch, G. A. Newman, and S. Finsterle. Mpitough2: A parallel parameter estimation framework for hydrological and hydrogeophysical applications. *Computers & Geosciences*, 65:127–135, 2014. → pages 9
- [19] J.-C. Comte and O. Banton. Cross-validation of geo-electrical and hydrogeological models to evaluate seawater intrusion in coastal aquifers. *Geophysical research letters*, 34(10), 2007. → pages 57
- [20] J.-C. Comte, O. Banton, J.-L. Join, and G. Cabioch. Evaluation of effective groundwater recharge of freshwater lens in small islands by the combined modeling of geoelectrical data and water heads. *Water Resources Research*, 46(6), 2010. → pages 3
- [21] S. Costabel and U. Yaramanci. Estimation of water retention parameters from nuclear magnetic resonance relaxation time distributions. *Water resources research*, 49(4):2068–2079, 2013. → pages 4

- [22] D. L. de Castro and R. M. G. C. Branco. 4-d ground penetrating radar monitoring of a hydrocarbon leakage site in fortaleza (brazil) during its remediation process: a case history. *Journal of Applied Geophysics*, 54(1):127–144, 2003. → pages 4
- [23] W. Deng and W. Yin. On the global and linear convergence of the generalized alternating direction method of multipliers. *Journal of Scientific Computing*, 66(3): 889–916, 2016. → pages 52
- [24] J. Doetsch, N. Linde, M. Pessognelli, A. G. Green, and T. Günther. Constraining 3-d electrical resistance tomography with gpr reflection data for improved aquifer characterization. *Journal of Applied Geophysics*, 78:68–76, 2012. → pages 4
- [25] J. E. Doherty, R. J. Hunt, and M. J. Tonkin. *Approaches to highly parameterized inversion: A guide to using PEST for model-parameter and predictive-uncertainty analysis*. US Department of the Interior, US Geological Survey, 2011. → pages 7
- [26] J. Douglas, Jr and T. F. Russell. Numerical methods for convection-dominated diffusion problems based on combining the method of characteristics with finite element or finite difference procedures. *SIAM Journal on Numerical Analysis*, 19(5): 871–885, 1982. → pages 19
- [27] M. Droske and M. Rumpf. A variational approach to nonrigid morphological image registration. *SIAM Journal on Applied Mathematics*, 64(2):668–687, 2004. → pages 44
- [28] M. J. Ehrhardt, K. Thielemans, L. Pizarro, D. Atkinson, S. Ourselin, B. F. Hutton, and S. R. Arridge. Joint reconstruction of pet-mri by exploiting structural similarity. *Inverse Problems*, 31(1):015001, 2014. → pages 45
- [29] G. O. Essink. Modeling three-dimensional density dependent groundwater flow at the island of texel, the netherlands. *Coastal Aquifer Management-Monitoring, Modeling, and Case Studies*, page 77, 2016. → pages 57
- [30] C. G. Farquharson and D. W. Oldenburg. A comparison of automatic techniques for estimating the regularization parameter in non-linear inverse problems. *Geophysical Journal International*, 156(3):411–425, 2004. → pages 48
- [31] D. V. Fitterman. Mapping saltwater intrusion in the biscayne aquifer, miami-dade county, florida using transient electromagnetic sounding. *Journal of Environmental and Engineering Geophysics*, 19(1):33–43, 2014. → pages 57
- [32] D. E. Fowler and S. M. Moysey. Estimation of aquifer transport parameters from resistivity monitoring data within a coupled inversion framework. *Journal of Hydrology*, 409(1):545–554, 2011. → pages 3

- [33] L. A. Gallardo and M. A. Meju. Characterization of heterogeneous near-surface materials by joint 2d inversion of dc resistivity and seismic data. *Geophysical Research Letters*, 30(13), 2003. → pages 45
- [34] L. A. Gallardo and M. A. Meju. Joint two-dimensional dc resistivity and seismic travel time inversion with cross-gradients constraints. *Journal of Geophysical Research: Solid Earth*, 109(B3), 2004. → pages 10
- [35] L. A. Gallardo and M. A. Meju. Structure-coupled multiphysics imaging in geophysical sciences. *Reviews of Geophysics*, 49(1), 2011. → pages 10, 44
- [36] E. Ghadimi, A. Teixeira, I. Shames, and M. Johansson. Optimal parameter selection for the alternating direction method of multipliers (admm): quadratic problems. *IEEE Transactions on Automatic Control*, 60(3):644–658, 2015. → pages 12, 52
- [37] E. Haber. *Computational methods in geophysical electromagnetics*, volume 1. SIAM, 2014. → pages 18, 30, 33, 48
- [38] E. Haber and M. H. Gazit. Model fusion and joint inversion. *Surveys in Geophysics*, 34(5):675–695, 2013. → pages 44, 45
- [39] E. Haber and D. Oldenburg. Joint inversion: a structural approach. *Inverse problems*, 13(1):63, 1997. → pages 10, 44, 45
- [40] F. Haeni. *Application of seismic-refraction techniques to hydrologic studies*. US Government Printing Office, 1988. → pages 4
- [41] P. C. Hansen. *Discrete inverse problems: insight and algorithms*, volume 7. Siam, 2010. → pages 62
- [42] J. D. Hem. *Study and interpretation of the chemical characteristics of natural water*, volume 2254. Department of the Interior, US Geological Survey, 1985. → pages 43
- [43] H. R. Henry. Interfaces between salt water and fresh water in coastal aquifers. *US Geological Survey Water-Supply Paper*, pages C35–70, 1964. → pages 24
- [44] D. Herckenrath, G. Fiandaca, E. Auken, and P. Bauer-Gottwein. Sequential and joint hydrogeophysical inversion using a field-scale groundwater model with ert and tdem data. *Hydrology and Earth System Sciences*, 17(10):4043–4060, 2013. → pages 3, 6, 7
- [45] D. Herckenrath, N. Odlum, V. Nenna, R. Knight, E. Auken, and P. Bauer-Gottwein. Calibrating a salt water intrusion model with time-domain electromagnetic data. *Groundwater*, 51(3):385–397, 2013. → pages 3, 6, 9, 58

- [46] T. Hermans, A. Vandenbohede, L. Lebbe, R. Martin, A. Kemna, J. Beaujean, and F. Nguyen. Imaging artificial salt water infiltration using electrical resistivity tomography constrained by geostatistical data. *Journal of Hydrology*, 438:168–180, 2012. → pages 7
- [47] A. Hinnell, T. Ferré, J. Vrugt, J. Huisman, S. Moysey, J. Rings, and M. Kowalsky. Improved extraction of hydrologic information from geophysical data through coupled hydrogeophysical inversion. *Water resources research*, 46(4), 2010. → pages 3, 6, 7
- [48] W. Hu, A. Abubakar, and T. M. Habashy. Joint electromagnetic and seismic inversion using structural constraints. *Geophysics*, 74(6):R99–R109, 2009. → pages 10
- [49] J. Irving and K. Singha. Stochastic inversion of tracer test and electrical geophysical data to estimate hydraulic conductivities. *Water Resources Research*, 46(11), 2010. → pages 3, 6, 8
- [50] A. Jardani, A. Revil, A. Bolève, A. Crespy, J.-P. Dupont, W. Barrash, and B. Malama. Tomography of the darcy velocity from self-potential measurements. *Geophysical Research Letters*, 34(24), 2007. → pages 42
- [51] A. Jardani, A. Revil, and J. Dupont. Stochastic joint inversion of hydrogeophysical data for salt tracer test monitoring and hydraulic conductivity imaging. *Advances in Water Resources*, 52:62–77, 2013. → pages 3, 7, 8, 80
- [52] D. H. Jayawickreme, C. S. Santoni, J. H. Kim, E. G. Jobbágy, and R. B. Jackson. Changes in hydrology and salinity accompanying a century of agricultural conversion in argentina. *Ecological Applications*, 21(7):2367–2379, 2011. → pages 3
- [53] D. H. Jayawickreme, E. G. Jobbágy, and R. B. Jackson. Geophysical subsurface imaging for ecological applications. *New Phytologist*, 201(4):1170–1175, 2014. → pages 3
- [54] T. C. Johnson, R. J. Versteeg, H. Huang, and P. S. Routh. Data-domain correlation approach for joint hydrogeologic inversion of time-lapse hydrogeologic and geophysical data. *Geophysics*, 74(6):F127–F140, 2009. → pages 10, 44, 73
- [55] A. Kacimov, M. Sherif, J. Perret, and A. Al-Mushikhi. Control of sea-water intrusion by salt-water pumping: Coast of oman. *Hydrogeology Journal*, 17(3):541–558, 2009. → pages 57
- [56] A. Kemna, A. Binley, F. Day-Lewis, A. Englert, B. Tezkan, J. Vanderborght, H. Vereecken, and P. Winship. Solute transport processes. In *Applied Hydrogeophysics*, pages 117–159. Springer, 2006. → pages 42, 43

- [57] O. Kolditz, R. Ratke, H.-J. G. Diersch, and W. Zielke. Coupled groundwater flow and transport: 1. verification of variable density flow and transport models. *Advances in Water Resources*, 21(1):27–46, 1998. → pages 15, 22
- [58] L. F. Konikow, D. J. Goode, and G. Z. Hornberger. *A three-dimensional method-of-characteristics solute-transport model (MOC3D)*. US Geological Survey, 1996. → pages 19
- [59] M. B. Kowalsky, S. Finsterle, J. Peterson, S. Hubbard, Y. Rubin, E. Majer, A. Ward, and G. Gee. Estimation of field-scale soil hydraulic and dielectric parameters through joint inversion of gpr and hydrological data. *Water Resources Research*, 41(11), 2005. → pages 41
- [60] C. D. Langevin and W. Guo. Modflow/mt3dms-based simulation of variable-density ground water flow and transport. *Ground Water*, 44(3):339–351, 2006. → pages 19
- [61] C. D. Langevin and M. Zygnerski. Effect of sea-level rise on salt water intrusion near a coastal well field in southeastern florida. *Groundwater*, 51(5):781–803, 2013. → pages 57
- [62] C. D. Langevin, D. T. Thorne Jr, A. M. Dausman, M. C. Sukop, and W. Guo. Seawat version 4: A computer program for simulation of multi-species solute and heat transport. Technical report, Geological Survey (US), 2008. → pages 19
- [63] P. G. Lelièvre and D. W. Oldenburg. A comprehensive study of including structural orientation information in geophysical inversions. *Geophysical Journal International*, 178(2):623–637, 2009. → pages 10
- [64] P. G. Lelièvre, D. W. Oldenburg, and N. C. Williams. Integrating geological and geophysical data through advanced constrained inversions*. *Exploration Geophysics*, 40(4):334–341, 2009. → pages 10
- [65] T. Lochbühler, J. Doetsch, R. Brauchler, and N. Linde. Structure-coupled joint inversion of geophysical and hydrological data. *Geophysics*, 78(3):ID1–ID14, 2013. → pages 11, 45, 73
- [66] J. Mead. Parameter estimation: A new approach to weighting a priori information. *J. Inv. Ill-posed Problems*, 16(2):175–194, 2008. → pages 33
- [67] A. Medina and J. Carrera. Coupled estimation of flow and solute transport parameters. *Water Resources Research*, 32(10):3063–3076, 1996. → pages 48
- [68] T. Mills, P. Hoekstra, M. Blohm, and L. Evans. Time domain electromagnetic soundings for mapping sea-water intrusion in monterey county, california. *Ground Water*, 26(6):771–782, 1988. → pages 57

- [69] D. M. Molodtsov, V. N. Troyan, Y. V. Roslov, and A. Zerilli. Joint inversion of seismic traveltimes and magnetotelluric data with a directed structural constraint. *Geophysical Prospecting*, 61(6):1218–1228, 2013. → pages 10
- [70] M. Moorkamp. *Integrated Imaging of the Earth: Theory and Applications*, volume 218. John Wiley & Sons, 2016. → pages 44
- [71] L. Neilson-Welch and L. Smith. Saline water intrusion adjacent to the fraser river, richmond, british columbia. *Canadian geotechnical journal*, 38(1):67–82, 2001. → pages xi, 59, 60
- [72] V. Nenna, D. Herckenrath, R. Knight, N. Odlum, and D. McPhee. Application and evaluation of electromagnetic methods for imaging saltwater intrusion in coastal aquifers: Seaside groundwater basin, california. *Geophysics*, 78(2):B77–B88, 2013. → pages 4, 57
- [73] W. Nijland, M. Van der Meijde, E. A. Addink, and S. M. De Jong. Detection of soil moisture and vegetation water abstraction in a mediterranean natural area using electrical resistivity tomography. *Catena*, 81(3):209–216, 2010. → pages x, 3, 4
- [74] R. Nishihara, L. Lessard, B. Recht, A. Packard, and M. I. Jordan. A general analysis of the convergence of admm. *arXiv preprint*, 2015. → pages 53
- [75] J. Nocedal and S. Wright. *Numerical optimization*. Springer Science & Business Media, 2006. → pages 36, 51, 54
- [76] D. S. Oliver and Y. Chen. Recent progress on reservoir history matching: a review. *Computational Geosciences*, 15(1):185–221, 2011. → pages 80
- [77] J. G. Paine. Determining salinization extent, identifying salinity sources, and estimating chloride mass using surface, borehole, and airborne electromagnetic induction methods. *Water Resources Research*, 39(3), 2003. → pages 4
- [78] E. E. Poeter, M. C. Hill, E. R. Banta, S. Mehl, and S. Christensen. Ucode_2005 and six other computer codes for universal sensitivity analysis, calibration, and uncertainty evaluation constructed using the jupiter api. Technical report, 2006. → pages 7
- [79] D. Pollock and O. A. Cirpka. Fully coupled hydrogeophysical inversion of synthetic salt tracer experiments. *Water Resources Research*, 46(7), 2010. → pages 8, 80
- [80] D. Pollock and O. A. Cirpka. Fully coupled hydrogeophysical inversion of a laboratory salt tracer experiment monitored by electrical resistivity tomography. *Water Resources Research*, 48(1), 2012. → pages 7, 8

- [81] M. Putti and C. Paniconi. Picard and newton linearization for the coupled model for saltwater intrusion in aquifers. *Advances in water resources*, 18(3):159–170, 1995. → pages 24
- [82] B. S. RamaRao, A. M. LaVenue, G. De Marsily, and M. G. Marietta. Pilot point methodology for automated calibration of an ensemble of conditionally simulated transmissivity fields: 1. theory and computational experiments. *Water Resources Research*, 31(3):475–493, 1995. → pages 80
- [83] M. Razaviyayn, M. Hong, and Z.-Q. Luo. A unified convergence analysis of block successive minimization methods for nonsmooth optimization. *SIAM Journal on Optimization*, 23(2):1126–1153, 2013. → pages 54
- [84] Y. Rubin and S. S. Hubbard. *Hydrogeophysics*, volume 50. Springer Science & Business Media, 2006. → pages 3
- [85] T. F. Russell and M. A. Celia. An overview of research on eulerian–lagrangian localized adjoint methods (ellam). *Advances in Water Resources*, 25(8):1215–1231, 2002. → pages 19
- [86] E. Sanchez-León, C. Leven, C. Haslauer, and O. Cirpka. Combining 3d hydraulic tomography with tracer tests for improved transport characterization. *Groundwater*, 2015. → pages 80
- [87] W. E. Sanford and J. P. Pope. Current challenges using models to forecast seawater intrusion: lessons from the eastern shore of virginia, usa. *Hydrogeology Journal*, 18(1):73–93, 2010. → pages 57
- [88] G. Sapiro and D. L. Ringach. Anisotropic diffusion of multivalued images with applications to color filtering. *IEEE transactions on image processing*, 5(11):1582–1586, 1996. → pages 45
- [89] S. Sorek and V. Borisov. Modified eulerian–lagrangian formulation for hydrodynamic modeling. *Journal of Computational Physics*, 231(8):3083–3100, 2012. → pages 19
- [90] K. Steklova and E. Haber. 3d joint hydrogeophysical inversion using similarity measures. *submitted to Applied Mathematics and Computations*. → pages iv
- [91] K. Steklova and E. Haber. Joint hydrogeophysical inversion: state estimation for seawater intrusion models in 3d. *Computational Geosciences*, pages 1–20, 2016. → pages iv, 13
- [92] D. K. Todd and L. W. Mays. Groundwater hydrology edition, 1980. → pages 16

- [93] F. Trabelsi, A. B. Mammou, J. Tarhouni, C. Piga, and G. Ranieri. Delineation of saltwater intrusion zones using the time domain electromagnetic method: the nabeul–hammamet coastal aquifer case study (ne tunisia). *Hydrological Processes*, 27(14):2004–2020, 2013. → pages 4, 57
- [94] C. R. Vogel. *Computational methods for inverse problems*, volume 23. Siam, 2002. → pages 62
- [95] C. I. Voss, C. T. Simmons, and N. I. Robinson. Three-dimensional benchmark for variable-density flow and transport simulation: matching semi-analytic stability modes for steady unstable convection in an inclined porous box. *Hydrogeology journal*, 18(1):5–23, 2010. → pages 21
- [96] J.-M. Vouillamoz, S. Sokheng, O. Bruyere, D. Caron, and L. Arnout. Towards a better estimate of storage properties of aquifer with magnetic resonance sounding. *Journal of Hydrology*, 458:51–58, 2012. → pages 4
- [97] K. Vozoff and D. Jupp. Joint inversion of geophysical data. *Geophysical Journal International*, 42(3):977–991, 1975. → pages 41
- [98] A. S. Ward, M. N. Gooseff, M. Fitzgerald, T. J. Voltz, and K. Singha. Spatially distributed characterization of hyporheic solute transport during baseflow recession in a headwater mountain stream using electrical geophysical imaging. *Journal of Hydrology*, 517:362–377, 2014. → pages 3
- [99] B. Wohlberg, D. M. Tartakovsky, and M. Dentz. Linearized functional minimization for inverse modeling. In *XIX International Conference on Water Resources (CMWR), Urbana-Champaign, IL, USA*, 2012. → pages 12